THE UNIVERSITY *of* EDINBURGH

ERICH ESSMANN

COMPLEX DYNAMICS OF SOLID-FLUID SYSTEMS

COMPLEX DYNAMICS OF SOLID-FLUID SYSTEMS

ERICH ESSMANN

THE UNIVERSITY
of EDINBURGH

Applications of Dynamic Systems Theory to Fluid Dynamics

Doctorate of Philosophy
University of Edinburgh

October 2019

Erich Essmann: *Complex Dynamics of Solid-Fluid Systems,* Applications of Dynamic Systems Theory to Fluid Dynamics, Doctorate of Philosophy

SUPERVISORS:
Dr. Prashant Valluri, (University of Edinburgh, Edinburgh)
Prof. Rama Govindarajan, (ICTS-TIFR, Bengaluru)
Dr. Timm Krüger, (University of Edinburgh, Edinburgh)
LOCATION:

Edinburgh

TIME FRAME:

October 2019

I dedicate this to Anna and Johann;
vir al die grenslose liefde.

DECLARATION

I declare that this thesis was composed by myself, that the work contained herein is my own except where explicitly stated otherwise in the text and that this work has not been submitted for any other degree or professional qualification.

Edinburgh, October 2019

Erich Essmann

ABSTRACT

The focus of this thesis was the investigation of the complex dynamics of solid-fluid systems. These systems are of great industrial importance, such as in methane clathrate formation in sub-sea pipelines, [23]. As well as being crucial to furthering our understanding of various natural phenomena, such as the rate of rain droplet formation in clouds, [88].

We began by considering the problem of the orbits tracked by ellipsoids immersed in viscous and inviscid environments. This investigation was carried out by a combination of analytical and numerical techniques: direct numerical simulations of resolved full-coupled solid-fluid systems, analysis the Kirchhoff-Clebsch equations for the case of inviscid flows, and characterising dynamics through advanced techniques such as recurrence quantification analysis. We demonstrate that the ellipsoid tracks a chaotic orbit not only in an inviscid environment but also when submerged in a viscous fluid, under specific conditions. Under inviscid environments, an ellipsoid subject to arbitrary initial conditions of linear and angular momentum demonstrates chaotic orbits when all the three axes of the ellipsoid are unequal, in agreement with the Kozlov and Onishchenko [57]'s theorem of non-integrability of Kirchhoff's equations and also with Aref and Jones [3]'s potential flow solution.

We then extended our methodology to understand the dynamics of a single ellipsoid tumbling in a viscous environment with the presence of both passive and viscosity coupled tracers in addition to the chaotic dynamics predicted by the Kirchhoff-Clebsch equations. Our results show that the bodies move along from viscosity gradients towards minima of the viscous stress. These bodies might become trapped in unstable minima. However, more work is needed to understand the long-term mixing of viscosity coupled tracers. Our direct numerical solver was also extended to include contact models for solid-solid interactions in the simulation domain. The validation of the contact models was presented.

Finally, we expand, the theoretical framework of the Kirchhoff-Clebsch equations to account for the presence of multiple bodies. This extension was done by using Hamiltonian mechanics to extend the derivation proposed by Lamb [63]. We present our preliminary result of simulating two solids systems using the extended Kirchhoff-Clebsch equations. The relative orientations of the two solids were found to regularly switch from being correlated to anti-correlated in an otherwise chaotic system. Further work is required to understand the mechanism behind this behaviour.

LAY SUMMARY

Solid-fluid systems are part of everyone's daily experiences: leaves blown in the wind, snow settling on a winter's eve, sand being swept down a river, or air laden with droplets and particles such as in clouds.

These are all examples of solid-fluid interactions that all of us have experienced. They arise from a vast array of different mechanisms, such as gravity, temperature or concentration gradients, crystallisation or condensation. While appearing initially disparate, all these systems have certain features in common. Namely, they have a fluid continuum, suspended solids transported by the fluid, and a two-way coupled interaction between the fluid and suspended solids. The most important of these commonalities is the two-way coupling between the fluid and solids, and it allows for the combined system's dynamics to be far more vibrant. This thesis investigates the behaviour of these systems by constructing mathematical models which simulate the important commonalities they share.

Starting from the simplest possible solid-fluid system, namely a single solid immersed in a fluid, dynamics of a single solid in the fluid was simulated using the mathematical models, and its motion was found to be dependent on the geometry. If the solid were asymmetric its movement through the fluid would be chaotic. This chaotic motion might be necessary for explaining how raindrops grow in clouds; however, more work is needed to confirm this hypothesis. Next, how the motion of these solids affects mixing in the fluid is investigated. Results suggest that solids which had chaotic motion mixed their surrounding fluid more efficiently than those solids which were not chaotic. Lastly, models were extended to account for multiple solids, contacts and collisions. This was an important extension since in most solid-fluid system, there are multiple solids, and they interact with each other constantly. Therefore it was essential to develop new modelling methods that can handle these interactions. This new framework allows me simulation of more complicated systems, which are closer to reality.

The heavens declare the glory of God;
the skies proclaim the work of his hands.
Day after day they pour forth speech;
night after night they reveal knowledge.

— Psalm 19:1-4

ACKNOWLEDGEMENTS

I gratefully acknowledge the generous financial support of the Namibia Students Financial Assistance Fund and from the ThermaSMART project for allowing me to be sent on secondment to ICTS in Bangaluru. I want to express my sincerest thanks to Mr Rudolf Fourie. His support allowed me to come to Edinburgh and made all of this possible.

I want to express my sincere gratitude to my supervisor Dr Prashant Valluri for the continuous support and supervision of my work. I am grateful for his patience, motivation, and immense knowledge. His guidance helped me in all the time of research and writing of this thesis. In discussions with him, I was enlightened about the importance of fundamental research and its contributions to society. I could not have imagined having a better supervisor and mentor for my PhD.

My sincere thanks go to my second supervisor, Prof. Rama Govindarajan (ICTS-TIFR, Bengaluru). I want to thank her for her brilliant insight and support. I am eternally grateful for providing me with the opportunity to go on secondment to ICTS-TIFR, Bengaluru.

My thanks also go to Dr Timm Krueger, who has been a wellspring of wisdom and support.

I thank my fellow students in the office for the stimulating discussions, for the sleepless nights we were working together before deadlines, and for all the fun we have had in the last four years.

Last but not least, I would like to thank my family: my parents, Anna and Johann for their unwavering love, and to my brother, Anrich, for supporting me throughout writing this thesis and my life in general.

CONTENTS

LIST OF FIGURES

LIST OF TABLES

NOMENCLATURE

Latin Letters

(a, b, c)	Dimensions of a general ellipsiod	m	L
a_f	Volume fraction of the fluid	–	
$\mathcal{A}$	Added mass tensor for the fluid	–	
a_s	Volume fraction of the solid	–	
D	Diffusion coefficient of the tracer	m^2/s	L^2T^-1
E	Energy ratio between the linear kinetic and angular kinetic energy of a body	–	
(λ, μ, ν)	Components of the Ellipsoidal coordinate system	–	
$\mathcal{F}$	Momentum flux tensor	$kg/m/s^2$	$ML^{-1}T^{-2}$
$\boldsymbol{f}$	Generalised contact fo vector	–	
f	Particle distribution function	–	
$\boldsymbol{f}_{ext}$	Generalised external force vector	–	

$\boldsymbol{f_S}$	Hydrodynamic force experieced by the immersed body	$\mathrm{N/m^3}$	$\mathrm{ML^{-2}T^{-2}}$
$\boldsymbol{F}$	Total hydrodynamic force on the immersed boundary	N	$\mathrm{MLT^{-2}}$
$\boldsymbol{g}$	Gravitational field strength	N/kg	$\mathrm{LT^{-2}}$
$\mathcal{I}_s$	Inertia tensor for the solid	$\mathrm{kgm^2}$	$\mathrm{ML^2}$
$\mathcal{I}_f$	Moment of inertia tensor of the fluid	$\mathrm{kgm^2}$	$\mathrm{ML^2}$
$\underline{\mathbf{1}}$	Identity matrix	–	
$\boldsymbol{j}$	Momentum density vector of the fluid	$\mathrm{kg/m^2/s}$	$\mathrm{ML^{-2}T^{-1}}$
$\mathcal{J}$	Fluid added moment of inertia tensor plus solid moment of inertia	–	
$\mathcal{J}_\rfloor$	Contact condition matrix	–	
K	Kinetic energy	J	$\mathrm{ML^2T^{-2}}$
k	Spring constant for the contact model	N/m	$\mathrm{MT^-2}$
K_{tot}	Total kinetic energy for the solid-fluid system	J	$\mathrm{ML^2T^{-2}}$
L	Size of the computational domain	m	L
$\boldsymbol{L}$	Generalised angular momentum vector	–	
m	Mass of the solid	kg	M
$\mathcal{M}$	Generalised mass tensor	–	
$\boldsymbol{n}$	Normal vector	–	
N	Mesh refinement level	–	L
$\boldsymbol{n}_\Gamma$	Normal vector of the solid domain, Γ	–	
$\mathcal{N}$	Contact normal matrix	–	
p	Pressure of the fluid	Pa	$\mathrm{ML^{-1}T^{-2}}$
$\mathcal{P}$	Projection matrix	–	
$\boldsymbol{P}$	Generalised linear momentum vector	–	
q	Unit quaternion describing orientation of the solid	–	
$\mathcal{Q}$	Quaternion rotation matrix	–	

$\boldsymbol{r}$	Relavtive position vector of a point of the solid interface relative to centre of mass of the solid	m	L
Re_p	Particle Reynolds number	–	
$\boldsymbol{s}$	Body force density vector	N/m^3	$ML^{-2}T^{-1}$
S	Surface area of body	m^2	L^2
s_d	Surface fluid fraction	–	
$\mathcal{S}$	Generalised orientation matrix	–	
Sr	Strouhal number describes oscillating flow mechanics	–	
t	Simulation time	s	T
$\boldsymbol{T}$	Total hydrodynamic torque on by the immersed boundary	Nm	ML^2T^-2
$\boldsymbol{u}$	Velocity vector for the fluid	m/s	LT^{-1}
$\boldsymbol{u}^\star$	Intermediate fluid velocity vector	m/s	LT^{-1}
$\boldsymbol{v}$	Velocity vector of the solid	m/s	LT^{-1}
$\boldsymbol{v}_G$	Generalised velocity vector	–	
V	Volume of the solid	m^3	L^3
$\boldsymbol{x}$	Translational position vector of the centriod of the solid	m	L
$\boldsymbol{X}_k$	Coordinates of the Lagrangian points of the solid boundary	m	L
Δx_{MIN}	Minimum length of fluid mesh cell	m	L
$\boldsymbol{z}$	Contact impulse vector	–	

Greek Letters

α	Tracer advected by the fluid	–	
δ	Interface delta function	–	
$\underline{\boldsymbol{\delta}}_{ij}$	Kronecker delta symbol	–	
Δt	Size of the time step	s	T
ε	Ellipsoid aspect ratio defined as, $\varepsilon = a/b$	–	
γ	Viscous damping constant for the contact model	N/m/s	MT^-3
μ	Viscosity of the fluid	Pas	$ML^{-1}T^{-1}$
ν	Kinematic viscosity of the fluid	m^2/s	L^2T^{-1}
$\Omega(f)$	Collision operator	–	
$\boldsymbol{\Omega}$	Angular velocity of body	rad/s	T^{-1}

ϕ	Velocity potential for an inviscid fluid	–	
ρ_f	Density of the fluid	kg/m³	ML^{-3}
ρ	Density ratio between fluid and solid densities	kg/m³	ML^{-3}
ρ_s	Density of the solid	kg/m³	ML^{-3}
$\underline{\boldsymbol{\sigma}}$	Stress tensor	kg/m/s²	$ML^{-1}T^{-2}$
σ	Thickness of the spring-dashpot potential	m	L
$\boldsymbol{\sigma}$	Generalised position vector	–	
τ	Relaxation time of the system	s	T
$\boldsymbol{\tau}_{ij}$	Unit vector that is perpendicular to $\boldsymbol{n}$ and point in the direction of the tangential motion of the two solids	–	
$\boldsymbol{\theta}$	Vector of Euler angles describing the orienation of the solid	rad	
θ	Euler angle around i axis of the solid	rad	
ξ	Hydrodynamic separation between two bodies	m	L
ξ_β	Microscopic particle velocity	m/s	LT^{-1}
ξ_{min}	Minimum approach distance between two bodies	m	L
Superscripts			
n	Beginning of the time step	–	
$n+1$	End of the time step	–	
$n+\frac{1}{2}$	Intermediate time step	–	
Subscripts			
c	Contant bewteen two bodies	–	
f	Variable related to the Fluid	–	
Γ	Immersed solid region	–	
n	Normal vector to a surface	–	
$\perp$	Perpendicular vector to a surface	–	
s	Variable related to the Solid	–	
t	Tangent vector to a surface	–	

1

INTRODUCTION

Solid-fluid systems are part of everyone's daily experiences: leaves blown in the wind, snow settling on a winters eve, sand being swept down a river, or gas (or air) laden with droplets and particles such as in clouds. These are all examples of solid-fluid interactions that all of us have experienced. They arise from a vast array of different mechanisms, such as gravity, temperature or concentration gradients, crystallisation or condensation. While appearing initially very disparate, all these systems have certain features in common: a fluid continuum, the solids transported by the fluid, and a two-way coupled interaction between fluid and suspended solids. The most important of these commonalities is the two-way coupling between the fluid and the solids, and it allows for the combined system's dynamics to be far more vibrant.

Despite the seeming simplicity of solid-fluid systems, they give rise to a rather complex and fascinating dynamics, due to the interplay of momentum and energy being continuously shared between the fluid and solids. The emergent complexity of these systems has caused them to be an active subject of study since the advent of modern fluid dynamics in the late 19^{th} century. Some of the earliest work on this field was performed by Lamb [63]. The number of experimental and theoretical studies have greatly increased since the early days of the field. This increase has mainly been driven by the abundance of technology applications which have been discovered over the last century utilising solid-fluid flows. However, the importance of these systems is not limited to the realm of engineering. Geophysics (e.g. pyroclastic flows, [79]), medicine (e.g. blood flow through heart valve, [83]) as well as bio-engineering (blood analysis using microfluidic devices, [59]) are only a few examples which illuminate the breadth and multidisciplinary nature of solid-fluid flows.

Amongst the wide variety of natural processes in which solid-fluid flows can occur, the formation of rain droplets in the cloud is of critical importance to humanity. Fig. 1.1a show a cumulonimbus cloud over Africa, the rain this type of cloud delivers is crucial to the livelihoods and survival

(a)

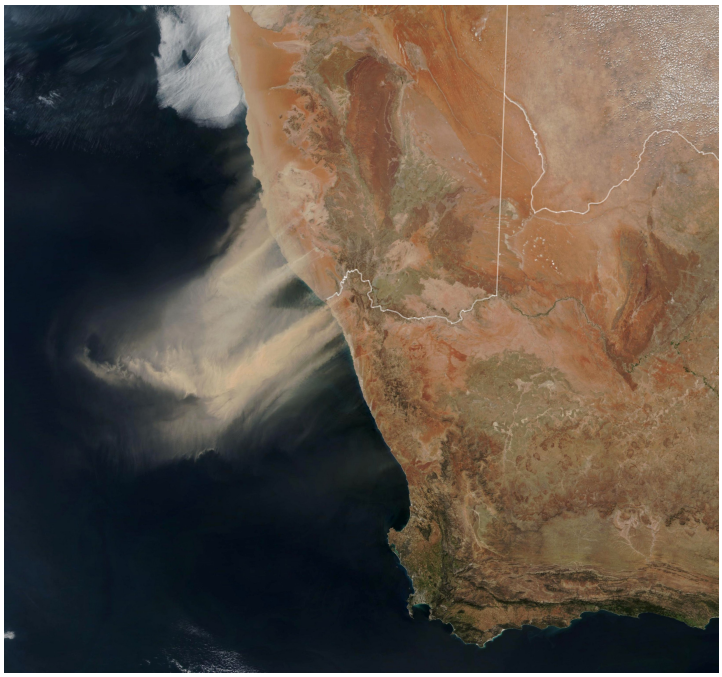

(b)

Figure 1.1: Examples of natural processes in which solid-fluid systems arise. (1.1a) Cumulonimbus cloud over Africa, (taken from NASA Earth Observatory [15]); (1.1b) sand storm over Namibian coast, (taken from NASA Earth Observatory [26])

for millions of people in the developing world. Better understanding the dynamics within these clouds, could lead to better precipitation predictions. Ravichandran and Govindarajan [88] has shown that interparticle collision in these clouds could be an important mechanism in the growth of raindrops. However, clouds are not the only interesting solid-fluid systems.

Sand storms have a massive impact on the climate of our planet, and they can be vast in extent. Fig. 1.1b shows a sand storm over Namibian coast, blowing huge amounts of sand and dust into the Atlantic Ocean. These storms effect can have planetary-scale effects, the dust and sand transported by Saharan storms is a major source of soil phosphorus for the Amazon rain-forest, as discussed by Okin et al. [80]. However, the mechanisms behind to initial entrainment of the sand particles into the air are not fully understood,[102].

The dynamics of solid-fluid systems are of surpassing industrial importance. For example, in the oil/gas industry, understanding the behaviour of methane clathrates slurries in sub-sea pipelines is critical towards preventing plugging, which can lead to significant accidents such as the Gulf of Mexico disaster. Plugging is a result of highly complex phenomena driven by interactions between a flowing fluid (such as oil) and suspended solid particles (such as hydrate crystals) that can either lead to hydrodynamic clustering or repulsion between suspended solids. It is still unclear what physics is the precursor to such clustering, and there is some evidence that the wakes generated as a solid particle moves have a role [23]. The process dramatically alters the apparent rheology of the slurry. Hence the industry relies on empiricism to design subsea pipelines, an of which can be seen in Fig. 1.2b.

Interest in deep-water drilling has rebounded following a brief lull in the aftermath of the April 2010 Gulf of Mexico disaster in the Macondo Prospect oil field. However, deeper wells and mature fields present increased water fractions posing significant risks to flow assurance such as hydrate-plugging. This process dramatically alters the apparent rheology of the slurry, which can have severe consequences if the pipeline cannot cope with the dramatic change in fluid properties.

The engineering importance of these flows is not only confined to pipelines. In the chemical industry, solid-fluid systems are also ubiquitous. Ranging from filtration to crystallisation, the number of industrial importance op-

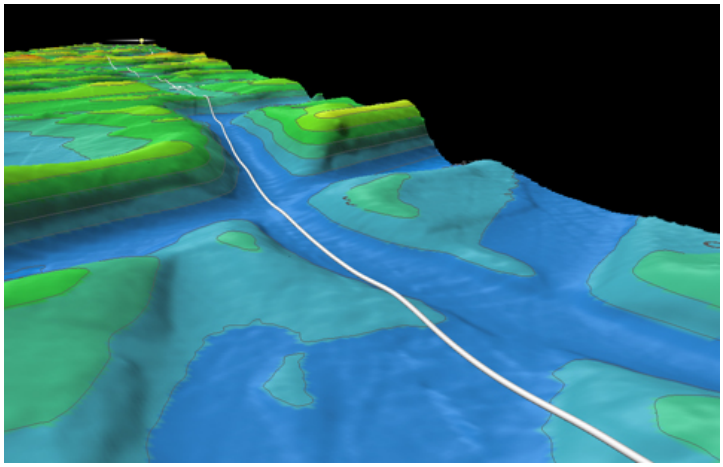

(a)

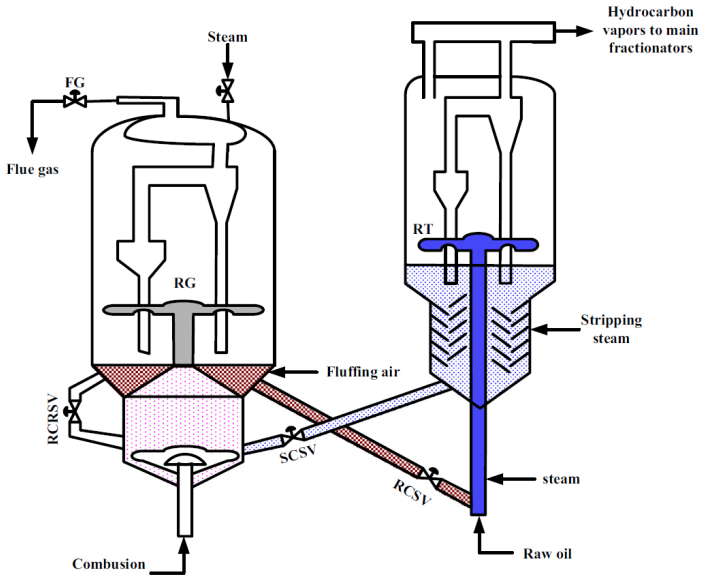

(b)

Figure 1.2: Examples of engineering processes which utilise solid-fluid flows. (1.1a) Subsea natural gas and oil pipelines, (taken from Subsea Engineering Associates [103]); (1.1b) fluidised-bed catalytic cracking reactor unit (taken from Jarullah, Awad and Mujtaba [49]).

erations that process solid-fluid systems are vast. However, fluidisation such as in catalytic cracking of hydrocarbons is of interest due to the energy demands of the process. Fig. 1.2b, shows a schematic of a fluidised-bed catalytic cracking unit, in which long-chain hydrocarbon vapour is passed through a fluidised bed of solid catalyst pellets and as a result broken down into shorter chain hydrocarbons, [101]. The design on these units is based on empirical relations since up to recently, and it has not been possible to model these systems numerically. It is desirable to develop a deeper understanding of the role of solid-fluid interactions in these processes and its relation to heat and mass transfer. Recently, thermal management of microelectronics has gained importance to help energy efficiencies in data centres and also increasing the lifetimes of microelectronic devices. An important method is by using phase-change coolants such as refrigerants that evaporate on contact with the processor and the ensuing vapour needs to be condensed in order to recycle the coolant. In the condenser, the ensuing vapour cloud comes in contact with cooler surfaces to nucleate and thus condense. It is of paramount importance to condense all of the refrigerant vapour and hence the dynamics of the vapour clouds is particularly important.

Elucidating, through modelling and simulations, the complex dynamics arising in solid-fluid systems is consequently the motivation of this work.

1.1 AIM AND OBJECTIVES

The objective of this work to obtain a comprehensive characterisation of the complex dynamics of immersed solid-fluid systems in both viscous and inviscid flows. This investigation was carried out by a combination of analytical and numerical techniques: (i) direct numerical simulations of resolved full-coupled solid-fluid systems, (ii) analysis the Kirchhoff-Clebsch equations for the case of inviscid flows, and (iii) characterising dynamics through advanced techniques such as recurrence quantification analysis. Additional objectives were to understand the effect of the immersed solid's motion on the mixing on the fluid and how viscosity gradients change the dynamics of solid-fluid systems. The results from the analytical and numerical methods are in the first instance compared to obtain a validation of

the capabilities of the solver developed in-house to capture the inviscid regime and then further extended to the viscous regime. Finally, our solver was extended to included solid-solid interactions via the implication of a composite contact model. The objectives can thus be summarised as:

- In-depth analysis, including validation, of the dynamics of a single solid immersed in inviscid and viscous environments.
- Generation of regime maps for the parameter space for single solid-fluid systems, identifying the parameters responsible for chaotic and periodic behaviour.
- Understanding, the influence of the motion of an, immersed solid on the mixing of the local fluid environment.
- Quantifying the effects of viscosity gradient driven migration of solids
- Extending the numerical solver to include contact models for solid-solid interactions in the simulation domain. This would include an account for hydraulic forces and contact forces.
- Validating the contact solver in the case of two settling spheres, against the experimental observations and theoretical predictions.

1.2 DISSERTATION OUTLINE

The remainder of this work is organised in the following manner. An overview of the most relevant studies in the field of solid-fluid systems is given in Chapter 2. Particular emphasis is giving upon the modelling approaches that have been developed to describe the complex dynamics of solid-fluid systems. The analytical and numerical techniques employed herein to quantify and investigate these dynamics are described in depth in Chapter 3. The results of the investigation of the chaotic dynamics of a single immersed solid in fluid given in Chapter 4. Chapter 5 pertains to the effects of the motion of a solid through a fluid marked with a tracer. This chapter also explains the effects of these dynamics on mixing and the influence of viscosity gradients. Extending the numerical solver to include contact models for solid-solid interactions in the simulation domain, is

shown in Chapter 6. Lastly, conclusion and future work are presented in Chapter 7.

2

LITERATURE REVIEW

The literature on solid-fluid systems is immense. Solid objects immersed in fluid demonstrate highly complex dynamics in both spatial and temporal scales and are central to a wide range of applications in nature and industry. For example, ice particles in clouds, tsunamis [one instance was the unusually large earthquakes inferred from tsunami deposits along the Kuril trench [77]], sediment transport near river beds [72], in fluidised beds [14], ore refining with slurry flow [27], hydrate transport in petroleum pipelines [23] and motion in vapour clouds [88].In all these applications, the solid-fluid motion is a strong function of the shape of the solid, and the complex two-way coupling between the solid and the nearby environment, which can result in hydrodynamic clustering of solids - eventually leading to chemical agglomeration or physical adhesion. It is still unclear what physics is a precursor to such clustering, and there is some evidence that the wakes generated as a solid particle moves have a role [23]. However, in this chapter, we will review only a subset of that corpus. These areas are the following, a review of the numerical simulation techniques used to simulate solid-fluid systems. Then hydrodynamic interactions between the fluid and solid and interparticle interaction will be covered. Lastly, we will review the special case of a solid in an inviscid flow.

2.1 REVIEW OF SIMULATION METHODS

We are faced with an embarrassment of riches when it comes to the number of numerical methods that are available to deal with fluid systems, [85]. When we look at extending them to include solids, the problem becomes much more difficult. The root of the problem arises from the Cauchy equation:

$$\frac{\partial \boldsymbol{j}}{\partial t} + \nabla \cdot \mathcal{F} = \boldsymbol{s}. \tag{2.1}$$

Eq. 2.1 is the most general non-relativistic momentum transport equation available for continua.

Where, $\boldsymbol{j}$ is the momentum density vector, $\mathcal{F}$ is the flux associated to the momentum density, $\underline{\boldsymbol{\sigma}}$ is the stress tensor, and $\boldsymbol{s}$ is the body force density vector. These are defined in the following manner:

$$\boldsymbol{j} = \rho \boldsymbol{u}, \quad \mathcal{F} = \rho \boldsymbol{u} \otimes \boldsymbol{u} - \underline{\boldsymbol{\sigma}}, \quad \text{and} \quad \boldsymbol{s} = \rho \boldsymbol{g}. \tag{2.2}$$

In addition we need to ensure the mass of the system is conserved. Therefore we have the following constraint:

$$\frac{\partial \rho}{\partial t} + \nabla \cdot (\rho \boldsymbol{u}) = 0. \tag{2.3}$$

Where, ρ is density. Individually both the fluid and the solid are governed by the Cauchy equation, in the continuum limit. There are three prominent methods in literature to solve this problem.

The most widely used method for these problems is the Eulerian continuum approach. It is a very natural extension of Eq. 2.1 and 2.3. By treating the solid and fluid as inter-penetrating mixtures the Eulerian continuum approach allows us to modify the stress tensor, $\underline{\boldsymbol{\sigma}}$ using continuum theory. Zhang and Prosperetti [113], Fan and Zhu [30], and Drew and Passman [24] have all presented results using this method. This method describes the fluid and solid as behaving like a nonhomogeneous phase. An additional term is introduced into the Cauchy equation to which arises from the interactions between the phases. Eq. 2.1 and 2.3, take the following forms under these assumptions, for the continuity equation:

$$\frac{\partial (a_f \rho_f)}{\partial t} + \nabla \cdot (a_f \rho_f \boldsymbol{u}) = 0, \tag{2.4}$$

$$\frac{\partial (a_s \rho_s)}{\partial t} + \nabla \cdot (a_s \rho_s \boldsymbol{v}) = 0. \tag{2.5}$$

The volume fractions are defined as a_f and a_s of fluid and solid phases respectively The sum of the volume fractions must reach unity. Further, ρ_f and ρ_s are the fluid and solid densities, respectively, while $\boldsymbol{u}$ is the fluid velocity and $\boldsymbol{v}$ is the solid velocity. The momentum equations for the two phases are given as:

$$\frac{\partial(a_f\rho_f\boldsymbol{u})}{\partial t} + \nabla\cdot(a_f\rho_f\boldsymbol{u}\otimes\boldsymbol{u}) = -a_f\nabla p + \nabla\cdot(a_f\boldsymbol{\tau_f}) + \boldsymbol{F}_f + a_f\rho_f\boldsymbol{g}, \tag{2.6}$$

$$\frac{\partial(a_s\rho_s\boldsymbol{v})}{\partial t} + \nabla\cdot(a_s\rho_s\boldsymbol{v}\otimes\boldsymbol{v}) = -a_s\nabla p - \nabla p_s + \nabla\cdot(a_s\boldsymbol{\tau_s}) + \boldsymbol{F}_f + a_s\rho_s\boldsymbol{g}, \tag{2.7}$$

where $\boldsymbol{g}$ is the gravitational acceleration. p and p_s are defined as the fluid and solid pressures, respectively. $\boldsymbol{\tau_f}$ is the fluid stress tenor and $\boldsymbol{\tau_s}$ is the solid stress tensor. An additional model for this term is required to close the modified governing equations, $\boldsymbol{F}_f$ and is called the inter-phase force transfer. In the literature, this interaction term has been well studied, by Syamlal [104], Yali Tang et al. [111], Gidaspow [35], and Di Felice [19].This model can be very efficiently implemented and is amenable to parallelisation since the solid and fluid motion are modelled in the same domain. However, this method obscures the details of the coupled interactions and makes them difficult to understand. This method has been widely used in the multi-phase flow community.

An alternative approach to the simulation of these systems is the Lagrangian method. In this method the fluid is described as a Eulerian domain using a form of the Cauchy equations, most typically the Navier-Stokes equation. The solids, on the other hand, are treated as a Lagrangian domain with Newton's laws governing their motion. A hydrodynamic force is applied to the solids to account for the fluid's effect on the solids and vice-versa. The form of this force depends on the model chosen for coupling. Boivin, Simonin and Squires [7] proposed the following equations of motion for the Lagrangian solids:

$$\frac{d\boldsymbol{x}_i}{dt} = \boldsymbol{v}_i \tag{2.8}$$

$$\rho_s\frac{d\boldsymbol{v}_i}{dt} = \rho_s\boldsymbol{g}_i + \oint_S[-p\underline{\boldsymbol{\delta}}_{ij} + \frac{\mu}{\rho_f}\frac{\partial\boldsymbol{u}_i}{\partial x_j}]\boldsymbol{n}_\Gamma dS, \tag{2.9}$$

where is $\boldsymbol{x}$ is the position of the centriod the solids, $\boldsymbol{n}_\Gamma$ is the outward pointing normal to the surface and $\underline{\boldsymbol{\delta}}_{ij}$ is the Kronecker delta symbol. The coupling between the fluid and solids can be either one-way, in which the

fluid affects the motion of the solids, but there is no back reaction or a full two-way couple where the solids affect the fluid domain. The one-way coupling variant is advantageous in situations dealing with a large number of small particles suspended in a fluid, in particular when their volume fraction is low such that the presence of solids does not affect the flow significantly. These model have been used in modelling rain droplets in clouds, [88]. The one-way coupling reduces the computational demands of the simulation and allows many more particles to be simulated compared to the simulation approach. The two-way method can be used in situations where the exchange of momentum between the solid and fluid domain is essential. This method can be extended to calculate the inter-particle stress empirically c.f. work done by Andrews and O'Rourke [2] and Snider, O'Rourke and Andrews [99]. This effect is typically neglected in the Lagrangian tracking methods and the Euler continuum approach.

Lattice Boltzmann method, (LBM), is another approach to solve solid-fluid systems. LBM is a very computational efficient approach and is applicable to modern computational architectures, such as graphical processing units and parallel simulation clusters. LBM stands in stake contrast to the other approaches, so far reviewed. It is not based on the Cauchy equations, Eq. 2.1, instead it is based on the Boltzmann equation: [60]:

$$\frac{\partial f}{\partial t} + \xi_\beta \frac{\partial f}{\partial x_\beta} + \frac{F_\beta}{\rho} \frac{\partial f}{\partial \xi_\beta} = \Omega(f), \tag{2.10}$$

where $f(x, \xi_\beta, t)$ is the particle distribution function. It can be seen as a generalisation of density ρ which also takes the microscopic particle velocity ξ_β into account.Additionally, F_β/ρ is the specific body force and $\Omega(f)$ is the *collision operator*.

The Boltzmann equation models the time evolution of the probability distributions of microscopic particles possessing specific properties; it is not a continuum approach. Instead, by placing mesoscopic-averaged constraints on the probability distributions, to ensure mass and momentum conservation, it is possible to recover the Navier-Stokes equation in the continuum limit. This done by the MRT method or prescribing a form

to the *collision operator*. The BGK collision model is most widely used in practice, [60] and takes the form:

$$\Omega(f) = \frac{1}{\tau}(f - f^{eq}) \tag{2.11}$$

,

where τ is the relaxation time and it determines the speed at the systems moves towards equilibrium, f^{eq}, thereby specifying the transport coefficients for the fluid such as viscosity and heat or mass diffusivity.

Owing to its computational advantage LBM has been extensively used to simulate solid-fluid systems,[21], [87], [6] and recent advances have been made by Krüger et al. [58]. The advantages of this approach are most clearly demonstrated by Ladd [62], by simulating 32000 spherical particles in a suspension using a parallel simulation. This method is not without its drawbacks and trade-offs, due to the nature of the mesoscale averaging in density, the flows that are simulated are never fully incompressible, [60]. Similarly, solids in LBM are not entirely rigid; instead, they are defined as a collection of gird-free points bounded together.

Lastly, direct numerical simulation, (DNS), can be used to investigate solid-fluid systems. In this approach the all the coupled hydrodynamic forces are calculated for particle laden-flow. This allows for the resolution of the instantaneous motions of both the fluid and the solids. The governing equations in this model for the flow in the presence of immersed solids are:

$$\nabla \cdot \boldsymbol{u} = 0, \tag{2.12}$$

$$\frac{\partial \boldsymbol{u}}{\partial t} + \boldsymbol{u} \cdot \nabla \boldsymbol{u} = -\frac{1}{\rho_f}\nabla p + \nu \nabla^2 \boldsymbol{u} + \delta \boldsymbol{f_S}. \tag{2.13}$$

Here, ν is the kinematic viscosity of the fluid, $\boldsymbol{f_S}$ is a general body force term characterising the influence of the immersed solid and $\delta = |\nabla a_s|$ is the so-called interface delta function whose value is unity at the surface of

the immersed body and zero elsewhere. The equations for the solids are the following:

$$m\frac{\boldsymbol{dv}}{\boldsymbol{dt}} = \iint_A \rho_f \boldsymbol{f_S} \cdot \boldsymbol{r} dA \tag{2.14}$$

$$\mathcal{I}_s\frac{\boldsymbol{d\Omega}}{\boldsymbol{dt}} = \iiint_V \rho_f \boldsymbol{f_S} \times \boldsymbol{r} dV \tag{2.15}$$

where V is the volume of the solid. Note that $\boldsymbol{f_S}$ is the hydrodynamic force applied by the fluid on the solid-fluid interface (i.e. the solid surface). For any point on the surface of the solid, $\boldsymbol{r}$ is the relative location of that surface point to the mass centre of the solid. $\boldsymbol{f_S}$ is a key coupling parameter between the fluid and solid and will be further discussed in Chapter 3.

Additionally, this method provides a wealth of information on the fluid-solid coupling, such as the pressure and stress distribution over a solid's surface. This level of detail, allows this method to be used to investigate phenomena that the previous approaches would have difficulty in simulating. DNS might provide the only numerical tool that can study the non-linear dynamics of particle motion alongside ensuing flow instabilities. It can also predict complex outcomes solid-solid and solid-wall interactions, such as hydrodynamic cluttering. However, there exists a trade-off for using DNS; it is computationally costly. This expense limits the scale of systems that we can investigate. Johnson and Tezduyar [51] reported their simulation of flow-particle interaction with 100 particles, and this is at least an order of magnitude smaller than what can be done using the Lagrangian tracking method.

2.2 DNS FOR SOLID-FLUID PROBLEMS

The general equation describing fluid flow, 2.1 and 2.3 can be simplified by neglecting the changes in the density of the fluid, leading to the Navier-Stokes equations. For the remainder of this thesis, we will only be interested in constant density flows, Gurris and Turek [38] have developed techniques for compressible fluid particle-laden flows. Initial DNS studies of particle-laden flows were limited by the computational cost of the meshing strategies they used. They typically used either body-fitted or un-

structured meshes. However, the high mesh density needed to capture complex geometry and the costs of transient mesh regeneration at every time-step for the moving solid boundary was prohibitive. Tezduyar, Liou and Ganjoo [108] used this method to investigate the flow induced by drafting cylinders. However, they encouraged numerical problems with the body-fitted meshing strategy. It did not handle the transient changes in the spatial domain caused the moving solid boundary well. These limitations inspired researchers to find more robust simulation approaches. Fig. 2.1, shows an example of a body-fitted mesh being superimposed on to a global Cartesian mesh, interpolation is require to transfer information between to two meshes, [1].

The arbitrary Lagrangian-Eulerian method, (ALE), is a much robust approach. ALE uses a combination of an unstructured finite element mesh and a reformation of the fluid-solid momentum equations to compute the trajectories of the system, [25]. This method has been used to study the two-dimensional dynamics of circular and elliptical cylinders sedimenting in a channel, and this work was carried out by Feng, Hu and Joseph [32]. Fig. 2.2, shows a rising bubble simulated using ALE, by Duarte, Gormaz and Natesan [25]. Using the same method they also investigated the effects of solid-wall interaction on the settling of rotating cylinders, [33]. They also present results for circular particles at $Re = 100$. Huang et al. [42] investigating the hydrodynamic interactions of circular and elliptical solids in different flow conditions, including Couette flows, Passion flows, and in sedimentation in both Newtonian and Oldroyd-B fluids. ALE has also been extended to viscous-elastic and shear-thinning fluids, by Huang, Hu and Joseph [43]. The studies so far have primarily focused on sedimentation. However, Patankar [81] used the ALE methodology to investigate the rheology of suspension using various hydrodynamic conditions. Keh and Huang [52] also extended the ALE to simulate tumbling kissing dynamics of multi-sphere particles in three-dimensional flows.

The distributed Lagrange multiplier method, (DLM), is an alternative to ALE. This methodology has an important feature; the governing fluid equations are applied both inside and outside the solid boundary, [95]. The fluid that is inside the solid boundary is constrained to have the same motion as the solid by using a system of Lagrange multipliers. This multiplier term behaves similarly to the pressure field, ensuring incompressibility constraint in the fluid. It multiplier becomes a generalised source

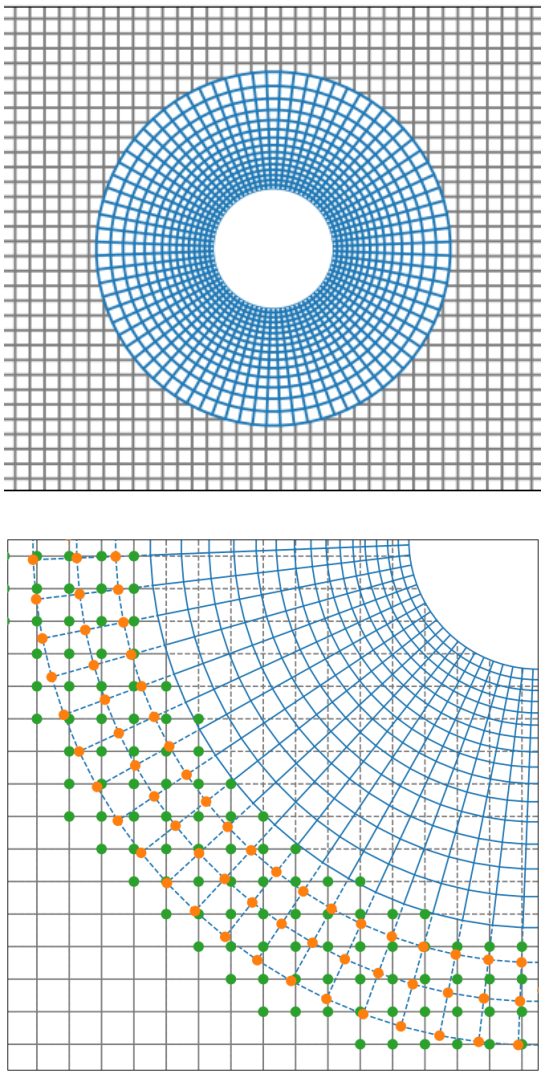

Figure 2.1: Body fitted mesh: (a) Cylindrical grid fitted to a body superimposed on top of global Cartesian grid. (b) communication between grids is accomplished by interpolation between the Cartesian grid points and the cylindrical grid point. Cartesian marked with green dots and cylindrical point marked with orange dots. (Figure taken from Aarnes, Haugen and Andersson [1])

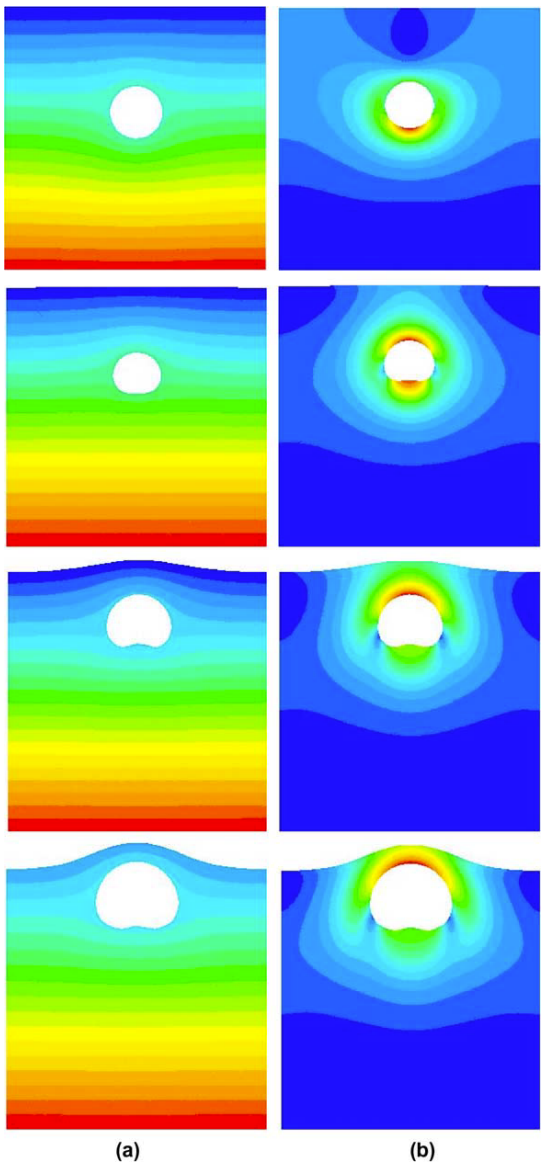

Figure 2.2: Bubble rising through fluid column, simulated using ALE.(a) Shows the contours of pressure around the bubble over time, (b) shows magnitude of the fluid velocity, $\boldsymbol{u}$ at the same time t (Figure taken from Duarte, Gormaz and Natesan [25])

term in the fluid equations. Hyman [46] was the first to publish work on the approach. The introduction of boundary constraints later refined it, this done by Glowinski, Pan and Périaux [36]. Much like ALE, DLM has been extended by further development to cover viscoelastic fluids [96].

The immersed boundary method (IBM) is the final method that will be reviewed. It was initially developed to study blood flow through vessels. Peskin [82] developed the method to handle deformable bodies (since red blood cells deform significantly in their passage round the body). In the interim, there have been improvements to the method, and it has been used in many different applications. Throughout its evolution it has cross-pollinated with DLM and now several variants exist. IBM has been employed in the thesis to study solid-fluid systems. A brief review of the method is presented in the following section.

2.3 IBM FOR SOLID-FLUID COUPLING

In the methods to simulate solid-fluid systems such as ALE, the fluid domain is partially occupied by the solids. This problem means that the resulting fluid domain is irregular and no longer simply-connected. This topological complexity limits these to using unstructured meshes for the spatial discretisation. These unstructured meshes are built up using a combination of tetrahedral, prismatic and hexahedral elements and have several disadvantages when compared to Cartesian meshes. These disadvantages mainly revolve around the computational difficulty of generating unstructured meshes of comparable quality to Cartesian mesh for a given resolution. The quality of the underlying mesh can have a significant impact on the accuracy of any DNS simulation, [34]. Furthermore, the extent of numerical error when using unstructured meshes is difficult to quantify as compared to structured cartesian meshes. A non-uniform unstructured mesh can be a significant source of error in these simulations, especially near solid boundaries and walls. This results in these simulations being unable to capture solid-solid interactions accurately, such has hydrodynamic clustering in fluid flows. Since the clustering creates localised pockets of a high solid fraction with the domain. Additionally, these DNS methods require the fluid mesh to be regenerated at each time-step to account for the motion of the solids, [107]. The control of the mesh quality for unstruc-

tured meshes at every time-step becomes a significant technical challenge [97].

Avoiding the use of unstructured meshes and iterative mesh regeneration is the main advantages of IBM and makes it a novel approach in the field of solid-fluid simulations. The approach treats the interaction between the solid and fluid has source terms in the governing equations. This term means that locally, the motion of the solids matches the motion of the fluid. The fluid flow is governed by the Navier-Stokes equations and for the orginal case presented by Peskin [83], it was solved on a Cartesian grid. The IBM is represented by a set of elastic interfaces and the location of these interfaces is tracked in a Lagrangian fashion by a collection of massless points that move with the local fluid velocity. Thus, the coordinate $\boldsymbol{X}_k$ of the k^{th} Lagrangian point is governed by the equation

$$\frac{\partial \boldsymbol{X}_k}{\partial t} = v(\boldsymbol{X}_k, t) \tag{2.16}$$

The stress $\boldsymbol{F}$ and deformation of these elastic interface is related by a constitutive law. In Peskin [83] original blood flow study the force applied by the interface was computed using Hooke's law. The effect of the IBM on the surrounding fluid is captured by transmitting the interface stress to the fluid through a forcing term, $\boldsymbol{f_S}$, in the momentum equations, which is given by:

$$f_m(\boldsymbol{x}, t) = \sum_k F_k(t)\delta(\|\boldsymbol{x} - \boldsymbol{X}_k\|). \tag{2.17}$$

This fundamental idea has inspired many variations, like the direct forcing approach, [29] and the immersed interface method [65]. These variations typically differ in their treatment of continuity and the no-slip conditions on the solid interface. The common thread is that by capturing the interaction in general source-term allows the fluid domain to remain intact and simply-connected. Therefore, IBM can be used on Cartesian meshes and then reaps the benefits of the simplified mesh generation process, [75]. This simplification is especially advantageous when the solid would have required a very complex body-fitted mesh since the Cartesian mesh does

not need to be regenerated on every time-step, when the solid moves, additional performance benefits are obtained. These two advantages combine to reduce the computation and memory requirements of IBM when compared to other DNS methods. However, the use of Cartesian meshes is a double-edged sword; the majority of IBM solvers available at this time are built on the assumption of a fixed Cartesian mesh with uniform mesh resolution. This means that in some instances, the computational resources needed for simulation would dramatically increase, as the need for a high mesh resolution needed over a limited area is imposed on the whole simulation.

In this thesis, a fluid-solid solver named the Gerris Immersed Solid Solver (GISS) was used to investigate solid-fluid interaction. This solver has been developed in-house by Shui et al. [94]. It leverages a novel approach to avoid the problems of uniform meshes faced by other IBM solvers. GISS comprises two sub-solvers, the solid motion solver which implements Newton's equations of motion for the solids smoothly coupled to the fluid flow sub-solver based on Gerris. Gerris is an open-source fluid solver that has been developed by Popinet [86]. Gerris solves the Navier-Stokes equations with an adaptive mesh projection method. The solid-fluid interaction on the solid boundaries is represented using a volume of fluid approach, called the embedded solid method. It was first proposed to study complex solid geometries in ideal flows by Khokhlov [53]. The computational fluid domain is adaptively discretised using a quadtree for the two-dimensional case and an octree in the three-dimensional case. The data structure can automatically refine a given mesh cell by splitting the root cell into either 4 or 8 leaf cells while maintaining the Cartesian nature of the mesh over the whole domain. This "tree mesh adaptation" is much simpler than the conventional mesh adaption based on body-conforming unstructured meshes, resulting in a reduced computational cost to both to other IBM implementations and the conventional methods. Leveraging these advantages GISS can theoretically handle an arbitrary number of solids in the fluid domain, limited only by the computational resources available to it. Additional the solids can have complex geometry allowing for the simulation of the hydrodynamic interaction between these solids. In thesis, Gerris is used to study the complex dynamics of solid-fluid systems. Details of GISS are explored in section 3.1.

2.4 IMMERSED BODIES IN INVISCID FLOWS

One of the objectives of this thesis is to investigate dynamics of an immersed ellipsoid in an inviscid or viscous flow environment. Gustav Kirchhoff in the mid-19th century [54] was probably the first to study the motion of an immersed solid moving through an ideal fluid. He showed that a set of ordinary differential equations could describe the motion of a body through an incompressible, inviscid and irrotational flow:

$$\frac{d}{dt}\frac{\partial K_{tot}}{\partial \boldsymbol{v}} + \boldsymbol{\Omega} \times \frac{\partial K_{tot}}{\partial \boldsymbol{v}} = 0, \tag{2.18}$$

$$\frac{d}{dt}\frac{\partial K_{tot}}{\partial \boldsymbol{\Omega}} + \boldsymbol{\Omega} \times \frac{\partial K_{tot}}{\partial \boldsymbol{\Omega}} + \boldsymbol{v} \times \frac{\partial K_{tot}}{\partial \boldsymbol{v}} = 0. \tag{2.19}$$

Here K_{tot} is the total kinetic energy of the fluid and solid, $\boldsymbol{\Omega}$ and $\boldsymbol{v}$ are the angular and linear velocities of the solid respectively. These equations may be seen to be a generalisation of Euler's equation for the motion of a body through a vacuum [73]. Later, Lamb [63] showed that for spheres and general ellipsoids, a closed-form expression exists for the hydraulic force and torque in the Kirchhoff equations. The reduction of the problem to a set of ordinary differential equations is a dramatic simplification of the problem, which otherwise has only very recently entered the realm of feasibility to simulate directly. Jeffery [50] analytically showed that a single neutrally buoyant ellipsoid in shear flow adopts positions with least energy dissipation. This action corresponds to rotary motion, the orbit tracked by the ellipsoid under these conditions is the so-called *Jeffery's orbit*. At low Reynolds numbers when the effects of inertia are negligible, the solution was confirmed in several experiments by Taylor [106].

Kozlov and Onishchenko [57] re-investigated these equations using dynamical systems theory showing that the dynamics of an ellipsoid released in a quiescent inviscid fluid with arbitrary initial linear and angular velocity is integrable if at least two axes of revolution are equal. Later Aref and Jones [3] demonstrated by solving the relevant potential flow equations that an ellipsoid of revolution whose three axes are all different from each other can indeed display chaotic motion in an inviscid fluid, Fig 2.3 is the resulting orbits traced out by these ellipsoids for different initial conditions. In the limit of zero inertia, Yarin, Gottlieb and Roisman [112]

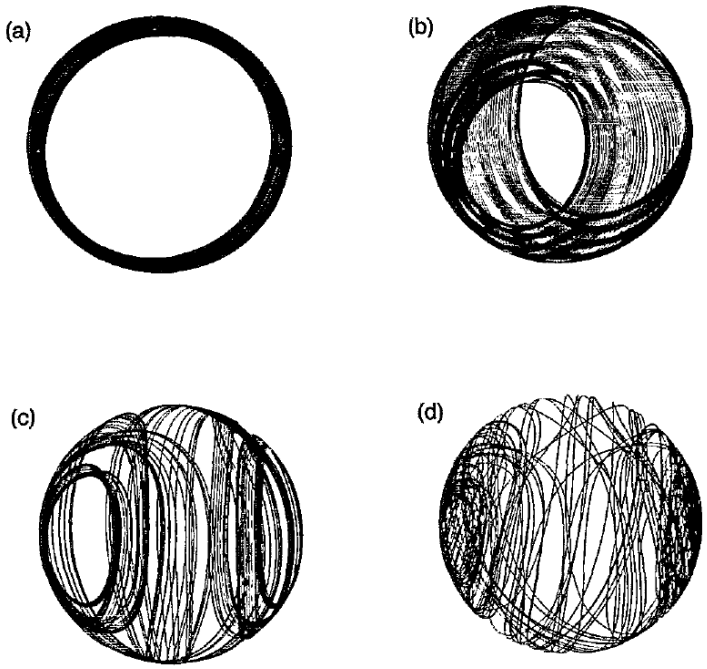

Figure 2.3: Orbits of triaxial ellipsoids for the four initial conditions. The trajectories shown are traced out by the tip of a marker, rigidly attached to the body, (Taken from Aref and Jones [3]).

demonstrated that an immersed tri-axial ellipsoid exhibits chaotic rotation. The effects of viscosity on the motion of single general ellipsoid have been studied in a paper by Rosén [89] in the context of low Reynolds number shear flows. Under those conditions, they found that the ellipsoid followed quasi-Jefferys and that the geometry strongly affected the stability of these orbits. Nevertheless, the effects of fluid inertia under viscous conditions have not been explored in much detail. In particular, the chaotic and periodic/quasiperiodic nature of these orbits needs clarification as a function of density and energy ratios.

Quantifying chaos and periodic/quasiperiodic behaviour for any non-linear dynamical system, including that of an immersed solid body in a fluid is a challenge in its own right. Any orbit tracked by a solid is chaotic if and only if it satisfies three signatures: a) incredible sensitivity to initial conditions, the so-called butterfly effect; b) demonstrates overlap of any region of phase-space with any other region, the so-called topological mixing principle and c) exhibits dense periodic orbits. First introduced by Eckmann, Oliffson Kamphorst and Ruelle [28], recurrence quantification analysis (RQA) is one of the methods of non-linear data analysis for

identifying and characterising behaviour. RQA measures the frequency and duration of recurrences in the phase space of a system within a small error called the recurrence threshold.

2.5 CONCLUSIONS

Given the literature on solid-fluid systems is vast, a brief review of the literature is given focusing purely on a) simulation methodologies of solving solid-fluid systems, b) direct numerical simulation approaches, c) immersed boundary methods and d) theoretical frameworks exploring immersed bodies

It can be seen that there is still a lack of knowledge relating to motion of general ellipsoids. It must also be reemphasised that most of the previous work has looked into stationary immersed solids, and its only recently the two-way fluid-solid interaction is amenable to calculate whilst ensuring free movement of the solid, due to increase in computational power. Thus, in this thesis, we are motivated by the following questions:

- Can the orbits tracked by immersed ellipsoids be ever chaotic? While the non-integrability theorem of Kozlov and Onishchenko [57] for a tri-axial ellipsoid states that under inviscid conditions, orbits tracked can be chaotic, this thesis (Chapter 4) will explore the role of geometry, and viscosity.

- Can such motion influence mixing? Such as those in vapour clouds or multicomponent atmospheres (Chapter 5)

- How do neighbouring solids influence such motion? We also present the theory for multi-body dynamics (Chapter 6).

3

METHODOLOGY AND PRELIMINARY VALIDATION

In this chapter, all the methodologies used in this thesis are described. We first begin with describing the methodology used for Direct Numerical Simulations in GISS. We also present a few basic validation cases concerning translation and rotation of a solid immersed in a fluid. We then focus on describing the methodology used to solve the Kirchoff-Clebsch equations for both single and multiple solids. Some contents of this chapter have been submitted as a paper for the Journal of Fluid Mechanics, currently under review.

3.1 DIRECT NUMERICAL SIMULATIONS USING GISS

The GISS numerical solver developed here comprises two sub-solvers: i) The Gerris flow solver and ii) the Immersed Solid Solver. A two-step solution strategy is used. First, the 3D flow equations around the body are solved using the Gerris Engine [86] to obtain velocity and pressure fields. These are then used to calculate the hydrodynamic force field on the surface of the immersed solid. Second, the calculated forces are passed on to the solid solver which calculates the new position of the immersed body using rigid body equations for translation and rotation. These steps allow for two-way solid-fluid coupling at every time step. The solver allows for arbitrary number of solids with arbitrary geometric features in six degree of freedom (6DOF) motion. The solver can perform dynamical quad/octree mesh optimisation in a Cartesian framework, which greatly simplifies the procedure for mesh generation.

3.1.1 *Fluid Solver: Governing Equations and Solution Methodology*

The fluid physics are solved using Gerris [86] which is based on a fractional step projection method suggested by Brown, Cortez and Minion [10]. In

this study, we consider the fluid to be incompressible and Newtonian and the immersed solid to be rigid and non-porous. Thus, the governing equations for the flow in the presence of such an immersed solid are:

$$\nabla \cdot \boldsymbol{u} = 0, \tag{3.1}$$

$$\frac{\partial \boldsymbol{u}}{\partial t} + \boldsymbol{u} \cdot \nabla \boldsymbol{u} = -\frac{1}{\rho_f} \nabla p + \nu \nabla^2 \boldsymbol{u} + \delta \boldsymbol{f_S}. \tag{3.2}$$

Here, ν is the kinematic viscosity of the fluid, p is the pressure, $\boldsymbol{f_S}$ is a general body force term characterising the influence of the immersed solid and $\delta = |\nabla a_f|$ is the so-called interface delta function whose value is unity at the surface of the immersed body and zero elsewhere, with a_f signifying the volume fraction of the fluid. In this work, periodic boundary conditions are applied on the fluid domain and a no-slip nonpenetration boundary condition is enforced on the immersed solid-fluid interface. Thus, if Γ indicates the immersed solid region then

$$\boldsymbol{u} = \boldsymbol{u}_\Gamma = \boldsymbol{v}, \tag{3.3}$$

$$\nabla p \cdot \boldsymbol{n}_\Gamma = 0. \tag{3.4}$$

Here, $\boldsymbol{n}_\Gamma$ indicates the normal to the solid domain. The projection method is based on Helmholtz-Hodge decomposition by which the velocity field $\boldsymbol{u}$ can be uniquely decomposed into a solenoidal (divergence-free) part and an irrotational part. We can rewrite the Eq. 3.1 and Eq. 3.2 in second-order in time and time-discrete semi-implicit forms, to get:

$$\nabla \cdot \boldsymbol{u}^{n+1} = 0, \tag{3.5}$$

$$\frac{\boldsymbol{u}^{n+1} - \boldsymbol{u}^n}{\Delta t} + [(\boldsymbol{u} \cdot \nabla)\boldsymbol{u}]^n = -\frac{1}{\rho_f} \nabla p^{n+1/2} + \nu \nabla^2 \boldsymbol{u}^n + \delta \boldsymbol{f}_{\boldsymbol{S}}^n. \tag{3.6}$$

Here, the superscript n denotes the variable at the time point of $t = n\Delta t$. (The coupling force, $\boldsymbol{f_S}$, from the solid dynamics is treated later in

Section 3.1.2.) With the help of an intermediate velocity field $\boldsymbol{u}^\star$, Eq. 3.6 can be divided into two equations:

$$\frac{\boldsymbol{u}^\star - \boldsymbol{u}^n}{\Delta t} + [(\boldsymbol{u}\cdot\nabla)\boldsymbol{u}]^n = \nu\nabla^2\boldsymbol{u}^n + \delta\boldsymbol{f}_{\boldsymbol{S}}^n, \tag{3.7}$$

$$\frac{\boldsymbol{u}^{n+1} - \boldsymbol{u}^\star}{\Delta t} = -\frac{1}{\rho_f}\nabla p^{n+1/2}. \tag{3.8}$$

It is possible to calculate the value of $\boldsymbol{u}^\star$ explicitly through Eq. 3.7 with the known velocity field $\boldsymbol{u}^n$, and with the help of Eq. 3.5, and by taking the divergence on both sides of the Eq. 3.8, we obtain

$$\nabla^2 p^{n+1/2} = \frac{\rho_f}{\Delta t}\nabla\cdot\boldsymbol{u}^\star. \tag{3.9}$$

Eq. 3.9 is a typical Poisson equation, the solution of which will reveal the pressure field at $n+1/2$ time step. Substituting $\boldsymbol{u}^\star$ and $p^{n+1/2}$ back into Eq. 3.8, we then obtain the velocity field at the next time step as follows.

$$\boldsymbol{u}^{n+1} = \boldsymbol{u}^\star - \frac{\Delta t}{\rho_f}\nabla p^{n+1/2}. \tag{3.10}$$

3.1.2 *Solid Motion Solver in GISS and Coupling with Fluid Solver*

The governing equations for the solid are Newton's second law built on the global coordinate system which will remain stationary during the simulation. The solid is free to perform full 6 degrees-of-freedom (6DOF) motion. While any number of solids can be immersed in the framework, computational effort rises with increasing number of solids. The calculation is powered by the Open Dynamics Engine (ODE, developed by

Smith [98]), which uses the following force and moment balance equations:

$$m\frac{\boldsymbol{dv}}{\boldsymbol{dt}} = \iint_A \rho_f \boldsymbol{f_S} \cdot \boldsymbol{r} dA, \tag{3.11}$$

$$\mathcal{I}_s\frac{\boldsymbol{d\Omega}}{\boldsymbol{dt}} = \iiint_V \rho_f \boldsymbol{f_S} \times \boldsymbol{r} dV, \tag{3.12}$$

where V_s is the volume of the solid. Note that $\boldsymbol{f_S}$ is the hydrodynamic force applied by the fluid on the solid-fluid interface (i.e. the solid surface). For any point on the surface of the solid, $\boldsymbol{r}$ is the relative location of that surface point to the mass centre of the solid, $\boldsymbol{r}_\perp$ is the positional vector of the surface point perpendicular to the axis of rotation of the solid, $\boldsymbol{x}$ is the instantaneous translational position of the centriod of the body and $\boldsymbol{\theta}$ is the instantaneous set of Euler angles of the surface point with reference to the global coordinate system. Evidently, $\boldsymbol{f_S}$ is a key coupling parameter between the flow and solid solvers. Eq. 3.12 is built on a local coordinate system associated with the solid with the origin at its centre of mass and moves synchronously during the simulation. Though the orientation of the solid is represented by Eulerian angles at each timestep, the internal calculations on the rotation are based on quaternions to avoid the so called "Gimbal lock" singularity [61]. The conversion between them are as follows:

$$\begin{bmatrix} q_0 \\ q_1 \\ q_2 \\ q_3 \end{bmatrix} = \begin{bmatrix} \cos(\theta_x/2)\cos(\theta_y/2)\cos(\theta_z/2) + \sin(\theta_x/2)\sin(\theta_y/2)\sin(\theta_z/2) \\ \sin(\theta_x/2)\cos(\theta_y/2)\cos(\theta_z/2) - \cos(\theta_x/2)\sin(\theta_y/2)\sin(\theta_z/2) \\ \cos(\theta_x/2)\sin(\theta_y/2)\cos(\theta_z/2) + \sin(\theta_x/2)\cos(\theta_y/2)\sin(\theta_z/2) \\ \cos(\theta_x/2)\cos(\theta_y/2)\sin(\theta_z/2) - \sin(\theta_x/2)\sin(\theta_y/2)\cos(\theta_z/2) \end{bmatrix}, \tag{3.13}$$

$$\begin{bmatrix} \theta_x \\ \theta_y \\ \theta_z \end{bmatrix} = \begin{bmatrix} \text{atan2}[2(q_0q_1 + q_2q_3), 1 - 2(q_1^2 + q_2^2)] \\ \text{asin}[2(q_0q_2 - q_3q_1)] \\ \text{atan2}[2(q_0q_3 + q_1q_2), 1 - 2(q_2^2 + q3^2)] \end{bmatrix}. \tag{3.14}$$

Here θ_i denotes the rotation angle around i axis of the instantaneous solid coordinate system and q denotes the set of resulting quarternions.

On the boundary, the solid is represented by the volume fluid fraction (a_f) and surface fluid fraction (s_d, where d is the direction of the face) of the fluid together. Both a_f and s_d are set to the value of 1 in pure fluid, 0 in the pure solid, and any number between 0 and 1 means a mixed cell on the solid-fluid interface. This variant of immersed boundary method is usually referred as the "Cartesian grid method" or the "embedded solid method" [18, 109].

To calculate the force applied on each cell, it is essential to know the area and direction of the interface which can be calculated approximately by:

$$\boldsymbol{A} = (s_{x-} - s_{x+}, s_{y-} - s_{y+}, s_{z-} - s_{z+}) \cdot \Delta x^2. \tag{3.15}$$

As shown by the example in Fig. 3.1, the area vector of the interface cutting the cell is $(-1,-1)\cdot\Delta x$, $|\boldsymbol{A}|$ is the area of the numerical interface with the direction of inward-pointing normal. Therefore, the body force tensor interpreted by the solid solver, $\boldsymbol{F}$ is:

$$\boldsymbol{F} = \iint_A \rho_f \boldsymbol{f_S} \cdot \boldsymbol{r}, \tag{3.16}$$

$$= \begin{bmatrix} A_x & A_y & A_z \end{bmatrix} \cdot \mathcal{E}, \tag{3.17}$$

where, $\mathcal{E}$ is defined as:

$$\mathcal{E} = \begin{bmatrix} p - 2\mu\frac{\partial u_x}{\partial x} & -\mu\left(\frac{\partial u_x}{\partial y} + \frac{\partial u_y}{\partial x}\right) & -\mu\left(\frac{\partial u_x}{\partial z} + \frac{\partial u_z}{\partial x}\right) \\ -\mu\left(\frac{\partial u_y}{\partial x} + \frac{\partial u_x}{\partial y}\right) & p - 2\mu\frac{\partial u_y}{\partial y} & -\mu\left(\frac{\partial u_y}{\partial z} + \frac{\partial u_z}{\partial y}\right) \\ -\mu\left(\frac{\partial u_z}{\partial x} + \frac{\partial u_x}{\partial z}\right) & -\mu\left(\frac{\partial u_z}{\partial y} + \frac{\partial u_y}{\partial z}\right) & p - 2\mu\frac{\partial u_z}{\partial z} \end{bmatrix}. \tag{3.18}$$

The accuracy of $\boldsymbol{F}$ improves with mesh refinement, as shown in Fig. 3.1. The Gerris fluid solver uses an adaptive mesh projection method proposed by Martin and Colella [68] and Howell and Bell [41]. Mesh adaption

is governed by a vorticity criterion, $\Delta x \left|\nabla \times \boldsymbol{u}\right| / \left|\boldsymbol{u}_{max}\right| > \zeta$, where ζ is mesh tolerance. A unique feature in GISS is that the computational domain is discretised by quad-tree (in 2D) or oct-tree (in 3D) cell (c.f. [47, 91]). This allows GISS to exploit the advantages from both conventional dynamic mesh adaptation and immersed solid methods. A cell in the mesh will be automatically adapted by dividing the root cell to 4 (in 2D) or 8 (in 3D) leaf cells under the criterion of vorticity, whilst all cells remain Cartesian. This "tree-structure adaptation" of the mesh is simpler than the commonly used body-conformal unstructured mesh adaption (Fig. 3.1).

For a mesh refinement level N, the smallest mesh size, $\Delta x_{MIN} = L/2^N$ surrounds the solid. In dimensionless terms, $\Delta x^*_{MIN} = \Delta x_{MIN}/D_p$. We define mesh resolution as inverse of mesh size i.e. $R_m = 1/\Delta x^*_{MIN} = D_p/\Delta x_{MIN}$. In order to ensure the continuity of numerical error between the fluid and the solid domains, $\Delta x^*_{MIN}|_f = \Delta x^*|_s$ where $\Delta x^*|_s$ is the the mesh defining the immersed solid. This also ensures enforcement of the no-slip, nopenetration boundary condition on the walls of the solid. This also minimises error in calculation of the stress tensor around the solid and hence the drag and lift forces. During the simulation, the timestep is set to fulfil both Courant and viscous criteria such that $\Delta t^* \leqq min\left(\frac{\Delta x_{MIN}}{U_0}\frac{U_0}{D}, \frac{\Delta x^2_{MIN}}{\nu}\frac{U_0}{D}\right) \implies \Delta t^* \leqq min\left(\frac{1}{M_R}, \frac{Re_p}{M_R^2}\right)$.

With the aforementioned description of the solid, we can then apply Gauss's theorem on Eq. 3.9 and rewrite it to its spatial discrete equivalent with consideration of the fluid fraction:

$$\iint_A \nabla p \cdot \boldsymbol{n} dA = \frac{\rho_f}{\Delta t} \iiint_V \nabla \cdot \mathbf{u}^\star dV, \tag{3.19}$$

$$\sum_d s_d \nabla_d p = \frac{\rho_f h c}{\Delta t} \nabla \cdot \mathbf{u}^\star. \tag{3.20}$$

Here, h is the local mesh size. Eq. 3.20 is a general form of the Poisson equations solved by Gerris [86].

We now perform some basic validation studies for the immersed solid solver, for cases of solid translation and rotation in viscous fluid, against theory and against experiments reported in literature.

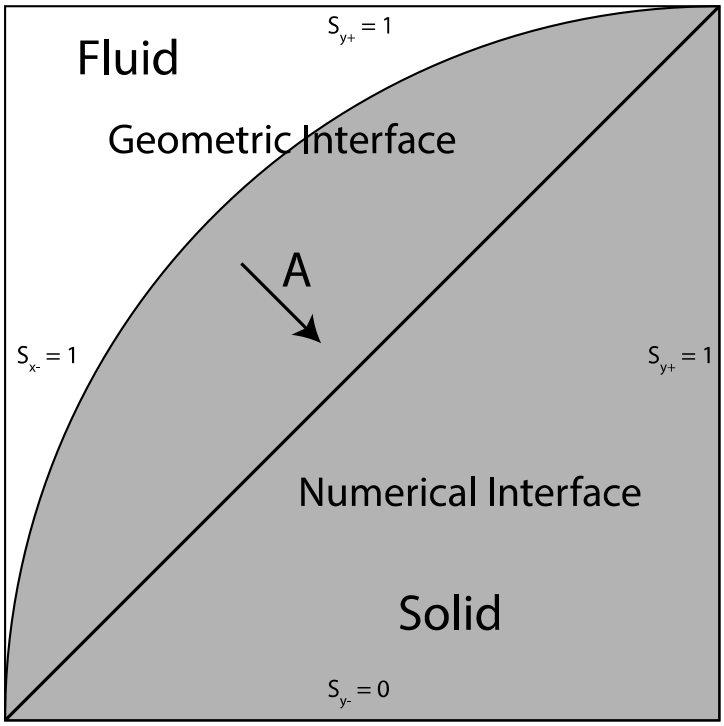

(a) Coarse parental mesh

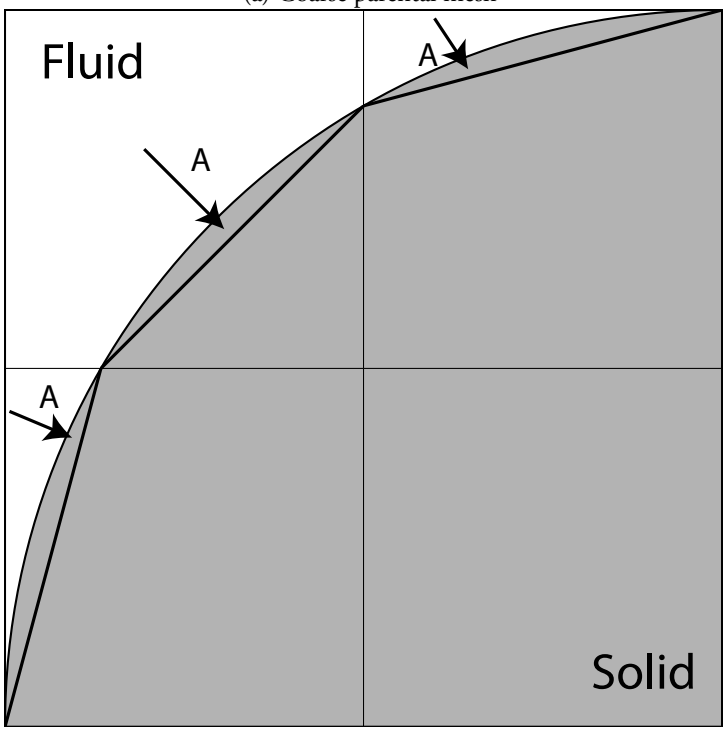

(b) Under mesh refinement.

Figure 3.1: Calculating numerical surface using volume of fluid approach and mesh refinement at fluid-interface elements

Time	Typical Dynamic Mesh Adaption	Typical Immersed Boundary Method	Quadtree Mesh in GISS
At $t = 0$	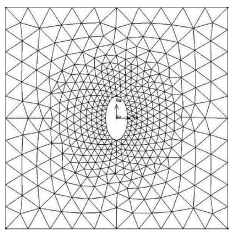	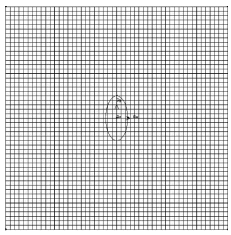	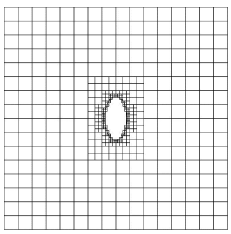
At $t > 0$	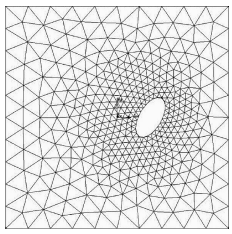	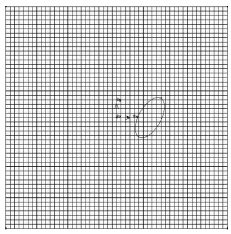	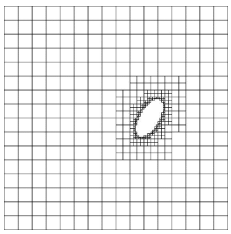

Table 3.1: Mesh adaption methods

3.1.3 *Validating GISS for Simple Solid Motion at Finite Reynolds Number*

3.1.3.1 *Translational Motion during Settling*

The initial transient and the terminal velocity of a sphere settling in a fluid was validated against the experiments of Mordant and Pinton [76] where beads were gently released in water, and against the theoretical calculations of Clift, Grace and Weber [12]. The experiments were simulated using a domain spacious sufficient, see Fig. 3.2a, to eliminate the effect of the side boundaries ($L/D_p = 32$). Our previous rigorous studies [94] suggested that a sixteen fold mesh refinement, defined as $R_m = 1/16$ was dense enough around the body to accurately simulate settling.

While we have simulated all experimental cases of Mordant and Pinton [76] in the range $41 \leq Re_p \leq 430$, we present one of them in Fig. 3.2b. It can be seen that the 3D GISS solver shows good agreement with both the theoretical predictions and experiments.

3.1.3.2 *Rotational Motion describing Jeffery's Orbits*

Here we seek to simulate the rotational motion of an ellipsoid immersed in a fluid of the same density as itself, under simple shear flow, and to validate it against the classical Jeffery's orbit solution [50]. Our set-up contains such an an ellipsoid of revolution subjected to a Couette flow at a constant

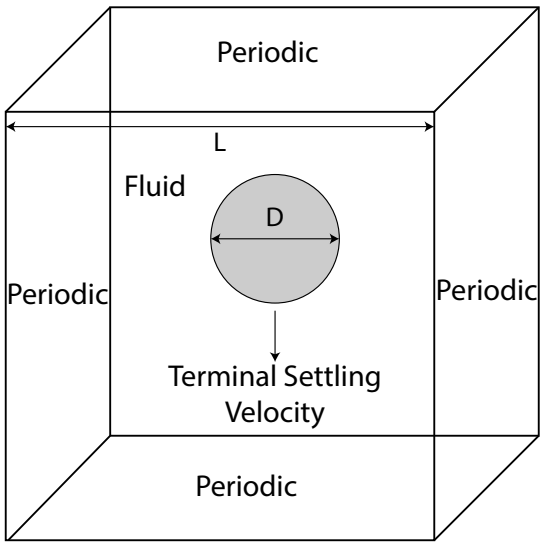

(a) Problem definition

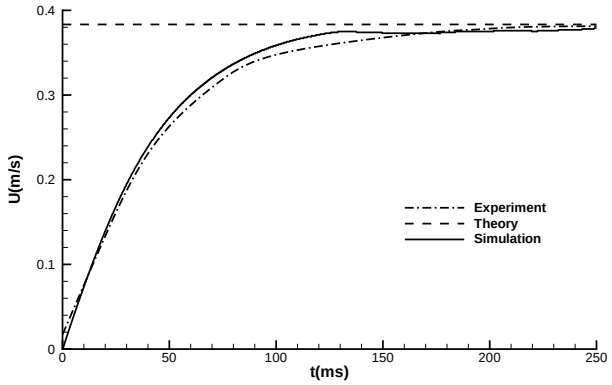

(b) $Re_p = 430$, steel sphere case of Mordant and Pinton [76]

Figure 3.2: Settling of a steel sphere at $Re_p = DU_0/\nu = 430$ against experiments of Mordant and Pinton [76]. Sample of results from Shui et al. [94].

shear rate (ξ) in a channel. The channel is bounded by walls at the top and bottom, both moving with constant velocity but in opposite directions. The boundaries in the stream-wise and span-wise directions are periodic, as shown in Fig. 3.3a. The rotation of the solid is then compared against the theoretical result of Jeffery [50].

Fig. 3.3b shows the detailed process of the rotation of prolate spheroids with different ε, where ε is the aspect ratio defined as, $\varepsilon = a/b$. We may conclude that our simulated rotation at various aspect ratios is in very good agreement with theory (both spatially and temporally). The angle and time were non-dimensionalized by their values for one cycle. Thereby proving the ability of GISS to predict solid body rotation using the full Navier-Stokes equations at low Re_p. Note that only a small sample of results from an exhaustive validation study available in Shui et al. [94] have been presented here.

Good agreements between the DNS and theory/ experiments, in the classical settling and rotation problems described in Sections 3.1.3.1 and 3.1.3.2 respectively, give us confidence in the ability of the GISS solver to tackle simple solid motion in viscous fluid. We now consider the more difficult case of an immersed solid in inviscid fluid presenting complex 6DoF motion.

3.2 DYNAMICS OF A BODY IMMERSED IN AN INVISCID FLUID

We now target the classical problem of motion of a general ellipsoid immersed in a fluid. This is a particularly important problem given that the solid depicts a complex 6DoF motion. Under inviscid conditions the dynamics are described by the Kirchhoff-Clebsch equations. These equations, and our solutions to them for triaxial ellipsoids, are discussed below.

3.2.1 *Kirchhoff-Clebsch Equations and Solution Methodology*

Provided that the ellipsoid is completely submerged by fluid which is inviscid, irrotational, incompressible, and stationary at infinity, the fluid-solid system may be studied as a whole as follows, offering considerable simpli-

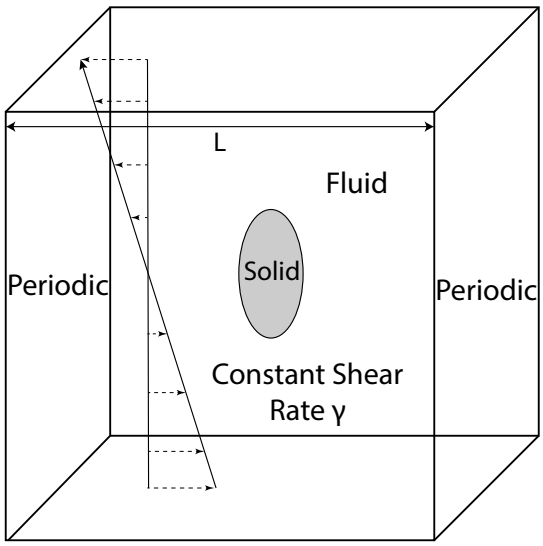

(a) Classical Jeffery's orbits problem schematic

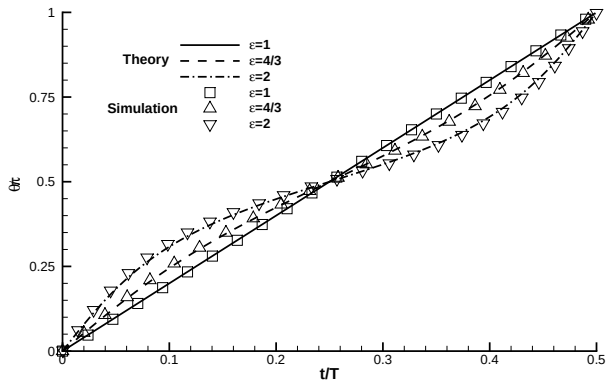

(b) Rotation curves at various aspect ratios, $Re_p = 0.1$, $M = 16$, $L^* = 4$.

Figure 3.3: Rotation of a neutrally buoyant prolate spheroid, of aspect ratio $\varepsilon = a/b$ as stated in the legend, under shear flow defined by $Re_p = 4\xi a^2/\nu$ against the theory of Jeffery [50]. Sample of results from Shui et al. [94].

fication. The total kinetic energy K_{tot} for the combined fluid-solid system may be written as

$$K_{tot} = \frac{1}{2}\boldsymbol{v} \cdot \mathcal{M}\boldsymbol{v} + \frac{1}{2}\boldsymbol{\Omega} \cdot \mathcal{J}\boldsymbol{\Omega}, \tag{3.21}$$

where

$$\mathcal{M} \equiv \mathcal{M}_f + \mathcal{M}_s, \qquad \mathcal{J} \equiv \mathcal{I}_f + \mathcal{I}_s, \qquad \text{and } \mathcal{A} = \begin{bmatrix} \mathcal{M}_f & \mathcal{S} \\ \mathcal{S}^T & \mathcal{I}_f \end{bmatrix}. \tag{3.22}$$

$\mathcal{A}$ is the added mass tensor of the fluid, which includes both linear and rotational effects, and is dependent on the body shape and the fluid density. For any body which is symmetric about three mutually perpendicular axes, we have a desirable simplification, in that $\mathcal{S} = 0$, and further, for a triaxial ellipsoid, $\mathcal{M}_f$ and $\mathcal{I}_f$ are given in closed form ([Lamb [63], see also Korotkin [55]]) by

$$\mathcal{M}_f = V_s \rho_f \begin{bmatrix} \frac{\alpha}{2-\alpha} & 0 & 0 \\ 0 & \frac{\beta}{2-\beta} & 0 \\ 0 & 0 & \frac{\gamma}{2-\gamma} \end{bmatrix}, \tag{3.23}$$

$$\mathcal{I}_f = \frac{V_s \rho_f}{5} \begin{bmatrix} \frac{(b^2-c^2)^2(\gamma-\beta)}{2(b^2-c^2)+(\beta-\gamma)(b^2+c^2)} & 0 & 0 \\ 0 & \frac{(a^2-c^2)^2(\gamma-\alpha)}{2(a^2-c^2)+(\alpha-\gamma)(a^2+c^2)} & 0 \\ 0 & 0 & \frac{(a^2-b^2)^2(\beta-\alpha)}{2(a^2-b^2)+(\alpha-\beta)(a^2+b^2)} \end{bmatrix}. \tag{3.24}$$

In these expressions,

$$\alpha = abc \int_0^\infty \frac{d\lambda}{(a^2+\lambda)k_\lambda}, \quad \beta = abc \int_0^\infty \frac{d\lambda}{(b^2+\lambda)k_\lambda}, \quad \gamma = abc \int_0^\infty \frac{d\lambda}{(c^2+\lambda)k_\lambda}, \tag{3.25}$$

$$\text{where } k_\lambda^2 = (a^2+\lambda)(b^2+\lambda)(c^2+\lambda). \tag{3.26}$$

The added mass terms are obtained by fourth-order Runge-Kutta integration of Eq.(3.25). λ is one of the components of the Ellipsoidal coordinate system (λ, μ, ν) that generalizes the two-dimensional elliptic coordinate system.

In terms of the generalised momentum $\boldsymbol{P} = (\mathcal{M}_f + \mathcal{M}_s)\boldsymbol{v}$ and the generalised angular momentum $L = (\mathcal{I}_f + \mathcal{I}_s)\boldsymbol{\Omega}$ the Kirchhoff-Clebsch equations take the form [3]

$$\dot{\boldsymbol{P}} + \boldsymbol{\Omega} \times \boldsymbol{P} = 0, \qquad \dot{\boldsymbol{L}} + \boldsymbol{\Omega} \times \boldsymbol{L} + \boldsymbol{v} \times \boldsymbol{P} = 0. \tag{3.27}$$

Our coordinate frame moves and is oriented with the body, so $\boldsymbol{v}$ and $\boldsymbol{\Omega}$ are the instantaneous velocity and angular velocity of this frame. This is a Hamiltonian system [3], where K_{tot} is the Hamiltonian. There are two other integrals of the motion apart from K_{tot}, namely $\boldsymbol{P} \cdot \boldsymbol{P}$ and $\boldsymbol{L} \cdot \boldsymbol{P}$. Solutions for the ordinary differential equations (3.27) are obtained by a Runge-Kutta fourth-order scheme, and it is ensured that the three integrals of motion are maintained constant throughout the solution to at least six significant decimal places. The results of Aref and Jones [3] were recovered excellently (not shown). It has been recently shown that is possible to extent the notion of added mass from the ideal fluid regime to more general viscous flows, [67].

3.2.2 *Derivation of the added-mass tensor*

In our analysis far, we have assumed that the fluid the body is immersed within, is infinite in extent and is an ideal fluid. If we impose a further condition on the fluid, namely that it is free from vortices, it becomes possible to derive the added-mass tensor, we will be following the method presented by Milne-Thomson [73]. The irrotational condition implies the existence of a single-valued scalar potential field, ϕ, such that the fluid velocity can be given by:

$$\boldsymbol{u} = \nabla\phi, \tag{3.28}$$

The incompressible nature of the fluid and the conversation of mass imply that the potential field must satisfy the Laplace equation.

$$\nabla^2\phi = 0. \tag{3.29}$$

The following boundary conditions apply to Eq. 3.29 in this situation:

1. Impermeability condition of the body, valid on its surface, S:

$$\left.\frac{\partial\phi}{\partial\boldsymbol{n}}\right|_S = \boldsymbol{v_n}, \tag{3.30}$$

   where $\left.\frac{\partial\phi}{\partial\boldsymbol{n}}\right|_S$ is a projection of the fluid velocity on the normal unit vector of the surface S and $\boldsymbol{v_n}$ is the projection of the velocity of a point on the body along the normal $\boldsymbol{n}$

2. Stationary condition at infinity:

$$\lim_{\boldsymbol{x}\to\infty} \nabla\phi = 0. \tag{3.31}$$

The potential field ϕ depends on time via the right-hand side of the boundary Eq. 3.30. Looking at this condition is more detail; we find that the velocity of an arbitrary point on the body, $\boldsymbol{v_r}$, is giving by the following:

$$\boldsymbol{v_r} = \boldsymbol{v} + \boldsymbol{\Omega} \times \boldsymbol{r}. \tag{3.32}$$

Substituting Eq. 3.32 into the surface boundary condition Eq. 3.30, we can obtain the following expressions:

$$-\left.\frac{\partial\phi}{\partial\boldsymbol{n}}\right|_S = \boldsymbol{n}\cdot\boldsymbol{v_r}, \tag{3.33}$$

$$= \boldsymbol{n}\cdot(\boldsymbol{v} + \boldsymbol{\Omega}\times\boldsymbol{r}), \tag{3.34}$$

$$= \boldsymbol{v}\cdot\boldsymbol{n} + \boldsymbol{\Omega}\cdot(\boldsymbol{r}\times\boldsymbol{n}). \tag{3.35}$$

This condition can be satisfied by the following:

$$\phi = \boldsymbol{v} \cdot \boldsymbol{\psi} + \boldsymbol{\Omega} \cdot \boldsymbol{\chi}. \tag{3.36}$$

Where $\boldsymbol{\psi}$ and $\boldsymbol{\chi}$ are vectors whose components are solutions to the Laplace equation that satisfy the following boundary conditions:

$$\lim_{\boldsymbol{x}\to\infty} \nabla\psi_i = 0, \tag{3.37}$$

$$\lim_{\boldsymbol{x}\to\infty} \nabla\chi_i = 0, \tag{3.38}$$

$$-\left.\frac{\partial \boldsymbol{\psi}}{\partial \boldsymbol{n}}\right|_S = \boldsymbol{n}, \tag{3.39}$$

$$-\left.\frac{\partial \boldsymbol{\chi}}{\partial \boldsymbol{n}}\right|_S = \boldsymbol{r} \times \boldsymbol{n}. \tag{3.40}$$

$\boldsymbol{\psi}$ and $\boldsymbol{\chi}$ are independent of the motion of the body the fluid and are only dependent on its geometry. It was noted by [63], that by using the linearity of the problem would allow us to represent the potential ϕ as a sum.

$$\phi = \sum_{i=1}^{6} \dot{\sigma}_i \phi_i. \tag{3.41}$$

Where $\dot{\sigma}_i$ are the generalised velocities of the system and ϕ_i are the flow potentials corresponding to the body moving along the generalised coordinates relating to those velocities. Now that we have a method to calculate, ϕ, it is possible to calculate the kinetic energy of the fluid, K_f.

$$K_f = \frac{1}{2}\rho_F \iiint_V \boldsymbol{u} \cdot \boldsymbol{u} dV, \tag{3.42}$$

$$= \frac{1}{2}\rho_F \iiint_V \|\nabla\phi\|^2 \, dV. \tag{3.43}$$

Using the Green's transformation, we can write the expression:

$$K_f = -\frac{1}{2}\rho_F \iint_S \phi \frac{\partial \phi}{\partial \boldsymbol{n}} dS, \tag{3.44}$$

Substituting Eq. 3.41 into Eq. 3.44, we obtain the following:

$$K_f = \frac{1}{2}\sum_{i=1}^{6}\sum_{j=1}^{6}\mathcal{A}_{ij}\dot{\sigma}_i\dot{\sigma}_j. \tag{3.45}$$

where $\mathcal{A}_{ij}$ are the added masses, with the values:

$$\mathcal{A}_{ij} = -\rho\iint_S \phi_j \frac{\partial\phi_i}{\partial \boldsymbol{n}} dS. \tag{3.46}$$

The added-masses are independent of the kinematics of the body's motion since Eq. 3.46 does not contain any generalised velocities. They only depend on the geometry of the body, the chosen coordinate system and the density of the fluid. For our case of an ellipsoid it is possible to calculate the values of $\mathcal{A}_{ij}$ analytical and are well known in the literature, [73] and [55].

3.2.3 *Symmetry and the limits of integrability*

Kozlov and Onishchenko [57] proved that chaotic motion can exist when the ellipsoid's geometry satisfies the following condition:

$$j_a^{-1}(m_b - m_c) + j_b^{-1}(m_c - m_a) + j_c^{-1}(m_a - m_b) \neq 0, \tag{3.47}$$

where $m_{a,b,c}$ and $j_{a,b,c}$ are the elements of the diagonal matrices $\mathcal{M}$ and $\mathcal{J}$ along the a, b and c semi-axes of the ellipsoid. In the general case of a triaxial ellipsoid, which we define as one where $a \neq b \neq c$, only in very special ratios of these axes can the condition 3.47 be violated. So for almost any triaxial ellipsoid, the dynamics is non-integrable, and we should be able to obtain chaotic trajectories. Aref and Jones [3] identified that the dynamics of an ellipsoid with semiaxes in the ratio 1.0, 0.8 and 0.6 is non-integrable by the Kozlov-Onishchenko theorem and demonstrated chaotic trajectories. If the ellipsoid has an axis of rotation, i.e., if two of the axes, say b and c are equal, then $j_b = j_c$ and $m_b = m_c$, the above inequality is never satisfied, i.e., the dynamics is integrable. Several authors, such as Holmes, Jenkins and Leonard [39] and Dragović and Gajić [22] have identified this property. Such ellipsoids are referred to as ellipsoids of revolution, or as prolate spheroids where $a > b$ and oblate spheroids

where $a < b$. The system must exhibit periodic or quasiperiodic behavior in this case. Such a body of revolution is analogous to the Lagrange case of the heavy top found in Goldstein, Safko and Poole [37].

Put differently, given that Eq. 3.27 represents a six degree of freedom system, and three integrals of the motion have been identified. Using the degeneracy properties of the relevant Poisson bracket, Kozlov-Onishchenko were able to show, for a general ellipsoid, that if one more integral of the motion is supported, the system is completely integrable. For a sphere, $\alpha = \beta = \gamma = 1/2$, so we recover its well known added mass. Moreover $\mathcal{I}_f$ in this case is just 0, so a sphere will not be rotated by an inviscid fluid. We thus have $\dot{\boldsymbol{L}} = 0$, with which the conditions for integrability are trivially satisfied. For a spheroid, we explicitly identify another integral of the motion below, and show physically how it considerably simplifies the dynamics.

3.3 CONCLUSIONS

In this chapter, both the DNS methodology used in our in-house 6DoF GIS solver and the theoretical framework for solving the Kirchoff-Clebsch equations are presented in detail. It must be noted that while the GIS Solver can be used for both inviscid and viscous systems, the Kirchoff-Clebsch equations are solved for inviscid systems. As will be seen in Chapter 4, the Kirchoff-Clebsch equations have two main purposes: a) to validate our DNS results using the inviscid Euler equations and b) to explore a wide parameter space of energy and density ratios. In Chapter 5, the DNS methodology is further extended to understand to the role of tumbling ellipsoids in mixing. Chapter 6 further expands the theoretical framework to account for the presence of multiple bodies.

4

ORBITS OF TUMBLING ELLIPSOIDS

This chapter demonstrates the use of DNS and the Kirchoff-Clebsch methodologies described in Chapter 3 to quantify the orbits tracked by an ellipsoid in inviscid and viscous fluid. The problem is particularly challenging as Kozlov and Onishchenko [57] have shown that in some situations, the orbits could be chaotic. Contents of this chapter have been submitted as an article for The Journal of Fluid Mechanics, which is under peer-review.

In an inviscid fluid, when the axes of a triaxial ellipsoid are fixed, two parameters characterise the system: the ratio of the densities of fluid and solid, and the total kinetic energy of the fluid-solid system. Our first objective in this chapter is to show how these parameters affect the dynamics. We also pose the same question on the behaviour of a body immersed in a fluid at high particle Reynolds number, where the effects of viscosity are non-negligible. We show that chaotic dynamics is displayed here as well by a triaxial ellipsoid. Moreover, ellipsoids of rotation, with two of the axes equal, whose dynamics are integrable under inviscid conditions, are shown to display chaotic dynamics at high Reynolds number.

4.1 PROBLEM STATEMENT

Consider a solid shaped as a general ellipsoid of axes a, b and c, immersed in a cubical fluid domain of size $L \gg (a, b, c)$ as shown in figure 4.1. We define a density ratio $\rho = \rho_f/\rho_s$, where ρ_f and ρ_s are densities, and the subscripts s and f stand for solid and fluid respectively. The kinetic energy of the solid is given by

$$K_s = \frac{1}{2}\left[\boldsymbol{v} \cdot \mathcal{M}_s \boldsymbol{v} + \boldsymbol{\Omega} \cdot \mathcal{I}\boldsymbol{\Omega}\right]. \tag{4.1}$$

$\mathcal{M}_s$ is a diagonal 3×3 matrix whose non-zero elements are the mass m of the ellipsoid, while $\mathcal{I}$ is its moment of inertia tensor. $\boldsymbol{v}$ is the translational velocity vector of the solid, $\boldsymbol{\Omega}$ is its angular velocity vector. The fluid in the direct numerical simulations is initially at rest, so K_s comprises the

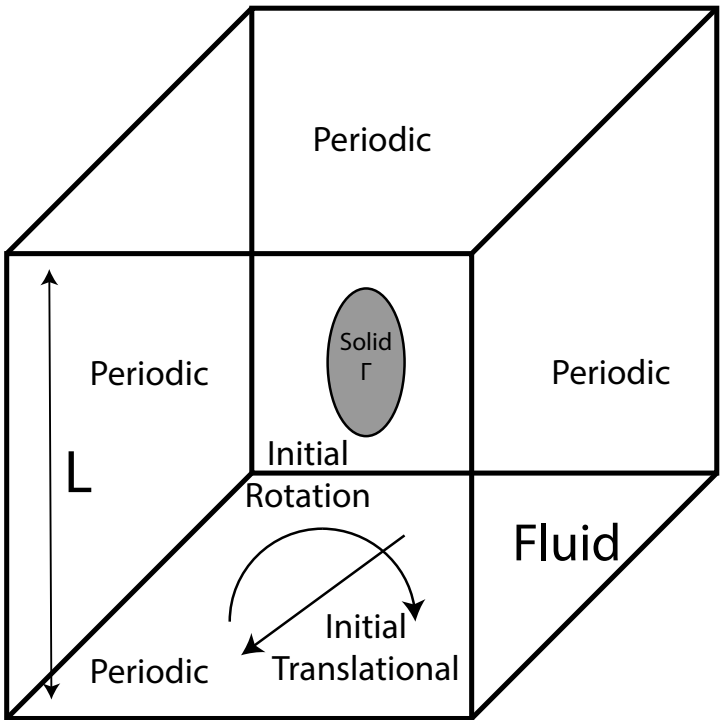

(a)

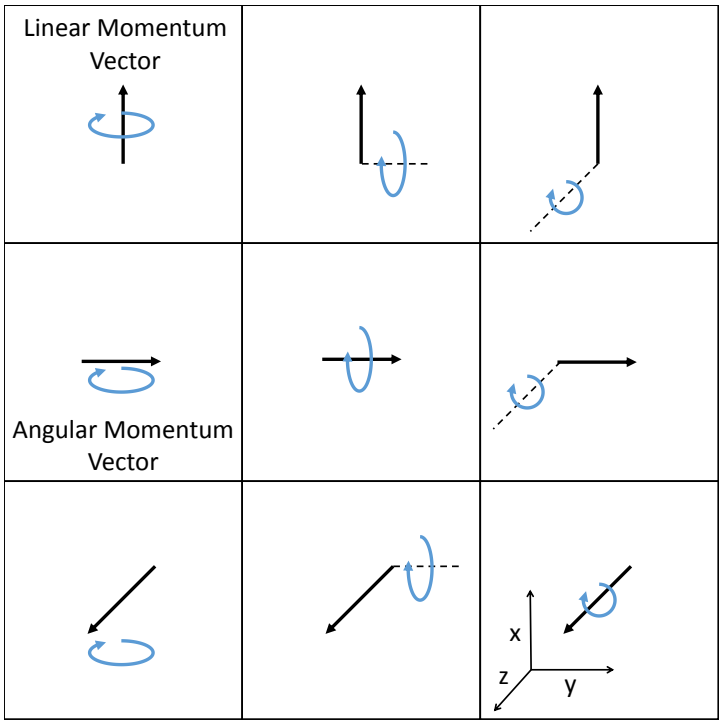

(b)

Figure 4.1: Problem definition (a) A general ellipsoid with aspect ratio $a : b : c$ immersed in a fluid with initial energy ratio E, and (b) schematic of nine initial conditions formed by basic configurations of the linear momentum and angular momentum vectors. The axes are defined as shown, in a frame of reference fixed with the body. A general initial condition can be constructed by a linear combination of these conditions.

total kinetic energy of the system. In an inviscid flow the kinetic energy is maintained constant through time, but gets interchanged between fluid and solid in interesting ways in a triaxial ellipsoid, as we shall see. Note that there is no gravity or any other bodyforce in this problem. This enables the kinetic energy to be treated as the Hamiltonian of the system.

We emphasise here the difference between a body held fixed, with a flow going past it, and one which is free to tumble and move. Auguste, Magnaudet and Fabre [4] have shown, for example, that the minimum Reynolds number for lateral motion in a freely falling thin disk is about a half the Reyolds at which a fixed disk would display wake instability. Although capable of far richer dynamic, there are far fewer studies on bodies free to move in fluids than those held fixed. It is hoped that the numerical method presented here will help to fill the gap, and enables viscous and inviscid studies on moving bodies. The code will soon be made publicly available. A triaxial ellipsoid held fixed in a steady incoming flow would never display the chaotic behaviour we are after.

In our direct numerical simulations, the solid is subjected to an initial condition with a specified ratio E of the initial translational kinetic energy, k_t to the the initial rotational kinetic energy k_r:

$$E = \frac{k_t}{k_r} = \frac{m \left\| \boldsymbol{v} \right\|^2}{\boldsymbol{\Omega} \cdot \mathcal{I}\boldsymbol{\Omega}}. \tag{4.2}$$

We found that the initial energy ratio E is an excellent choice for delineating the dynamics rather than the total kinetic energy, although the latter remains constant in an inviscid flow whereas the former does not. This is because the degree of chaos in the system depends on the ratio E, as we shall see. Higher energy ratios indicate the dominance of initial translational kinetic energy over rotational . It is important to note that a range of initial conditions can be imposed for the same E, some basis combinations are shown in Fig. 4.1b. We study immersed solids ranging from far heavier to much lighter than the fluid, and investigate their orbital behaviour under both inviscid and viscous conditions. In the viscous case, we define a particle Reynolds number, $Re_p = D_p U_0/\nu$, based on the solid length-scale D_p and the initial solid velocity, U_0. In our simulations, we have chosen D_p as the longest axis a of the ellipsoid. For solids immersed in inviscid fluids we cross-validate our DNS results against the-

oretical solutions of the Kirchhoff-Clebsch equations for inviscid fluids. Our DNS and theoretical methodologies are detailed in Section 3.1 and Section 3.2.1, respectively. Using DNS and solutions of the Kirchhoff-Clebsch equations, we then investigate the influence of density ratios and energy ratios on the trajectories executed by the ellipsoid. To study the effect of fluid viscosity we use DNS.

4.2 VALIDATING OUR NUMERICAL APPROACH IN INVISCID ENVIRONMENTS

The Kirchhoff-Clebsch system, being inviscid, and in addition offering a rich tapestry of complex behaviour, provides a rigorous benchmark test-case for validating any numerical approach. Our next objective is therefore to conduct an inviscid direct numerical simulation equivalent to solving Kirchhoff-Clebsch using GISS, and to test it against the Kozlov-Oniscenko theorem. The problem is set up as shown in Fig. 4.1a. The domain size is $L = 512a$ where $2a$ is the major axis of the ellipsoid. All sides of the domain are periodic. Such a large domain is chosen to ensure that the solid has enough space to track chaotic orbits without interference from residual wakes (in the viscous case) due to the periodic boundary conditions. The highest mesh resolution was set as 128 grid points on the solid surface, and adaptive mesh refinement ensures that the flow around it is adequately resolved. In the Direct Numerical Simulations the ellipsoid is given an initial velocity U_0 and angular velocity Ω_0 which are perpendicular to each other as used by Aref and Jones [3] and shown in some of the schematics in Fig. 4.1b. Note that the dot product of the momentum and angular momentum in this case is zero, and, since it is an integral of the motion, will remain zero throughout the simulation time. We recommend this, to reduce the time needed for the ellipsoid to explore a statistically significant region of the system's phase space, but any angle between the two may be used, and will not change the results qualitatively, as we have shown above. In our Kirchhoff-Clebsch solutions we have used a far wider range of initial conditions as will be discussed below. We wish to obtain

the trajectory executed by a marker point, M, located on the surface of the ellipsoid. The relative location of M is

$$\boldsymbol{r}_M = \boldsymbol{x}_M - \boldsymbol{x}_C, \tag{4.3}$$

where $\boldsymbol{x}_M$ is the positional vector of M in the global frame and $\boldsymbol{x}_C$ is the positional vector of the solid centre in the global frame. Hence, plotting $\boldsymbol{x}_C$ shows the trajectory of the solid centre moving in the fluid, and plotting $\mathbf{r_M}$ shows the orbit of the marker point relative to the solid centre itself, representing the orientation of the solid. These vectors as solutions of the equations give an immediate view of how the orientation and position of the ellipsoid changes as it moves through the fluid.

4.2.1 *Periodic and Quasiperiodic Dynamics*

We consider the case of an ellipsoid of revolution, $a : b : c = 1 : 0.7 : 0.7$. The initial energy ratio is specified as $E = 1$. Fig. 4.2a shows an orbit described by the marker point, $\boldsymbol{r}_M$, about the centre of mass of the ellipsoid using GISS simulations. Is is seen that $\boldsymbol{r}_M$ describes a near-circular orbit in the $x - y$ plane. Every time the orbit is described, the location on the z axis is slightly different, and we cannot yet distinguish whether this is due to numerical errors or due to the quasiperiodic nature of the orbit. We shall return to this point below. It is obvious however, that the dynamics is not chaotic. This conclusion agrees well with our own solution of the Kirchhoff-Clebsch equations, example shown in Fig. 4.2b. The initial conditions are different in the two cases, but the dynamics is similar.

4.2.2 *Chaotic Dynamics*

We next study the dynamics of a triaxial ellipsoid, with $a : b : c = 1 : 0.8 : 0.6$. This was the shape studied by Aref and Jones [3] whose sample result indicated that increasing the ratio ρ of fluid density to solid density increases the propensity for chaotic orbits.

The initial condition is quantified at $E = 20$. Fig. 4.3a shows clearly that the orbit tracked by the marker point using GISS simulations is chaotic. This also agrees well with our own solution of the Kirchhoff-

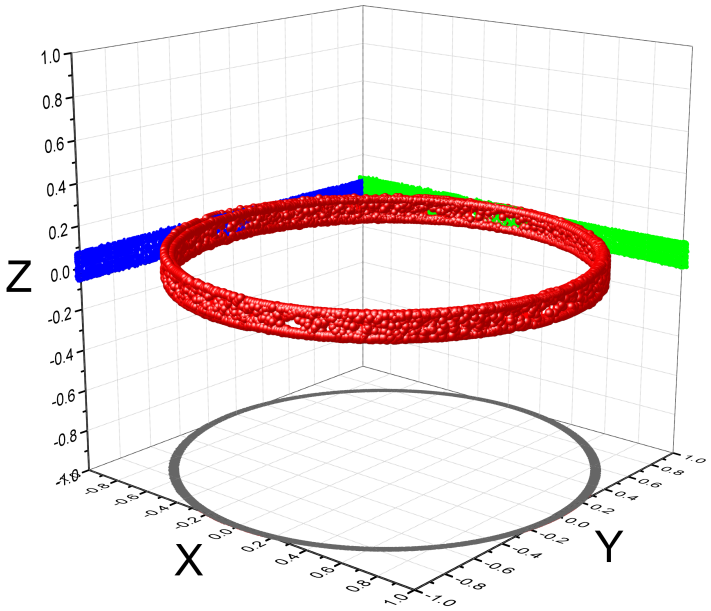

(a) DNS solution

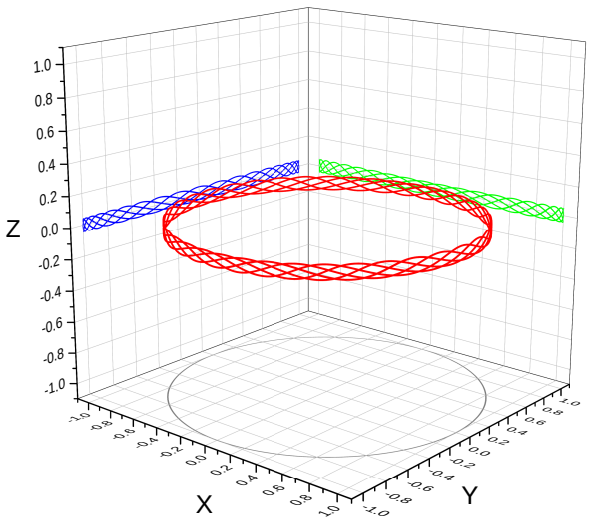

(b) Kirchhoff-Clebsch solution

Figure 4.2: Periodic orbits tracked by a marker point M on an ellipsoid of revolution with $a : b : c = 1 : 0.7 : 0.7$ at $E = 1$ and $\rho = 1$. The orbit (locus of points defined by $\boldsymbol{r}_M$) is represented in red, with its projections on the XY, XZ and YZ planes in grey, blue and green, respectively.

Clebsch equations, as shown in Fig. 4.3b. Apart from the marker point it is instructive to obtain the trajectories tracked by the centroids $\boldsymbol{x}_C$ of the periodic and chaotic ellipsoids in DNS. These are shown in Fig. 4.4b. After an initial transient during which the fluid gains kinetic energy the centroid of the ellipsoid of rotation settles into motion on a line, and we have seen earlier that it is in steady rotation about its centroid. The triaxial ellipsoid on the other hand executes irregular motion.

We have thus shown that our numerical approach, which was tested earlier in viscous environments, not only works well in invisdic environments, but is able to demonstrate the Kozlov-Onishchenko theorem by showing chaotic trajectories in the case of a triaxial ellipsoid, which reduce to simple dynamics for an ellipsoid of revolution. We next present a method to quantify orbital behaviour.

4.3 UNDERSTANDING ORBITAL BEHAVIOUR

We use recurrence quantification analysis (RQA) to quantify orbits tracked by solid bodies. A recurrence plot (RP) is the foundation of RQA. Eckmann, Oliffson Kamphorst and Ruelle [28] introduced recurrence plots, as a way to visualise the dynamics of a system through its phase space, marking all time points when a said event recurs. The main advantage of recurrence plots is that they provide a means to investigate behaviour of N-dimensional dynamics using a two-dimensional plot. Recurrence is defined by Eq. 4.4.

$$R(i,j) = \begin{cases} 1 & \text{if } \| \boldsymbol{x}_M(i) - \boldsymbol{x}_M(j) \|_\infty \leq \epsilon \\ 0 & \text{otherwise,} \end{cases} \tag{4.4}$$

where $R(i,j)$ is an N-by-N matrix, N being the number of samples in the time series, $\boldsymbol{x}_M(i)$ is the position of the marker point M in the phase space of the body at time i and $\boldsymbol{x}_M(j)$ is the position of the marker point in the phase space of the body at time j. A thought experiment will tell us that a perfectly periodic system will only have solid diagonal lines in the recurrence plot, and the spacing of the diagonal lines will be periodic. A quasiperiodic system will have only diagonal lines, but these could be broken into segments. Deterministic chaos of a small number of degrees

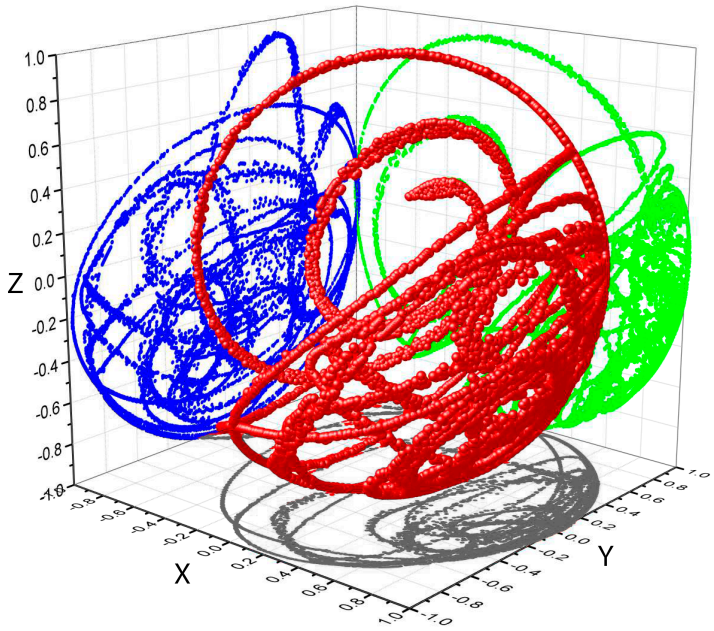

(a) DNS Solution

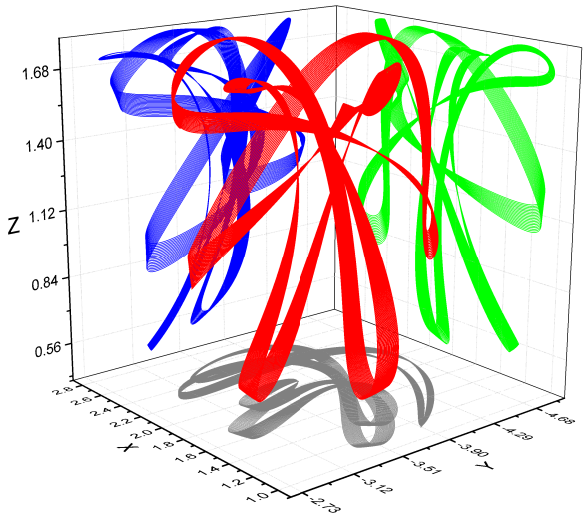

(b) Kirchhoff-Clebsch Solution

Figure 4.3: Chaotic orbits tracked by a marker point M on a triaxial ellipsoid $a : b : c = 1 : 0.8 : 0.6$ at $E = 20$ and $\rho = 1$.

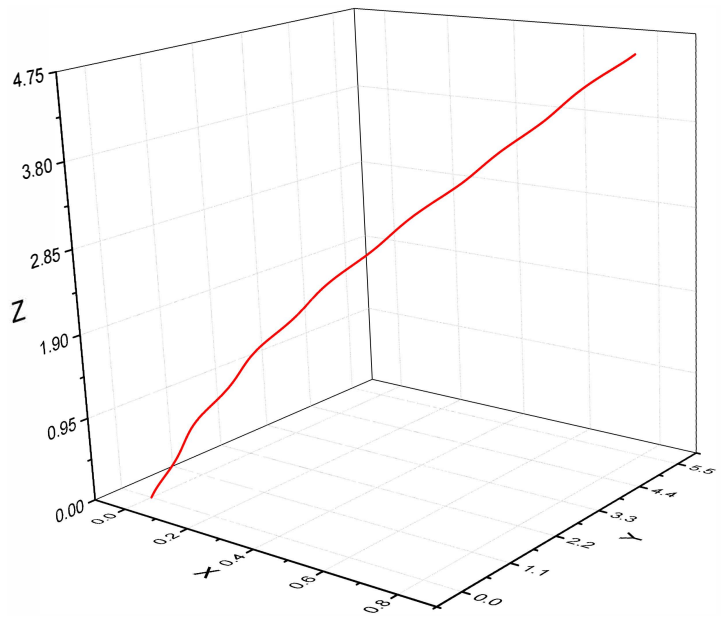

(a) Periodic system

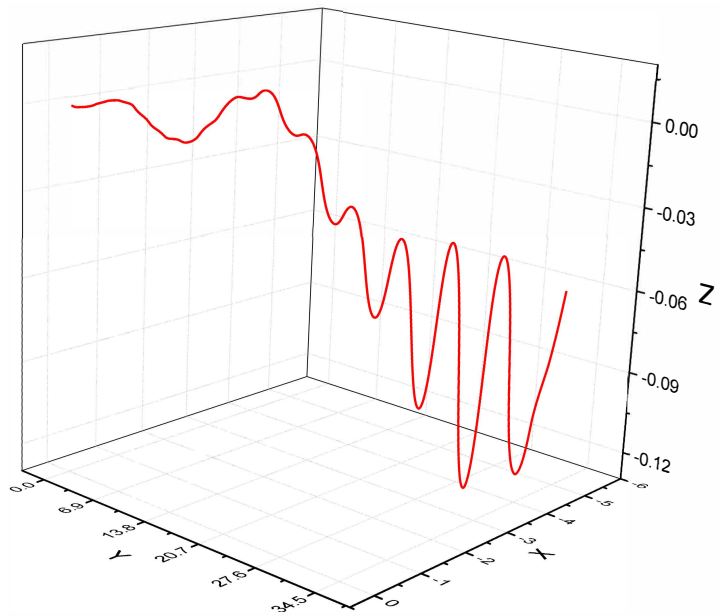

(b) Chaotic system

Figure 4.4: Trajectories of the centroids of the ellipsoids (locus of points defined by $\boldsymbol{x}_C$) for (a) the simulation of the ellipsoid of revolution shown in Fig. 4.2a and (b) that of the triaxial ellipsoid of Fig. 4.3a. These are results from DNS.

of freedom presents visually interesting patterns in the recurrence plot. On the other hand, white noise would display a recurrence plot composed of randomly spaced single dots. At a given time j, our RQA steps through the array i to check for recurrence of the position of the marker point for each timestep. In the case of our solution of the Kirchhoff-Clebsch equations, we use about 100000 timesteps and in our DNS it is about 200000 timesteps, with each timestep recording the spatial location of the marker point. Since perfect recurrence is nearly impossible due to numerical noise, ϵ is the heuristic threshold distance which determines where two given states are sufficiently close to count as a recurrence. In this work, we set $\epsilon = 5\%$ of the maximum phase-space diameter i.e., the maximum displacement presented by the solid in any simulation, in line with the recommendations of Marwan [69]. We make use of three statistical measures to quantify chaos, as defined below.

We define RR as the recurrence rate of the system, representing the probability of the solid's orientation to recur in the orbit.

$$RR = \frac{1}{N^2} \sum_{i,j=1}^{N} R(i,j), \tag{4.5}$$

We next define DET as the determinism exhibited by the system, which is a measure of the predictability of any dynamical system, as follows:

$$DET = \frac{\sum_{\ell=\ell_{min}}^{N} \ell P(\ell)}{\sum_{i,j=1}^{N} R(i,j)}, \tag{4.6}$$

where $P(\ell)$ is the frequency distribution of the lengths of the diagonal lines in a recurrence plot, ℓ is the length of those lines and ℓ_{min} is the criterion used to indicate the presence of a line. This is set to 2 in our work, which means that a minimum of 2 points (pixels) are needed to lay diagonally next to each other. We also define

$$p(\ell) = \frac{P(\ell)}{\sum_{\ell=\ell_{min}}^{N} P(\ell)}, \tag{4.7}$$

as the probability of a diagonal line giving exactly length ℓ. The Shannon entropy (ENTR) of the recurrence plot, given by

$$ENTR = -\sum_{\ell=\ell_{min}}^{N} p(\ell)\ln(p(\ell)), \tag{4.8}$$

can be calculated by this distribution. The entropy corresponds to the complexity of the deterministic structure in the system [70].

These statistics can be made time-dependent through computing over small time windows. These windows can be moved over the recurrence plot along the line of identity. These time-dependent measures can be useful to detect periodic-chaos regime transitions [69]. We define a moving time window, t_w over simulation time. Thus the number of simulation timesteps within the prescribed window is

$$N_w = \frac{t_w}{\Delta t}, \tag{4.9}$$

where Δt is the simulation timestep size. Using such a moving window, we can then compute the RQA statistics at any time t, corresponding to a timestep $n = t/\Delta t$ as below:

$$RR(t) = \frac{1}{{N_w}^2}\sum_{i,j=n}^{N_w} R(i,j), \qquad DET(t) = \frac{\sum_{\ell=\ell_{min}}^{N_w} \ell P_{t,t_w}(\ell)}{\sum_{i,j=n}^{N_w} R(i,j)}, \tag{4.10}$$

$$p_t(\ell) = \frac{P_{t,t_w}(\ell)}{\sum_{\ell=\ell_{min}}^{N_w} P_{t,t_w}(\ell)}, \qquad ENTR(t) = -\sum_{\ell=\ell_{min}}^{N_w} p_t(\ell)\ln(p_t(\ell)). \tag{4.11}$$

Here, $P_{t,t_w}(\ell)$ is the instantaneous frequency distribution of the lengths of the diagonal lines in a recurrence plot with respect to a window size of t_w, and $p_t(\ell)$ is the instantaneous probability of a diagonal line giving exactly length ℓ calculated over a moving time window t_w. In order to quantify which case is chaotic, DET is a very useful metric, [28]. As can be seen in Eq. 4.6, it is a measure of the fraction of points in the recurrence plot that form diagonal lines. A purely stochastic system would have a recurrent plot comprising scattered points, whereas a periodic or quasiperiodic system shows long running diagonal lines [69].

We identify orbital behaviour based on the recurrence plots and time dependent RQA statistics. Since periodic and quasiperiodic behaviour will consist only of diagonal lines or line segments, if we choose an N_w long enough to cover an orbital time, RR will remain constant, and DET will stay at a value of 1. On the other hand RR will not be constant, and DET must be less than 1 in a chaotic system. Similarly, the entropy remains constant in a periodic or quasiperiodic system but varies with time in a chaotic system.

We identify three classes of orbital behaviour based on the recurrence plots and time dependent RQA statistics.

- Periodic behaviour: The Time-Dependent Determinism, DET, of the system remains constant at a value of one and the entropy of the time series tends to remain constant.
- Quasiperiodic behaviour: After an initial decay, DET of the system remains constant and so does the entropy of the time series.
- Chaotic behaviour: The DET determinism tends to decay over time and the entropy of the series varies over time.

The analysis of small-scale features in these statistics can reveal more information about the behaviour of the system. For example, the recurrence rate, RR, and DET exhibit maxima at the periodic-chaotic transition. [70].

Fig. 4.5 shows recurrence plots corresponding to the nonchaotic orbital behaviour corresponding to the parameters used in in Fig. 4.2, and chaotic orbital behaviour of the case in Fig. 4.3. In Fig. 4.5a, the fact that the diagonal lines are often broken is indicative of quasiperiodic rather than strictly periodic motion of the marker point, similar patterns for quasiperiodic systems has been studied by Marwan et al. [70] . Whereas, in the case of chaotic orbital motion, Fig. 4.5b demonstrates a complex structure indicating irregular and unpredictable recurrence. At first sight the recurrence rate pattern seems to repeat itself in a regular manner. We recall that the high departure from a diagonal structure is already indicative of strongly chaotic dynamics. But we further ensured that there is no periodic pattern in the recurrence rate plot as well, by generating a residual recurrence plot by taking the difference between the original recurrence time-series and a time-shifted copy. The time shift was selected to minimises the error

between the two series, and it was obvious that there was no overlap (not shown).

Fig. 4.6 shows the behaviour of key statistical parameters, RR, DET, $ENTR$, over the period of the simulations to quantify orbital behaviour. For a periodic system, as shown in Fig. 4.6a, these statistics remain largely constant, and the DET is 1 (or, $1 - DET = 0$). Whereas, Fig. 4.6b demonstrates that in a chaotic system none of these parameters remain constant, and DET is less than 1. These statistics along with the texture of the recurrence plot are used to classify the behaviour of the orbits generated later in this chapter. We will also use Poincare sections to distinguish chaotic from non-chaotic behaviour.

4.4 DYNAMICS IN AN INVISCID ENVIRONMENT

There are four non-dimensional parameters in the inviscid problem: the axis ratios b/a and c/a, the fluid to solid density ratio ρ, and the ratio E of the initial kinetic energy of the system in rotational motion to that in linear motion of the body centroid.

To address the effect of the axis ratios first we ask what is it about a triaxial ellipsoid that makes it possible to see chaos in its dynamics and not in a spheroid. We answer that the added mass enables it. The primary difference between a spheroid and a triaxial ellipsoid is in the added complexity of the added mass tensor of the latter. In the case of a spheroid, two entries each of $\mathcal{M}$ and $\mathcal{J}$ in Eq.3.22 become equal to each other, so the added mass tensor $\mathcal{A}$ has only four independent entries rather than six as in a triaxial ellipsoid. With some algebra we show that a spheroid as a result has an additional integral of the motion: l_1, the angular momentum component along the x-axis. Although inherently available in the proof of the Kozlov-Onishchenko theorem, our explicit identification of this integral of the motion helps obtain physical understanding of how a spheroid can only display limited dynamics. The integral means the rate of rotation about the unequal axis, i.e., the long axis of a prolate spheroid or the short axis of an oblate spheroid, remains constant. So all changes in the angular momentum of the system are restricted to the plane perpendicular to the x-axis. We ask if a triaxial ellipsoid can therefore exchange kinetic energy more freely with the surrounding fluid than a spheroid can.

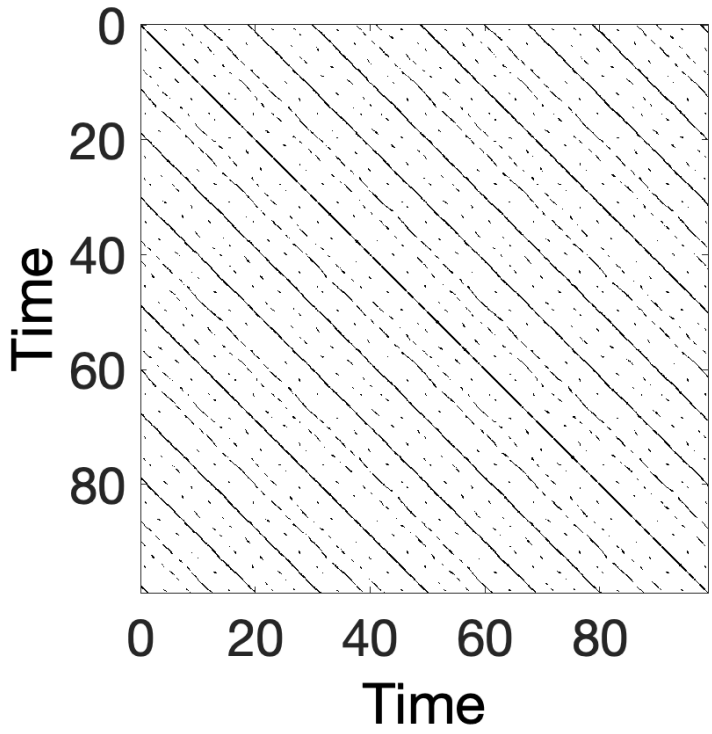

(a) Periodic Behaviour

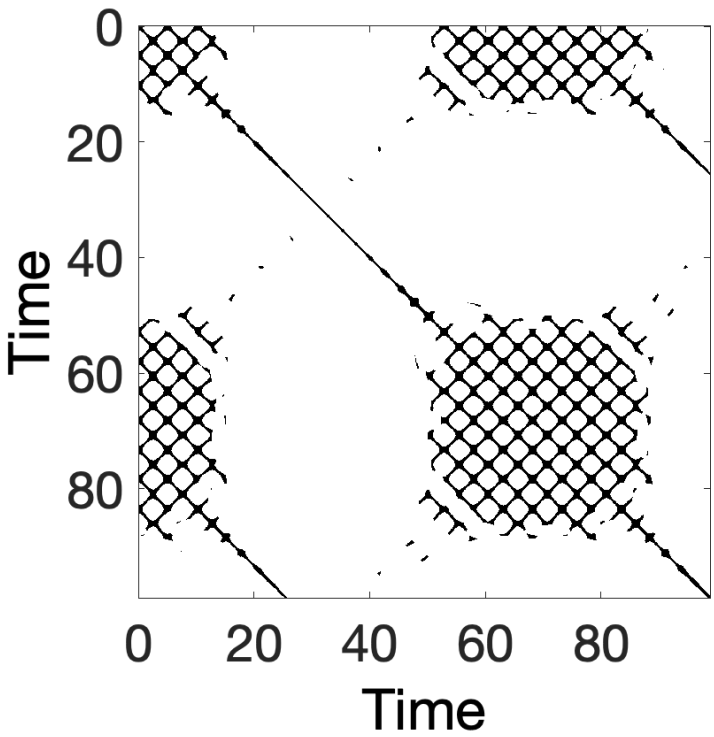

(b) Chaotic Behaviour

Figure 4.5: Recurrence plots, (a) Parameters as in Fig. 4.2. The regular diagonal bands are a signature of nonchaotic behaviour and (b) chaotic system, case as in Fig. 4.3. The complex structures are signature of chaotic behaviour. These results were produced by solving the Kirchhoff-Clebsch equations.

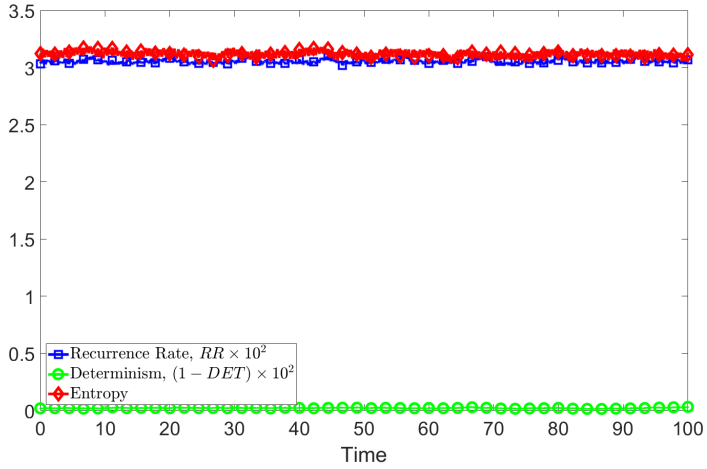

(a) Periodic Behaviour

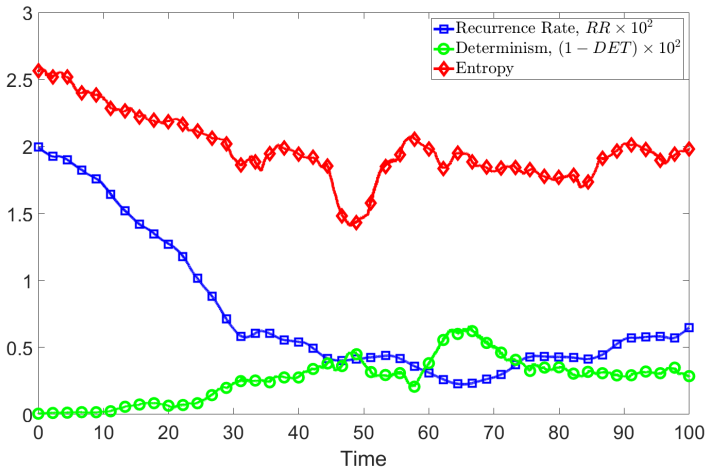

(b) Chaotic Behaviour

Figure 4.6: Recurrence statistics, (a) for the periodic system of Fig. 4.2b, and (b) for the chaotic system of Fig. 4.3b. These results were produced by solving the Kirchhoff-Clebsch equations.

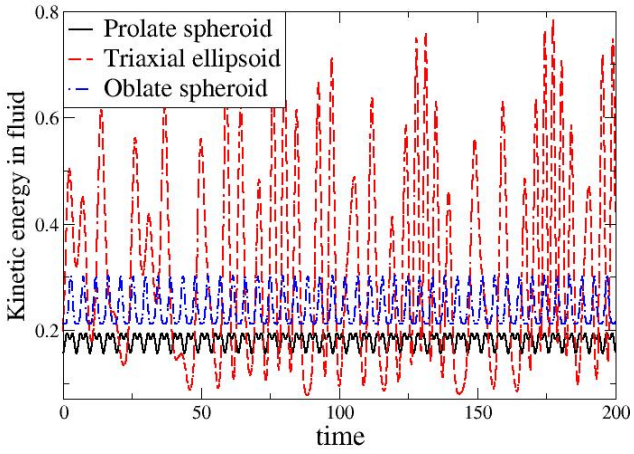

(a) Fraction of kinetic energy in fluid motion

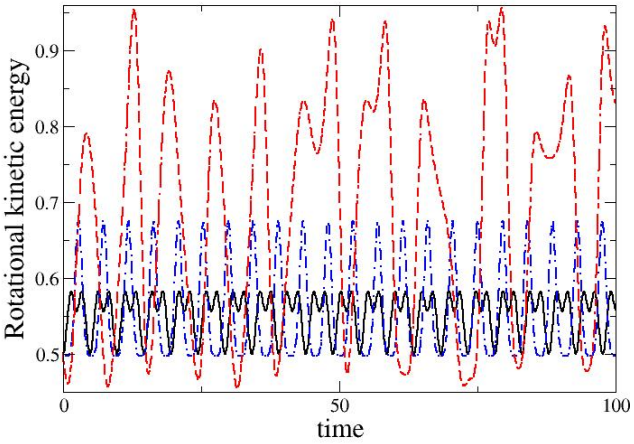

(b) Fraction of kinetic energy in rotational motion of the solid

Figure 4.7: (a) Fraction of kinetic energy in the fluid as a function of time for a triaxial ellipsoid, as compared to prolate and oblate spheroids of the same volume. These are solutions of the Kirchhoff-Clebsch equations. The energy exchange between fluid and solid is much larger in a triaxial ellipsoid. For clarity of viewing the curve for the oblate spheroid is displaced by 0.05 in the vertical. (b) Fraction of kinetic energy in rotational motion as a function of time in the same run as (a). Legend same as in (a). In all cases $\rho = 1$ and $E = 1$.

Figure 4.7a shows what fraction of the total kinetic energy at a given time is in the fluid. (The kinetic energy fraction in the solid is just this quantity subtracted from 1.) All conditions except the ratio of the axes are kept the same across the curves. This figure is just one example of a whole range of computations we have made, which give the same qualitative behaviour. Apart from varying ρ and E we have used many different orientations between the solid and its linear momentum, and between the linear and angular momenta. We thus show that the dynamics of prolate and the oblate spheroids are limited, in that they indulge only in minor exchanges of the kinetic energy between solid and fluid. The triaxial ellipsoid however wildly exchanges kinetic energy between solid and fluid. It is intuitive that this possibility of exchange provides for a rich range of tumbling dynamics. We digress briefly here to emphasise that added mass effects are of irrotational origin, and we therefore expect a triaxial ellipsoid to behave differently in a qualitative way in viscous flow as well as compared to a spheroid. Moreover, the Kirchhoff-Clebsch equations provide for an exchange of kinetic energy between motion of the centroid and that contained in tumbling. This exchange is shown terms of the fraction of total kinetic energy in rotational motion in figure 4.7b. The cases in the two sub-figures are the same. Given that $E = 1$ in all cases, the initial fraction in rotation is 0.5. Again we see that the fraction in rotational motion changes by a large amount in the case of the triaxial ellipsoid whereas the spheroids retain a ratio close to their starting value. We are able to get cases in the triaxial ellipsoid where the rotational energy goes from very low to high values, thus executing a complicated self-generated run-and-tumble dance.

Chaotic systems may have periodic windows in state-space, so we must have initial conditions giving rise to periodic motion. For the triaxial ellipsoid, we find an initial condition which gives rise to periodic behaviour, and plot, in figure 4.8, the ratios of kinetic energy in the fluid as opposed to the solid, and in rotational as opposed to translational motion. While in this case the solid remains primarily in rotational motion, the sharing between fluid and solid varies across most of the available range. This was never seen in the spheroid in all our attempts. Thus, even for periodic motion, more variety in dynamics is attainable with the triaxial ellipsoid than with spheroids.

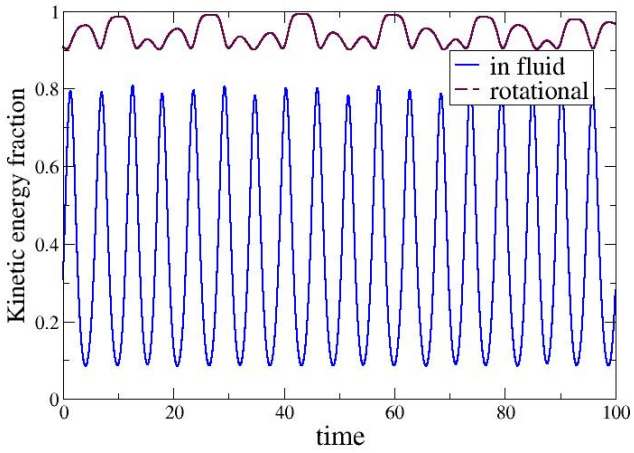

Figure 4.8: The triaxial ellipsoid in periodic motion, $\rho = 0.1$, $E = 1$. The plot shows the fraction of kinetic energy as a function of time in the fluid (blue solid line) and the fraction of kinetic energy in rotational motion (purple long-dashed line).

This brings us to an important question. What fraction of phase space is chaos seen in, and does this, for a given body shape, depend on ρ and E? We find that there are two limiting cases, where the motion cannot be chaotic even in a triaxial ellipsoid. When the fluid to solid density ratio approaches 0, the added mass of the fluid reaches to zero. In this case, $\boldsymbol{P}$ and $\boldsymbol{v}$ are collinear, and by dotting the second Kirchhoff-Clebsch equation with $\boldsymbol{\Omega}$, we show that $\boldsymbol{\Omega} \cdot \boldsymbol{L}$ is an additional integral of the motion. So the motion becomes integrable. In other words, the Kozlov-Onishchenko theorem is applicable when the fluid has non-zero density. In fact at zero fluid density, namely in vacuum, the dynamics reduces to periodic behaviour, as described in Landau and Lifshitz [64]. There the "asymmetrical top" as a triaxial ellipsoid is referred to, is shown to display an instability when spun around its intermediate axis, going into a three-dimensional tumbling state, but remaining periodic. Secondly when the initial linear momentum is zero, i.e., the body initially is only in rotational motion, or $E = 0$, the first of the Kirchhoff-Clebsch equations is identically zero, and the motion reduces to one of constant rotation. We realise from the Kozlov-Onishchenko theorem that for all other ρ and E, there will be some region of phase space where there is chaos. For a range of these parameters over several orders of magnitude, we estimate where the

probability of attaining chaotic dynamics from a randomly chosen set of initial conditions is higher than half. For this we ensure that the initial phase space conditions are uniformly sampled, and perform simulations for 20 or more initial conditions at each (ρ, E). Chaotic behaviour may be easily distinguished from periodic or quasiperiodic behaviour visually by examining the trajectory of the marker point, and an appealing example of a triaxial ellipsoid's tip covering a doughnut in quasiperiodic motion is shown in Fig. 4.9a in contrast to a chaotic orbit. The fastest way to make this distinction for a large number of initial conditions is to obtain Poincare sections, such as shown in Fig. 4.9b. The section chosen here is when p_2, the $y-$component of the linear momentum $\boldsymbol{P}$ goes through a 0 while decreasing, and the plane shows the x and z components of the angular momentum $\boldsymbol{L}$. Each colour and symbol here is the Poincare section corresponding to a different initial condition, with all non-dimensional parameters in the problem kept constant. Quasiperiodic orbits appear as single closed orbits (e.g. the black and blue symbols) or multiple closed orbits (e.g. the purple and green symbols) whereas chaotic orbits appear as scattered points on the plane. The parameters E and ρ are such that we are close to the border between predominantly chaotic and predominantly periodic behaviour, so depending on where in the sample space our initial condition lies, we can get both types of behaviour.

The boundary between a majority periodic state space and majority chaotic is shown in figure 4.10. By repeating the exercise close to the boundary points, we find that the results are robust. However we hasten to add that these are conclusions from a randomly sampled set of the phase space. As we move away from the boundary, the propensity for chaotic behaviour becomes predominant in the regime covered by the red squares in the figure, while periodic or quasiperiodic behaviour occurs with high probability in the black circled regime. Given our arguments for zero fluid density, and the importance of added mass for chaotic dynamics, it is intuitive that the propensity for chaos should increase with increasing fluid density. This is evident from the figure. So a body in a very light fluid, while technically in nonintegrable motion, is very unlikely to display chaos. At the right of the figure, the solid density approaches zero, we have a bubble in the shape of a triaxial ellipsoid in an inviscid fluid. The added-mass dominates the dynamics, and the system is almost always chaotic. We discussed earlier how $E = 0$ could never result in chaotic mo-

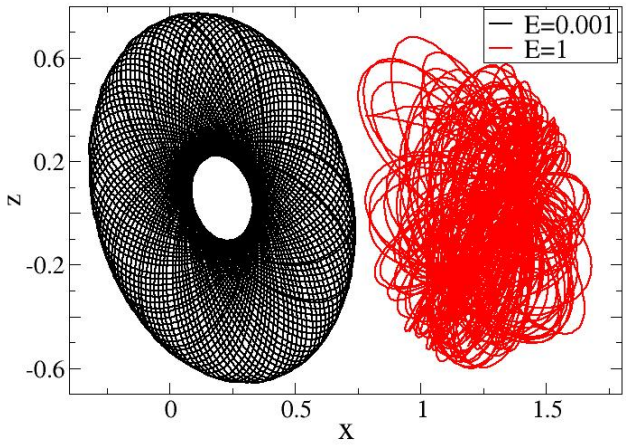

(a) Typical motion of the marker point relative to the centre of mass of the body

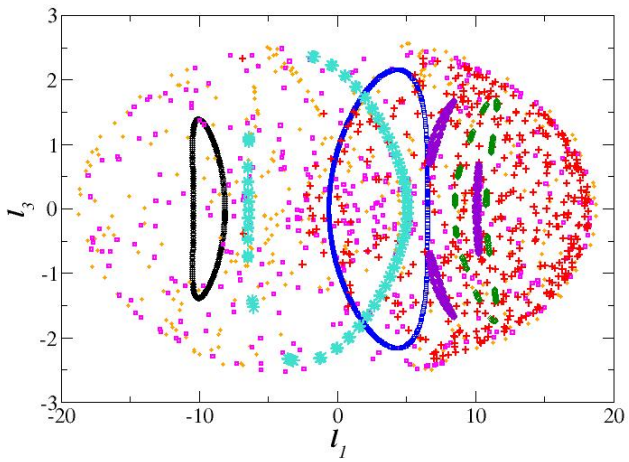

(b) Poincare section of angular momentum

Figure 4.9: Distinguishing chaotic dynamics from quasiperiodic. (a) Typical motion of the marker point relative to the centre of mass of the body in quasiperiodic ($E = 0.001$) and chaotic ($E = 1$) dynamics. Here $\rho = 1$. The view shown is in the x-z plane. The chaotic trajectory has been shifted on the x-axis by 1.1 for clearer viewing. (b) Typical Poincare section showing components of the angular momentum l_3 versus l_1 at the time when the linear momentum component p_3 goes through a zero while decreasing. Each colour or symbol stands for a different initial condition. Here $E = 10$ and $\rho = 0.1$. These are solutions of the KC equations.

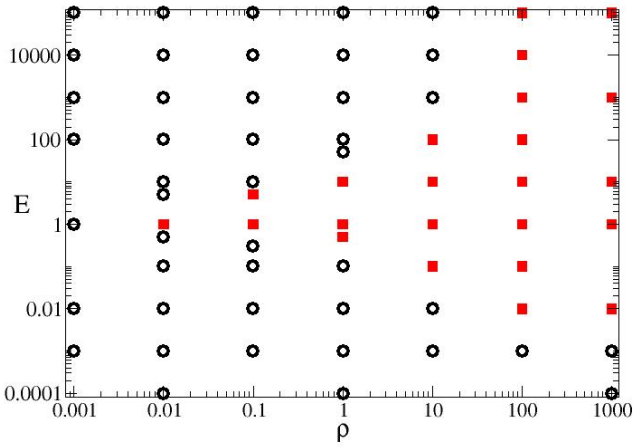

Figure 4.10: Orbital behaviour map of an ellipsoid with aspect ratio $a : b : c = 1 : 0.8 : 0.6$ submerged in an inviscid environment. At least twenty trials with randomly selected initial conditions were performed to obtain each point. Open black circles indicate periodic or quasiperiodic behaviour for a majority of initial conditions while the filled red squares indicate chaotic trajectories for a majority of initial conditions.

tion, and this propensity continues into small values of E for any density ratio. So in a fluid of any density, we see a triaxial ellipsoid will not display chaos if it was initially in predominantly rotational motion. We further see that at $E \sim 1$, where rotational and translational motion have comparable energy initially, is most conducive for chaotic motion, and under such initial conditions, the ellipsoid is wont to display chaotic motion even if it is a hundred times more dense than the fluid! At high values of initial linear momentum, while there is the possibility offered by the Kirchhoff-Clebsch system for converting translational to rotational motion, the system, at moderate fluid densities tend towards periodic dynamics, but at higher fluid densities displays chaos. We created an analogous figure (not shown) where we used the total kinetic energy rather than the ratio E as our parameter, and found that there was no simple boundary between chaotic and non-chaotic motion. So E is a physically appropriate choice.

We next zoom in on a smaller portion of the $\rho - E$ plane, namely $(E, \rho) = [(1 \ldots 30) \times (0.125 \ldots 8)]$, and fix an initial condition where the ellipsoid was initially set to rotate about the z axis, and translate along the $+y$ direction. At each point in this parameter space, for sufficiently

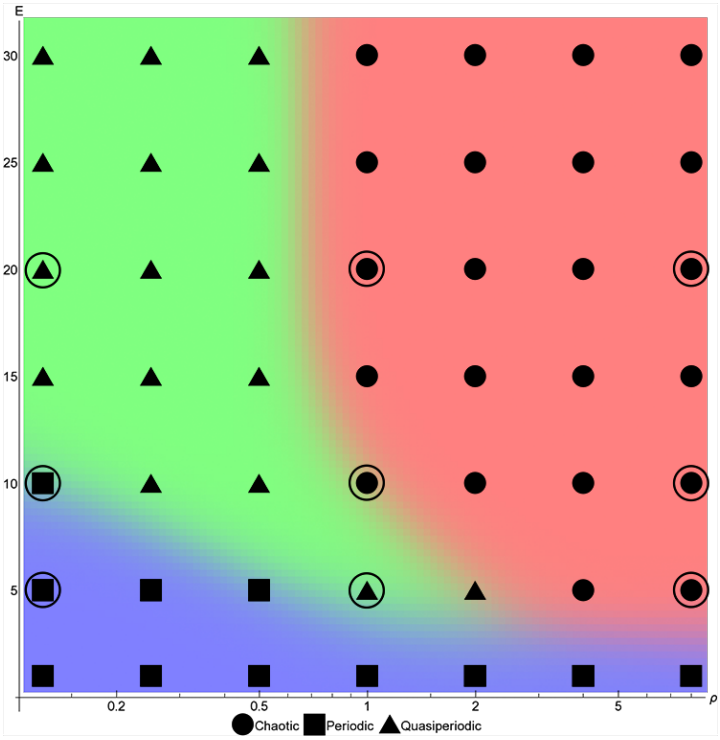

Figure 4.11: Orbital behaviour map of an ellipsoid with aspect ratio $a : b : c = 1 : 0.8 : 0.6$ submerged in an inviscid environment for energy ratios $1 \leq E \leq 30$ and density ratios $0.125 \leq \rho \leq 8$ for a single initial condition. A support-vector machine-learning algorithm was used to classify the regions of orbital behaviour. All cases (filled markers) have been characterised using Kirchhoff-Clebsch equations. Encircled points are those cases cross validated via DNS using our GISS solver.

large time-series (around 100 000 timesteps) a recurrence plot was generated. An RQA analysis was then performed and the criteria presented in Section 4.3 were used to determine the system behaviour. The progression in the regime space from periodic to quasiperiodic to chaotic is clearly evident in Fig. 4.11. Note that while the trend in this regime window is in broad agreement with the boundaries shown in Fig. 4.10, specific points may differ because the present figure is the result of one initial condition. Since the computational requirements of GISS are considerable, we selectively performed DNS for the parameter pairs denoted by large circles in this figure. All cases have been run for 100000 time steps. In each case we obtained the same result from GISS as from the Kirchhoff-Clebsch equations. An example of the DNS results is shown in Fig. 4.12, in the form of the orbit tracked by a triaxial ellipsoid along with the resulting recurrence plot at two different E. When $E = 1$, Fig. 4.12a shows quasiperiodic behaviour, which is confirmed by the recurrence plot in Fig. 4.12c, which shows only regular diagonal lines. Our RQA statistics confirm these conclusions. At the higher energy ratio, here when $E = 10$, it can be seen in Fig. 4.12b that the orbit of the marker point becomes irregular and Fig. 4.12d reveals its chaotic nature.

4.4.1 *Departures from sphericity*

We may create a triaxial ellipsoid, beginning with a neutrally buoyant sphere of radius R, and stretching outwards by a length ϵ along one axis and inwards along another whilst conserving volume. One would thus obtain a triaxial ellipsoid with the following semi-axes:

$$\left[R(1+\epsilon),\ R,\ R\left(1-\frac{\epsilon}{1+\epsilon}\right)\right]. \tag{4.12}$$

It is obvious that we obtain a sphere at $\epsilon = 0$, so ϵ may be called the departure from sphericity parameter. According to the Kozlov-Onishchenko theorem, any departure from $\epsilon = 0$ should make the system nonintegrable. We vary ϵ in the range 10^{-5} to 1 covering a wide variation of geometry, from a near-sphere to a highly triaxial ellipsoid. At the energy ratio $E = 20$, we solve the Kirchhoff-Clebsch equations to simulate the orbital behaviour. We choose this energy ratio given its more than even

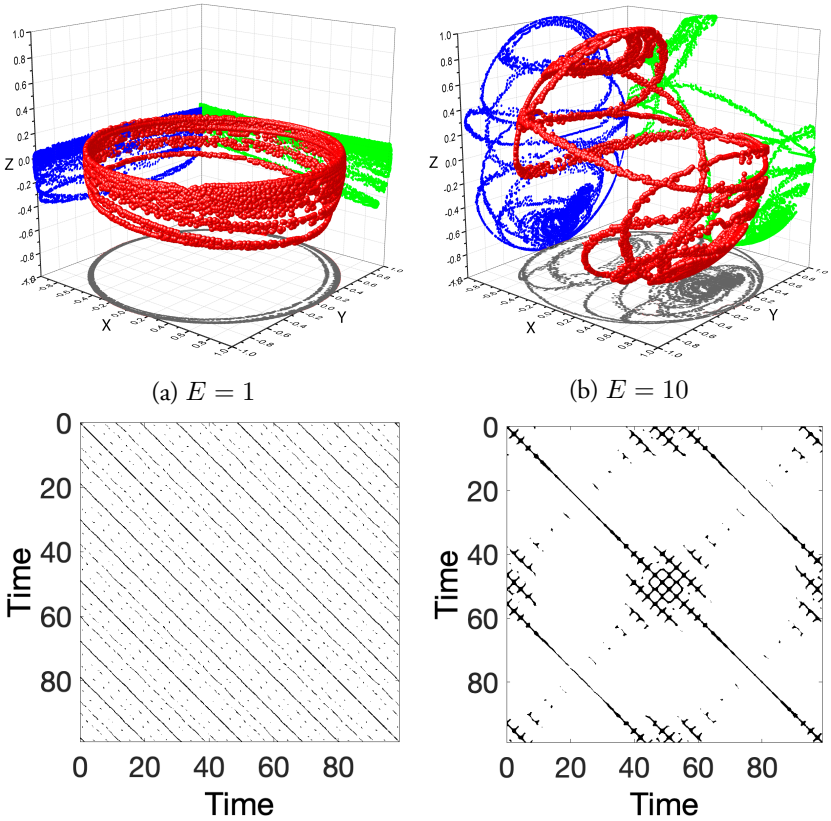

(a) $E = 1$ (b) $E = 10$

(c) $E = 1$ (d) $E = 10$

Figure 4.12: DNS result: (a, b) Orbits tracked and (c, d) corresponding recurrence plots by an ellipsoid with aspect ratio $a : b : c = 1 : 0.8 : 0.6$ in an inviscid fluid at energy ratios of $E = 1, 10$, respectively and $\rho = 1$.

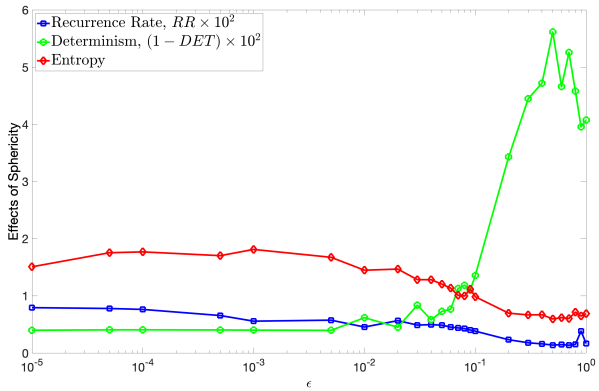

Figure 4.13: The dependency of the Recurrence Rate, Determinism and Entropy on ϵ, which is the perturbation from the a spherical shape. Volume of the ellipsoid remained constant as ϵ varied at energy ratio of $E = 20$ and $\rho = 1$.

likelihood of tracking a chaotic orbit for a triaxial ellipsoid, as seen from sections above. We then perform RQA for each of these cases to obtain orbital statistics. Note that this part of the study uses only one initial condition. The idea is to show the qualitative dependence of the dynamics on ϵ. Figure 4.13 shows the dependence of recurrence rate, determinism, and entropy on ϵ. These RQA statistics were calculated using the entire time-series of the respective simulations and they were all of the same length of time, (100 000 time-steps). In the range $10^{-5} \leq \epsilon \leq 4 \times 10^{-3}$, when the body is nearly spherical, it exhibits a non-chaotic behaviour for the run-times, as evidenced by the normalised determinism remaining constant and $(1 - DET) \times 10^2$ close to zero. It must be noted that lower but non-zero values of ϵ result in a periodic behaviour. In the range $10^{-2} \leq \epsilon \leq 10^{-1}$, DET demonstrates a small drop; around $\epsilon > 10^{-1}$, an abrupt change in the system behaviour is observed. All the RQA parameters switch from non-chaotic to fully chaotic, as DET reduces to levels similar to other chaotic systems (presented in the sections above). As per Kozlov and Onishchenko [57], any of these triaxial ellipsoids satisfies the necessary conditions for non-integrability. However, our results show that there is a critical departure from sphericity below which it is easier to obtain periodic orbits. We note that the nearly spherical cases have a relatively high recurrence rate and high entropy. This means that, in this range, the Lyapunov exponents for these systems would be relatively small [11]. Therefore, it could be argued that the timescale needed by the system to

display chaotic characteristics would have been longer than the run-time of the simulation, and that the abrupt change in behaviour at $\epsilon = 10^{-1}$ can be explained by the Lyapunov timescale becoming shorter than the run-time of the simulation. We leave this question open.

4.5 ORBITS IN VISCOUS ENVIRONMENTS

Since our study so far has been on an inviscid fluid it is natural to ask what would happen in a real fluid. Viscous drag could have a dampening effect, but more important, it could be asked if vortex shedding would introduce chaos into the system rendering the inviscid study irrelevant. We show in this section that in a viscous case as well, added mass continues (as it is expected to) to be an important player in the system, and insights obtained above from the above study are important to understand the behaviour. We also point out how vortex shedding indeed can change the dynamics, and in particular give rise to chaotic orbits executed by a spheroid. Thus while the earlier sections elucidated the role of added mass, its combination with viscous forces is presented here to complete the study.

We define the ellipsoid Reynolds number as $Re_p = aU_0/\nu$, where a is length of the major axis, U_0 is a characteristic velocity here chosen as the magnitude of the initial translational velocity $\boldsymbol{v}$ given to the ellipsoid, and ν is the kinematic viscosity of the surrounding fluid. Considering that the velocity of the solid evolves during the simulation, this Re_p must be treated as an indicative value. The motion of the solid is essentially dependent on the accurate resolution of flow (and hence, viscous drag) immediately around the body and the exact imposition of the no-slip boundary condition. Our mesh adaptation strategy has ensured that the mesh is sufficiently resolved in the immediate vicinity of the solid. Our results shown in Section 4.2 demonstrate that a mesh resolution of $R_m = 128$ suffices for the exact imposition of no-slip conditions on the solid and full resolution of the viscous stress tensor around it.

4.5.1 *Motion of triaxial ellipsoids*

Fig. 4.14 and 4.15 shows recurrence plots for orbits of a triaxial ellipsoid with $Re_p = 10000$ at various energy ratios, similar to conditions for cases under invsicid environments shown in Fig. 4.12. It can be seen that motion is non-chaotic at $E = 1$. This shows that despite viscosity affording vortex shedding, the inviscid predictions are a good indicator of the behaviour of an ellipsoid in a real fluid for this case.

At short times, a chaotic pattern is observed for $E = 20$, similar to the inviscid case, in Figs. 4.14b and 4.14d. However, the chaotic nature is suppressed as time progresses, presumably because of viscous damping. First, the angular velocities become vanishingly small leading to the ellipsoid ceasing to rotate while it continues to translate. At $E = 20$ the initial rotational energy is far smaller than the initial translational energy, so viscous damping acts earlier on the rotational energy. Eventually, over very long times, the translational velocity as well becomes small and we expect the ellipsoid to come to a halt.

4.5.2 *Motion of prolate spheroids*

In Section 4.2, we have seen how prolate spheroids display no chaos in inviscid environments. Here, we consider the same ellipsoid of revolution $(a : b : c = 1 : 0.7 : 0.7)$ subjected to an impulse in a viscous environment characterised by $Re_p = 10000$. Our DNS results presented in Fig. 4.16 and 4.17 demonstrate a highly complex pattern of orbital behaviour. At $E = 1$, the recurrence plot and statistics shown in Figs 4.16a and 4.16c demonstrate that the orbit is demonstrably non-chaotic. It must be recalled from Figs 4.2a, 4.5a and 4.6a that in an inviscid environment under identical initial conditions, the prolate spheroid tracks a quasiperiodic orbit. At $E = 20$, as shown in Figs. 4.16b and 4.16d, the prolate spheroid tracks a chaotic orbit that does not seem to dampen completely (at least within the simulation time). This is unlike a prolate spheroid under any ρ or E in inviscid fluid which will demonstrate non-chaotic behaviour, in accordance with the Kozlov and Onishchenko [57] theorem.

The RQA statistics shown in Fig. 4.16d confirms that at the higher energy ratio, the system demonstrates a chaotic behaviour of RR and

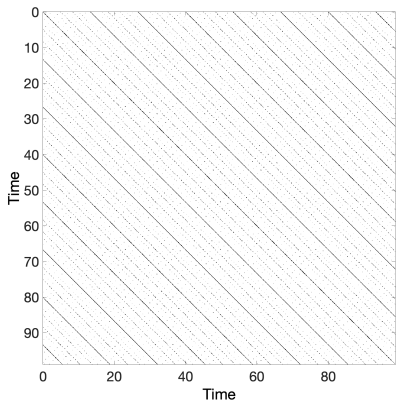

(a) $E = 1$

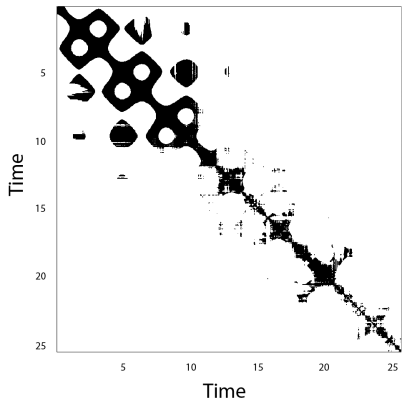

(b) $E = 20$

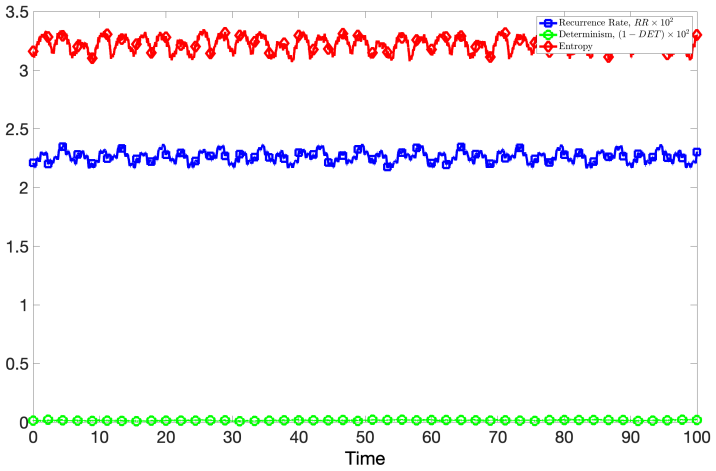

(c) $E = 1$, RQA statistics

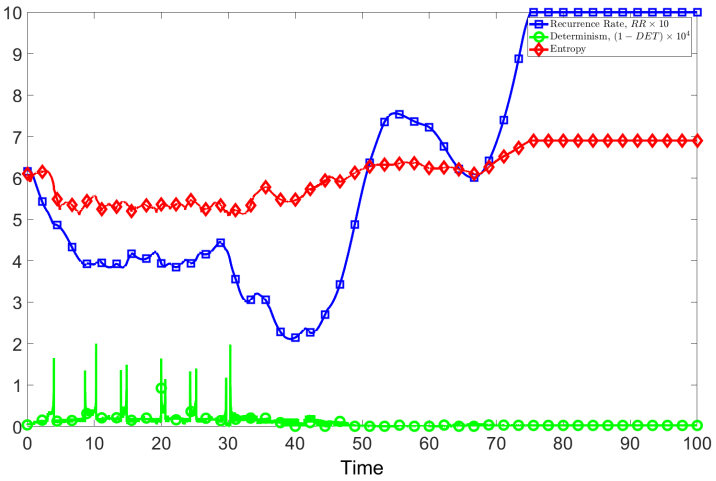

(d) $E = 20$, RQA statistics

Figure 4.14: Motion of a triaxial ellipsoid with aspect ratio $a : b : c = 1 : 0.8 : 0.6$ in viscous fluid. (a, b) Orbit recurrence plots and (c, d) Orbit RQA statistics under $Re_p = 10000$ at energy ratios of $E = (1, 20)$ respectively, while $\rho = 1$.

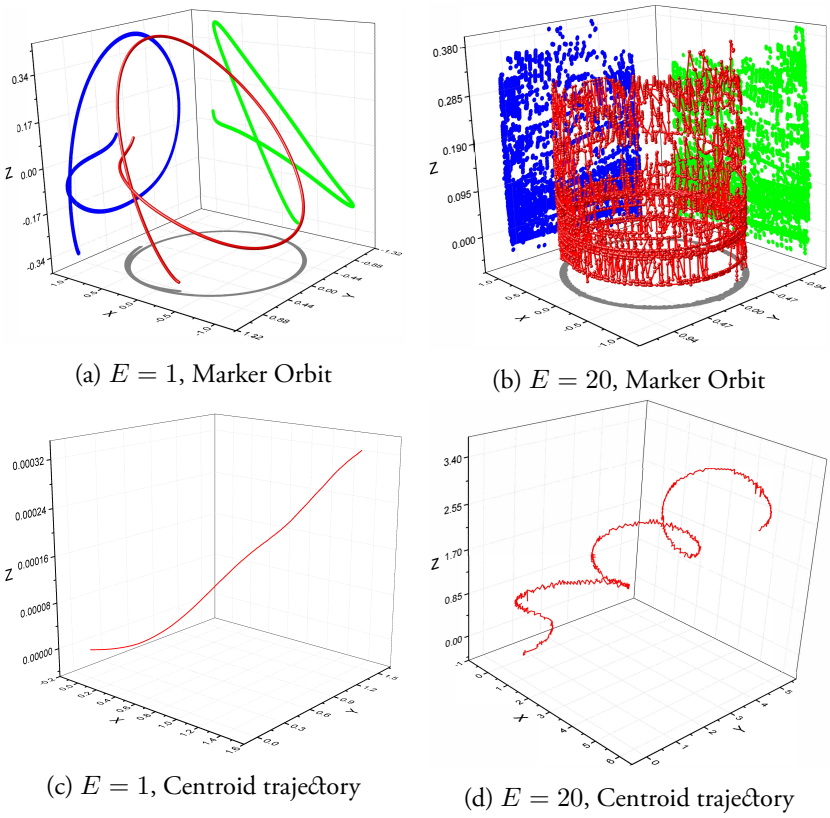

(a) $E = 1$, Marker Orbit

(b) $E = 20$, Marker Orbit

(c) $E = 1$, Centroid trajectory

(d) $E = 20$, Centroid trajectory

Figure 4.15: Motion of a triaxial ellipsoid with aspect ratio $a : b : c = 1 : 0.8 : 0.6$ in viscous fluid. (a, b) Marker point orbits and (c, d) Centroid trajectories under $Re_p = 10000$ at energy ratios of $E = (1, 20)$ respectively, while $\rho = 1$.

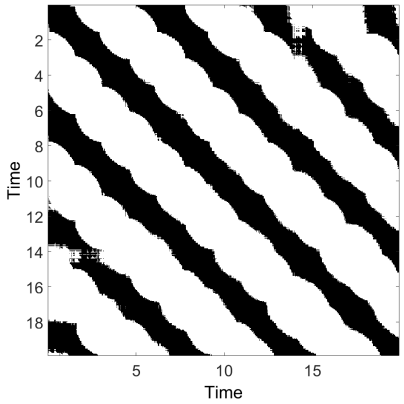

(a) $E = 1$, Recurrence plot

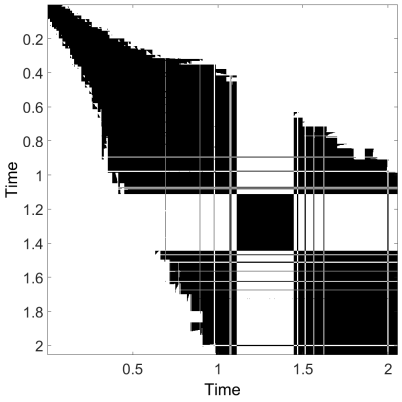

(b) $E = 20$, Recurrence plot

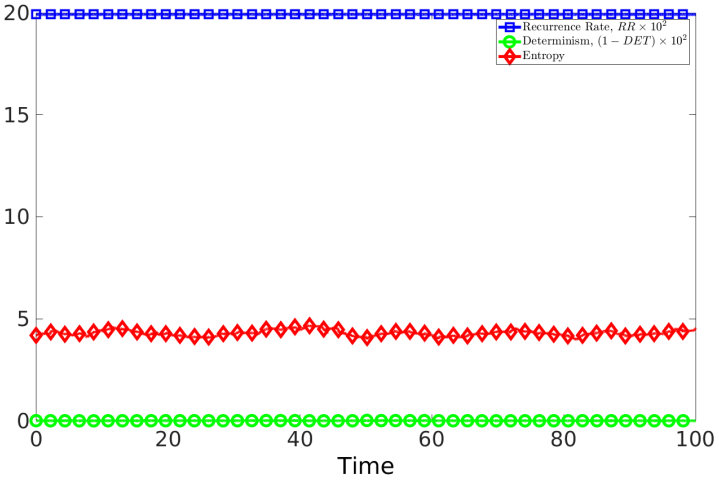

(c) $E = 1$, RQA statistics

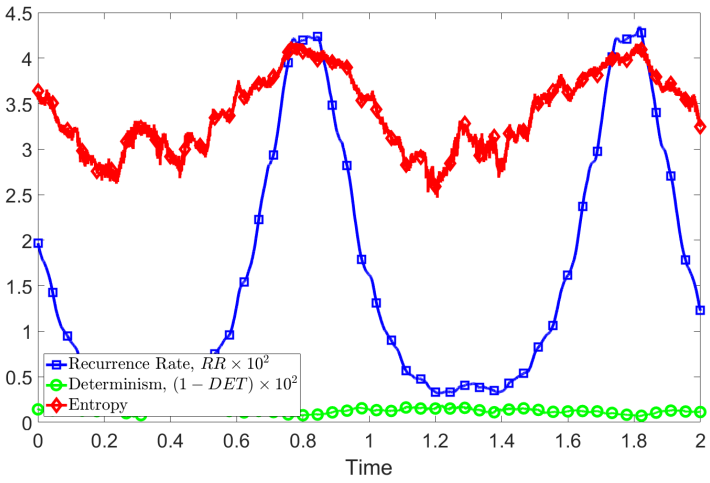

(d) $E = 20$, RQA statistics

Figure 4.16: (a, b) Orbit recurrence plots and (c, d) Orbit RQA statistics by a prolate spheroid defined by $a : b : c = 1 : 0.7 : 0.7$ under a viscous system with $Re_p = 10000$ at energy ratios of $E = 1, 20$, respectively and $\rho = 1$.

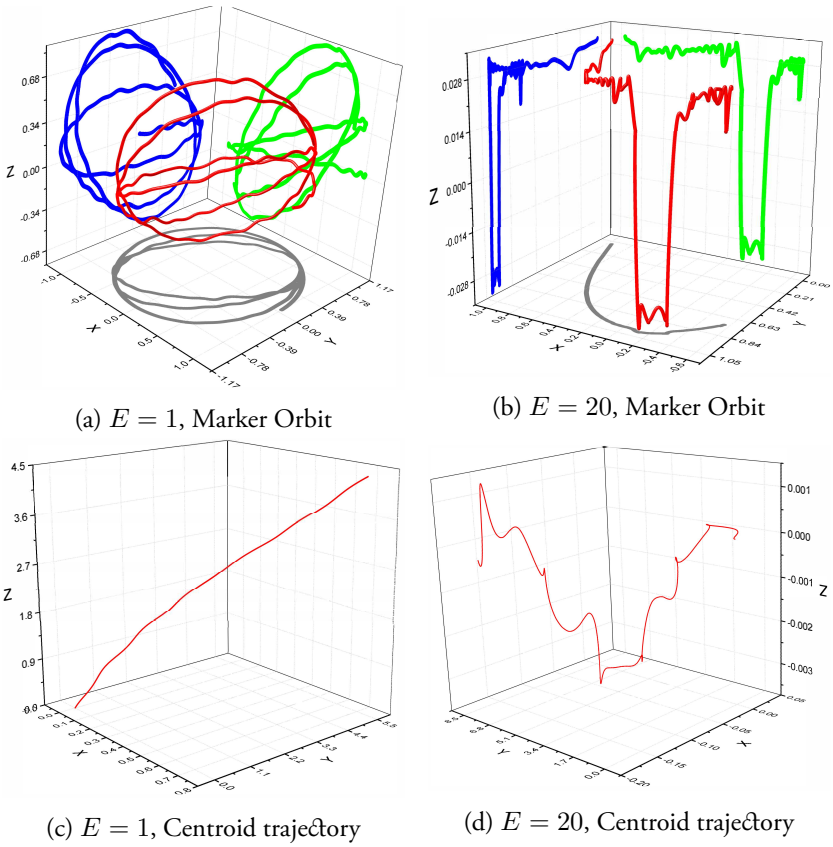

(a) $E = 1$, Marker Orbit

(b) $E = 20$, Marker Orbit

(c) $E = 1$, Centroid trajectory

(d) $E = 20$, Centroid trajectory

Figure 4.17: (a, b) Orbits and (c, d) centroid trajectories tracked by a prolate spheroid defined by $a : b : c = 1 : 0.7 : 0.7$ under a viscous system with $Re_p = 10000$ at energy ratios of $E = 1, 20$, respectively and $\rho = 1$.

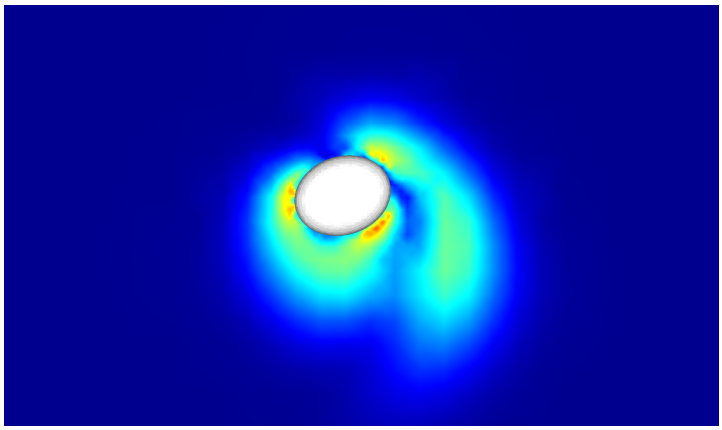

Figure 4.18: The vorticity field around a neutrally buoyant ellipsoid with aspect ratio $a : b : c = 1 : 0.7 : 0.7$ at $Re_p = 10000$ at energy ratios of $E = 20$ and $\rho = 1$. The colour shading is proportational to $|\nabla \times \boldsymbol{u}|$. Asymmetrical vortex shedding can clearly been seen in the figure.

$ENTR$. An examination of the trajectories of the marker point in Fig. 4.17b, and the centroid in Fig. 4.17d however, reveal that the trajectory is practically planar, with the centroid effectively confined to the $x - z$ plane and the marker point nearly so. This is in line with our expectations from our inviscid studies. To isolate the cause of chaos, we plot a picture of the instantaneous vorticity field around the prolate spheroid obtained from our DNS in Fig. 4.18. A partially detached vortex can be seen. This vortex distorts the surface pressure field, giving rise to asymmetric force and torque. As successive vortices are generated and shed, the ellipsoid will be disturbed from a periodic orbit. This indicates that viscosity breaks the symmetry of the system by vortex shedding.

In our viscous simulations thus, we see the effects of added mass: in keeping the dynamics periodic for smaller energy ratios, while restricting the dynamics to two-dimensions at higher energy. We also see the effects of viscosity, in producing chaos where there was none by vortex shedding, and by suppressing chaos at long time by dissipation. We have also conducted simulations at lower Reynolds numbers (not shown) in which viscous damping dominates.

4.6 CONCLUSION

In this chapter, the DNS and theoretical methodologies described in Chapter 3 have been used to understand the dynamics of a single ellipsoid tumbling in inviscid and viscous environments. Five nondimensional parameters which affect the dynamics have been identified: the ratios b/a and c/a of the ellipsoid axes, the fluid/solid density ratio ρ, the ratio E of initial kinetic energy in translational to rotational motion, and the particle Reynolds number. Over a very large parameter range of ρ and E, it is seen that the propensity of chaos depends strongly on these ratios.

5

EFFECTS OF FLUID MIXING AND VISCOSITY GRADIENTS

This chapter demonstrates the use of GISS solver described in Chapter 3 to quantify the effect that tumbling ellipsoids in inviscid and viscous environments have on the mixing of the surrounding fluid. The problem adds further complexity to those encountered in Chapter 4, through an additional advection-diffusion equation.

There is a result of dynamic systems theory that at least three degrees of freedom is necessary for a system to have chaotic behaviour. In the case of three-dimensional flows, the spatial basis vectors provide the needed degrees of freedom. Therefore, in general, chaotic behaviour is expected. Tan et al. [105] has shown that mixing in fluid systems is chaotic for all non-stationary flows using simulation. There is the exception that when the flow has symmetries that reduce the number of degrees of freedom, chaos would be prevented or suppressed. In these flows, the Lagrangian trajectories of fluid parcels are confined to closed tubes, and shear-induced mixing can only proceed within these tubes. However, the addition of the immersed solid to the problems increases that degrees of freedom by at least six. This further increases the likelihood of chaotic dynamics appearing.

As in Chapter 4, when the axes of a triaxial ellipsoid are fixed, three parameters characterise the system: the ratio of the densities of fluid and solid, and the total kinetic energy of the fluid-solid system and the particle Reynolds number. Our objective in this chapter is to show how these parameters affect the dynamics of mixing. We show that in the cases where chaotic dynamics are displayed, local mixing of the fluid is enhanced. Moreover, ellipsoids of rotation and triaxial ellipsoids are observed to exhibit substantially different behaviour in the presence of viscosity gradients. Alongside basic validation against mixing, we also present analysis of chaotic mixing using recurrence quantification method presented in Chapter 4. Given that this is the first such attempt to study mixing with immersed solids using direct numerical simulations and quantification of chaotic mixing,

we still consider the results in this chapter (while exhaustive) to be preliminary.

5.1 ADVECTION-DIFFUSION OF TRACERS

This section will give a brief overview of the methodology that GISS uses to numerically solve the advection-diffusion equation for the tracer, α;

$$\frac{\partial \alpha}{\partial t} + \nabla \cdot (\boldsymbol{u}\alpha) = \nabla \cdot (D\nabla\alpha) + S_\alpha + \nabla \cdot \mathbf{s}_\alpha, \tag{5.1}$$

Where D is the diffusion coefficient of the tracer, the model includes two types of sources for the tracer: S_α is the scalar source term for trace. $\mathbf{s}_\alpha$ is the source term for vector flux sources. This generality allows Gerris to simulation a vast range of systems [86]. Eq. 5.1 needs to be discretised in-order to by solved over the octree mesh generated by Gerris as described in Chapter 3. Gerris adopts a discretisation scheme of the form,

$$\begin{aligned}\frac{\alpha^{n+1} - \alpha^n}{\Delta t} + \nabla \cdot (\boldsymbol{u}^{n+1/2}\alpha^{n+1/2}) = (1-\beta)\nabla \cdot (D^n \nabla \alpha^n) \\ + \beta\nabla \cdot (D^{n+1}\nabla\alpha^{n+1}) \\ + S^n_\alpha + \nabla \cdot \mathbf{s}^n_\alpha\end{aligned} \tag{5.2}$$

Where β varies from 0.5 to 1.0: with the default value of $\beta = 0.5$. The default value corresponds to the Crank-Nicholson scheme, which has second-order accuracy in time. The value, $\beta = 1$ corresponds to the Forward Euler scheme, which is more robust against oscillations but only has the first-order accuracy in time. Thereby allowing the scheme's numerically behaviour to adjust in order to ensure the simulation numerically converges. The equation can be rewritten into a form close to the Poisson's equation given in 5.1,

$$\begin{aligned}\alpha^{n+1} - \nabla \cdot (\beta\Delta t D^{n+1}\nabla\alpha^{n+1}) = \alpha^n - \nabla \cdot (\Delta t \boldsymbol{u}^{n+1/2}\alpha^{n+1/2}) \\ + \nabla \cdot ((1-\beta)\Delta t D^n \nabla\alpha^n) \\ + S^n_\alpha + \nabla \cdot \mathbf{s}^n_\alpha\end{aligned} \tag{5.3}$$

We assume that the mesh cell is the control volume, dV and that a constant value of the tracer α is maintained across the cell. This allows integration of the above discrete equation over the cell, to obtain the following set of equations.

The temporal terms have the form:

$$\iiint_V \alpha dV = a_v \alpha d\ell_1 d\ell_2 d\ell_3 \; = a_v \alpha g_c h^3 \tag{5.4}$$

where h is the length of the mesh cell. We use a general system of orthogonal curvilinear coordinates defined by (x_1, x_2, x_3). Here, gm_i are the metric factors of each coordinate x_i such that $d\ell_i = gm_i dx_i$). The metric factors can be collected as $g = gm_1 gm_2 gm_3$. The subscript c denotes that the metric factor is computed at the centre of mass of the cell, and a_v is the volume fraction of the fluid in the cell. It has a value of 1, except in the case when cell is transacted by a solid segment, such as on a fluid-solid interface.

The advection terms are found by applying Gauss's theorem to eq. 5.1 and utilising the advection fluxes through the cell's contour, C,

$$\iiint_V \nabla \cdot (\mathbf{u}^{n+1/2} \alpha^{n+1/2}) \Delta dV = \iint_S \Delta t (\mathbf{u}^{n+1/2} \alpha^{n+1/2}) \cdot \boldsymbol{n} dA \tag{5.5}$$

$$= \sum_C {u_f}^{n+1/2} \alpha_f^{n+1/2} \Delta t \, s_f g_f h^2. \tag{5.6}$$

Where u_f and α_f are the normal velocity to the face and the value of the tracer evaluated on the face, respectively. Here, s_f is the face fraction that is not transected by a solid body and g_f is the metric factor that

is evaluated on the face. The diffusion terms are treated similarly to the advection term, resulting in

$$\iiint_V \nabla \cdot (\Delta t D \nabla \alpha) dV = \iint_S \Delta t D \nabla \alpha \cdot \boldsymbol{n} dS \tag{5.7}$$

$$= \sum_C \Delta t D_f g_f s_f h (h \nabla^f \alpha). \tag{5.8}$$

The equations can be reformulated in the following manner:

$$\begin{aligned}
&\alpha^{n+1} - \frac{1}{a_v g_c h^2} \sum_C \frac{\Delta t D_f \, g_f \, s_f \, \beta}{g m_f} \left(h \nabla^f \alpha^{n+1} \right) = \\
&\alpha^n - \frac{1}{a_v g_c} \sum_C \frac{\Delta t \, s_f g_f}{h} {u_f}^{n+1/2} \alpha_f^{n+1/2} + S_\alpha^n \, \Delta t \\
&+ \frac{1}{a_v g_c} \sum_C s_f^n \Delta t \, s_f g_f / h + \frac{1}{a_v g_c h^2} \sum_C \frac{\Delta t D_f g_f \, s_f \, (1 - \beta)}{g m_f} \left(h \nabla^f \alpha^n \right)_f
\end{aligned} \tag{5.9}$$

gm_f takes into account that an orthogonal curvilinear coordinate system could affect the expression of the normal gradient for the tracer. In Chapter 3, we outlined how Gerris was modified into GISS and allow it to solve solid-fluid systems. However this required modification of the software components that implement the advection scheme. Before we ran the mixing simulations described in the previous section, we validated that the modification to the system did not affect the advection scheme.

5.1.1 *Validating the Advection equation using GISS*

In order to check that the modifications made in the creation of GISS did not impair its ability to solve the advection equations, we validated against the case that Popinet [86] proposed for Gerris. The case is an example of two viscous fluids mixing at low Reynolds number. These fluids are identical in terms of their physical properties, however a scalar tracer differentiates them.

The fluid domain consists of a channel with bounded on one side by an impermeable wall within which, a cavity is situated. Fig. 5.1a shows the initial setup for this case. The fluid in the cavity is differentiated from the bulk flow by the tracer. The tracer has constant values in either fluid and

(a)

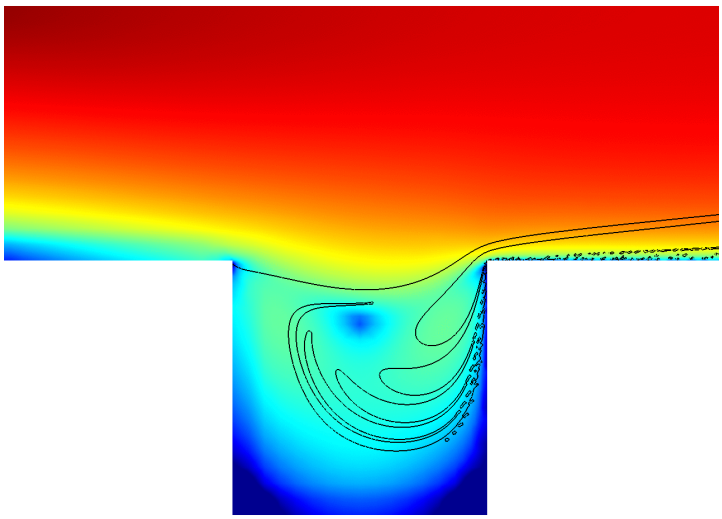

(b)

Figure 5.1: Problem definition: Validation case from Gerris, a pocket in an impermeable wall which contains a region of fluid with higher value of the scalar tracer than the bulk. The black line indicates the transition of the tracer and the colour represent the vorticity of the fluid, $|\nabla \times \boldsymbol{u}|$

the change of the value of the tracer makers the interface between the two fluids it is shown by a black line, as can be seen in Fig. 5.1b. The mixing of the fluids is driven by applying a varying Poiseuille flow to the upper half of the domain on the left boundary. The flow is varied by a sinaiodal velocity boundary condition to the left hand side of the domain, suggested by Popinet [86]. The boundary condition has the following form:

$$\boldsymbol{u}_x = \frac{1}{8}(2\boldsymbol{x}_y - 1)^2 \cos(2\pi t[\frac{ReSr}{Re}] + 1), \tag{5.10}$$

here $\boldsymbol{u}_x$ is the x component of the fluid velocity, and $\boldsymbol{x}_y$ is the y-component of the position vector.Horner et al. [40] has investigated these kinds of flows, both experimentally and numerically. Their work was used as the reference against which Gerris was compared. Therefore, it was also the datum that was shown in the validation of GISS. Horner et al. [40] found that these flow were parameterised by their Reynolds number, $Re = (L\rho_f \boldsymbol{u}_x)/\mu$ and the product of the Reynolds number and Strouhal number, Sr. The Strouhal number describes oscillating flow mechanics. In this case, it has the following definition: $Sr = L/(\boldsymbol{u}t_0)$, where L is the depth of the cavity and t_0 is the period of oscillating Poiseille flow. For this case, both parameters have low numerical values.

These sorts of flows are of interest to geophysical mixing processes, such as magma mixing in volcanic systems [93] and the injection of water into oil-bearing structures [31]. The fluid in the cavity is replaced over time by the main flow as a series of lodes. These lodes are injected into the flow as the driving oscillation reaches a turning point in its cycle. Fig. 5.2 shows the results of this process, Fig. 5.2a was produced by GISS and Fig. 5.2b is experimental results from Horner et al. [40]. In both cases, the flow was allowed to experience the same number of flow oscillations. From Fig. 5.2 it be seen that there is good agreement between GISS and experimental data. Not shown here, but GISS and Gerris produced identical output for Fig. 5.2a. This good agreement with experimental data from fluid mixing and Gerris gives confidence that the modifications made in the development of GISS, did not affect its ability to simulate mixing processes.

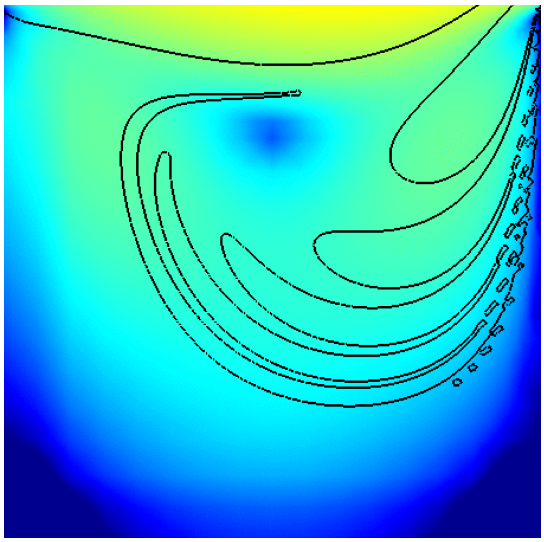

(a)

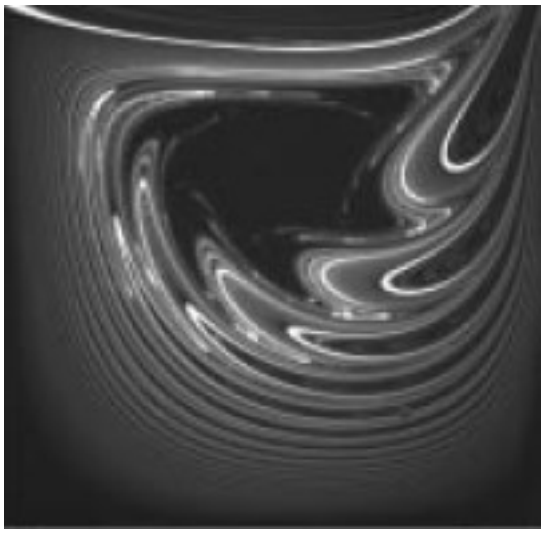

(b)

Figure 5.2: Comparing the shape of the manifold interface from the simulation using GISS, as seen in Fig. 5.2a and to experimental results from Horner et al. [40], as seen in Fig 5.2b, we see a very close agreement. The simulation and experimental data have the following conditions: $Re = 31$ and $ReSr = 3.09$

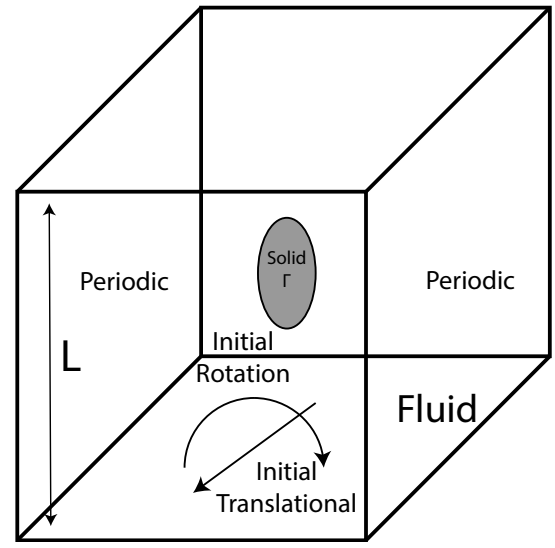

(a)

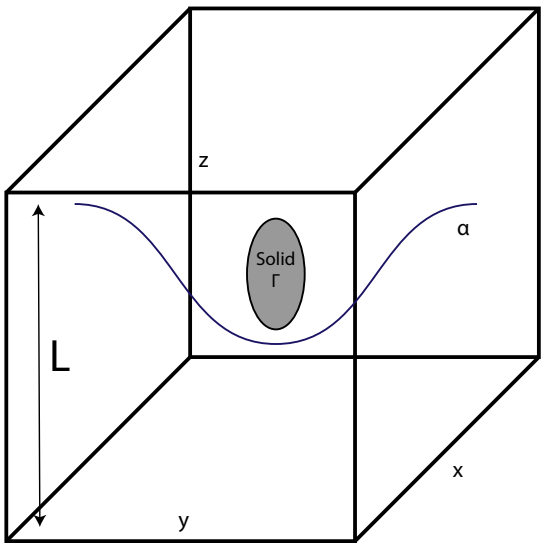

(b)

Figure 5.3: Problem definition (a) A general ellipsoid with aspect ratio $a : b : c$ immersed in a fluid with initial energy ratio E, and (b) schematic example of the initial spacial distribution of a scalar field, α which may be coupled to the viscosity, μ

Simulation Parameters	Triaxial		Symmetric	
	Case 1	Case 2	Case 3	Case4
E	1	20	1	20
Re_p	10000	10000	10000	10000
ρ_s	1000	1000	1000	1000
(a, b, c)	$(1, 0.8, 0.6)$	$(1, 0.8, 0.6)$	$(1, 0.7, 0.7)$	$(1, 0.7, 0.7)$
Mass	2010	2010	2053	2053
Length	16	16	16	16
$\|\boldsymbol{v}\|$	5	5	5	5
$\|\boldsymbol{\Omega}\|$	8.73	1.95	9.16	2.05

Table 5.1: Simulation parameters that were used by GISS to simulate the effects of mixing. Re_p calculated using the minimum value of viscosity if it varied.

5.2 PROBLEM STATEMENT FOR MIXING WITH IMMERSED SOLIDS

Working on the basis from Chapter 4, we consider a solid shaped as a general ellipsoid of axes a, b and c, immersed in a cubical fluid domain of size $L \gg (a, b, c)$ as shown in Figure 5.3a. Additionally, we define a scalar tracer, α, which will be advected by the fluid flow. This tracer can represent any physical condition that can be transported by the fluid, such as temperature and the concentration of a chemical species which may or may not influence viscosity, as can in seen in Drew and Passman [24]. We reuse the definitions for the following dimensionless parameters, including density ratio ρ and energy ratio, E. However, since we are dealing with viscous flows, the particle Reynolds number is needed as well, $Re_p = \frac{2a\boldsymbol{u}\rho_f}{\mu}$. This massively increases the size of the configuration space that is available to us to explore. Please note the we will be neglecting the effects of diffusion from this point forward, naming that $D = 0$. In order to have a frame of reference well will use initial conditions that are comparable to those used in Chapter 4.

Table 5.1 presents the cases studied through simulations. Similar to previous chapters, a triaxial ellipsoid and an ellipsoid of revolution were considered. We ran simulations for both these classes of ellipsoids under conditions that demonstrated a periodic and chaotic behaviour in Chapter 4. We expected that additional degree of freedom through scalar transport

Conditions	Regime		
	Passive	Hill	Valley
Distribution	$\cos(\frac{2\pi y}{L})$	$\cos(\frac{2\pi y}{L})$	$\cos(\frac{2\pi y}{L} + \pi)$
Coupling	Passive	Viscosity	Viscosity
μ_{min}	5.5	1	1
μ_{max}	5.5	10	10

Table 5.2: Initial scalar tracer distribution regimes. In the hill and valley regimes viscosity of the fluid is coupled to the tracer distribution as $\mu = \alpha$

would increase the chaotic behaviour of the ellipsoid. However, these conditions are not sufficient to completely define the initial conditions for the simulations. Thus, an initial distribution of the scalar tracer is also necessary. As can be seen from Fig. 5.3b, the simulation volume has periodic boundary conditions. The periodic boundary conditions increase the efficiency of the simulation solver. However, this constrains the functions that can be used for the tracer distribution. The function needs to be periodic and ideally have no sharp discontinuities in its derivatives across the periodic transition. Thus, we have used simple periodic functions such as $\cos(\frac{2\pi y}{L})$. Based on the nature of the tracer, we classify our simulation regimes. These are presented in Table 5.2

In the passive regime, the tracer is merely advected by the fluid and does not affect the viscosity. In many situations where mixing of particle-laden flows is essential, such as in fluidised bed reactors and droplet formation in clouds; it would nonphysical to assume that the physical quantity that is represented by the tracer would not affect the viscosity of flow. In the Hill and Valley regimes, however, the value of the advected tracer is directly coupled to the viscosity of the fluid at that point simply given by the function $\mu = \alpha$. For example, in the Hill regime, the viscosity of the fluid rises from a value of 1 at the boundary to a maximum of 10 on the centre line. For the passive case, the value of the viscosity was chosen to match the average viscosities of the Hill and Valley regime. Tables 5.1 and 5.2 completely define the parameters needed for our mixing simulations.

5.3 INFLUENCE OF MIXING AND VISCOSITY GRADIENTS

The effects of a tumbling ellipsoid on the surroundings is non-trivial. Especially for the cases in which the viscosity is coupled to the advected tracer. This coupling dramatically increases the computational requirements of the simulation. This is caused by requiring a new Laplacian equation to be solved over the domain and then iterating both the coupled Navier-Stokes and Advection-Diffusion equations until a convergence solution is found. Unfortunately, this has caused to the size of the data-set available for use to analyse in the cases of viscosity gradients to be small. The complexity of the problem can be reduced by ignoring the effects of diffusion, by set the diffusivity of the scalar to zero. This has been done for the rest of this chapter. We shall first look at the case in which the scalar is entirely passive.

5.3.1 *Advection of Passive Tracers*

The case of a passive tracer can be thought of as a dye being mixing into a fluid. The dye typically is dilute enough to assume that its effects on the physical properties of the fluid (such as viscosity) can be neglected. It was mentioned in a previous section that Tan et al. [105] showed that mixing would be chaotic, with the tracer acting as an additional degree of freedom. However, in the case of a passive tracer, this is not the case. Therefore, we see dynamics very similar to those encountered in Chapter 4. Indeed, this lends further confidence that GISS is capable of simulating both mixing and chaotic dynamics in complex systems.

5.3.1.1 *Mixing caused by Ellipsoid of Revolution*

Fig. 5.4 and 5.5 shows the plots of the distribution of the passive tracer at the end of the simulation and the trajectory of the centriod for an ellipsoid of revolution with $Re_p = 10000$ at energy ratios of $E = 1$ and $E = 20$ respectively. Here, we consider the same ellipsoid of revolution $(a : b : c = 1 : 0.7 : 0.7)$ to the using in Chapter 4. The dynamics of the ellipsoid in both cases are consistent to that seen for the non-mixing case.

We see from the trajectories of the centriod in both Fig. 5.4b and 5.4b evolve relatively smoothly. Similarly, for the tracer, as seen in Fig. 5.4a and

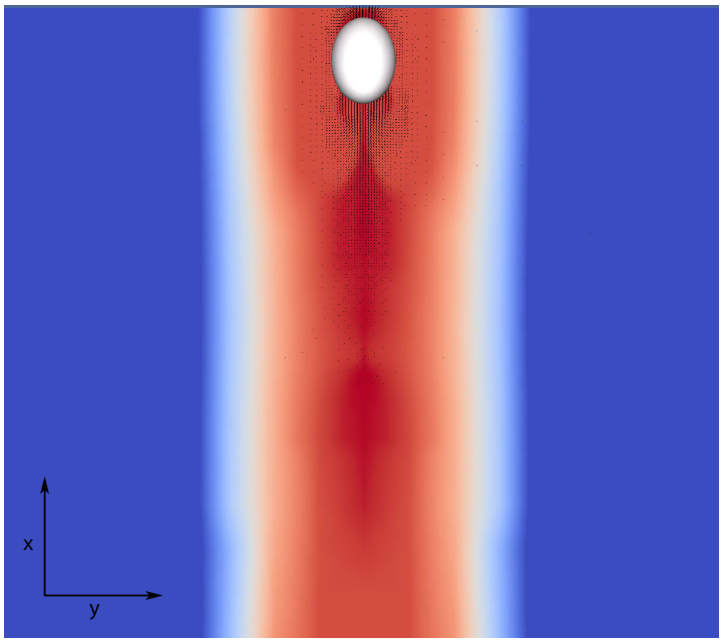

(a) Tracer Distribution at $E = 1$, xy plane at $z = 0$

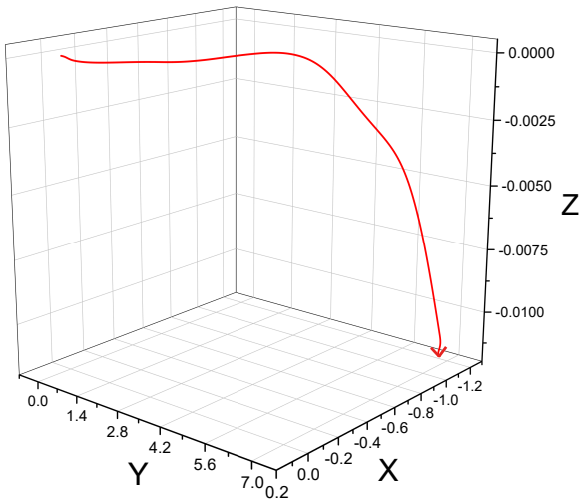

(b) Trajectory of the ellipsoid centriod at $E = 1$

Figure 5.4: Passive tracer mixed by an ellipsoid with dimensions $(a, b, c) = (1, 0.7, 0.7)$. Parameters used are $E = 1$, the density ratio $\rho = 1$ and the particle Reynolds number $Re_p = 10000$. In Fig. 5.4a, the colour represents the value of the tracer and the arrows indicate the fluid velocity vector, $\boldsymbol{u}$. In (b), the final position of the body is indicated by the arrow head

5.4a as expected, the ellipsoid drags along a region of flow in which the trace concentration is relatively constant. The resulting fluid flow caused the movement of the ellipsoid then dilutes the tracer as fluid is entrained.

While difficult to quantify analytically, when comparing cases with different energy ratios, it appears that the higher energy ratio corresponds to better mixing of the tracer. In Fig. 5.5a, we see that even though the ellipsoid has moved out of the visualisation plane, its effect on the tracer's distribution is greater than seen in Fig. 5.4a. In Fig. 5.5a, the tracer's distribution is more asymmetric along the axis of motion than the case of the lower energy ratio. A relative increase in linear motion likely causes this compared to the other case. Villermaux [110] showed that stretching component of the fluid velocity was more important to fluid mixing than the rotation component of the field. This supports our observation that as the energy ratio increases, mixing improves. When we look at the orbits of the ellipsoids, we see that dynamics is similar to Chapter 4.

We return to using RQA to analysis the behaviour of the ellipsoids orbits. For the case of the ellipsoid of revolution with passive tracer, we have seen that the system is periodic. With the caveat that only early-time dynamics can be observed due to the computation expense of the simulations. Fig. 5.6 contains the recurrence plots of both case $E = 1$ and $E = 20$. They both indicate that the system is periodic since there is a straight line across the plot and very few other features. There is an interesting feature in the upper left-hand side of Fig. 5.6b, which might indicate some non-periodic behaviour; however, it only appears very early in the simulation. This feature is likely caused by the solid needing to accelerate the fluid, as it was at rest initial and then disturbed by the sudden introduction of the momentum impulse applied to the solid. This mismatch in velocities would have caused the ellipsoid to decelerate rapidly initially, hence causing the local recurrence rate to increase. The effect was not seen in previous chapters since the time-series were much longer, and the effect of these initial velocity mismatches was diluted away. We see that for the case of the triaxial ellipsoid that dynamics are also consistent with Chapter 4.

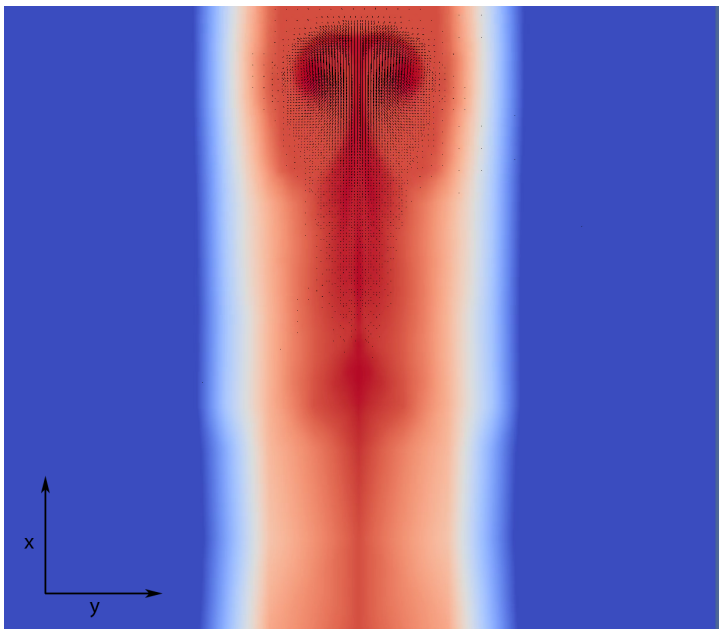

(a) Tracer Distribution at $E = 20$, xy plane at $z = 0$

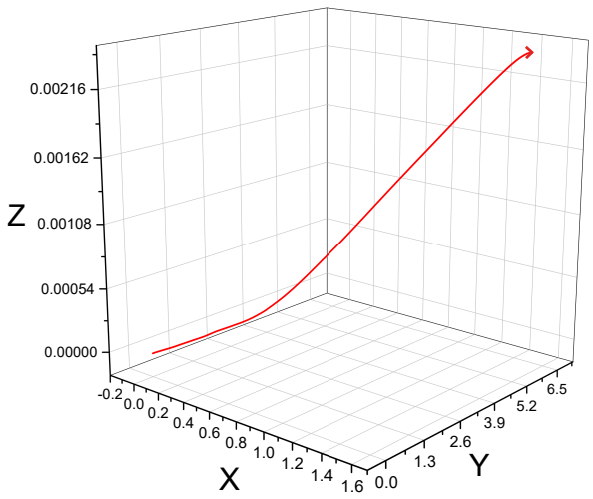

(b) Trajectory of the ellipsoid centriod at $E = 20$

Figure 5.5: Passive tracer mixed by an ellipsoid with dimensions $(a, b, c) = (1, 0.7, 0.7)$. Parameters used are $E = 20$, the density ratio $\rho = 1$ and the particle Reynolds number $Re_p = 10000$.(a), At the end of the simulation the body has moved out of the xy plane as seen in (b). However the mixing caused by wake vortex can still been in the figure.

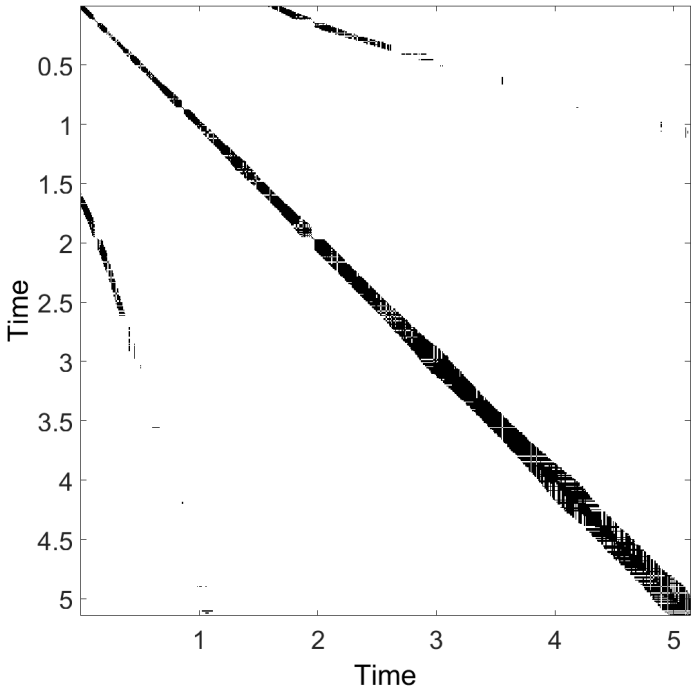

(a) $E = 1$

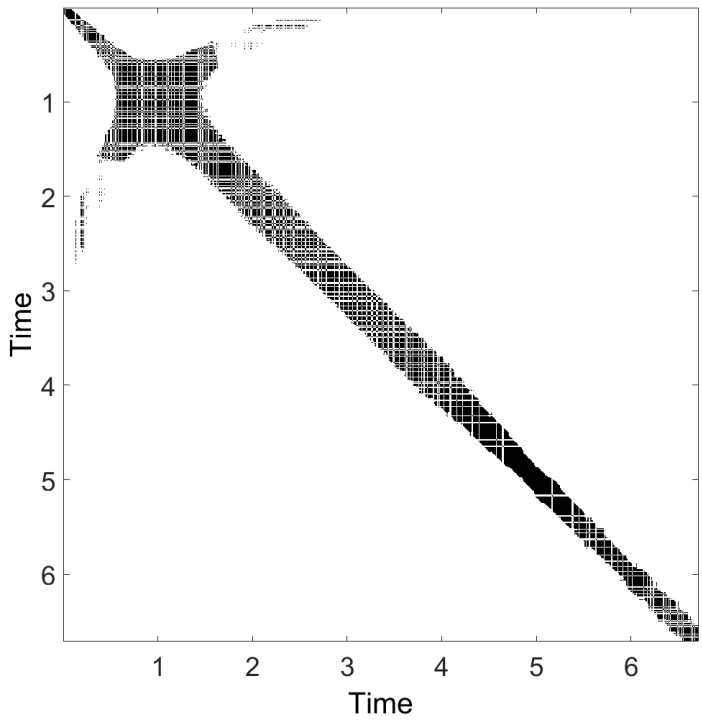

(b) $E = 20$

Figure 5.6: Recurrence plots for marker point orbit for an ellipsoid of revolution with dimensions $(a, b, c) = (1, 0.7, 0.7)$. With various energy ratios and the density ratio of $\rho = 1$ and the particle Reynolds number $Re_p = 10000$.

5.3.1.2 *Mixing caused by Triaxial Ellipsoids*

As in the previous section, we investigated how the motion of a triaxial ellipsoid's motion affected the distribution of a passive tracer. Fig. 5.7 and 5.8 shows the plots of the distribution of the passive tracer at the end of the simulation and the trajectory of the centriod for an ellipsoid of revolution with $Re_p = 10000$ at energy ratios of $E = 1$ and $E = 20$ respectively. Here, we consider a standard triaxial ellipsoid $(a : b : c = 1 : 0.8 : 0.6)$.

Fig. 5.7 and 5.8 show that for the case of the triaxial ellipsoid, its effects are very similar to the results seen previously. As before, when looking at the tracer distribution, Fig. 5.7a and 5.8a, we seen that the higher energy ratio mixes that surround fluid more effectively. Thereby causing the advection of the tracer to be more effective. This leads to the conclusion that particle-induced mixing would be more important in systems were the particles have higher linear momentum relative to angular momentum. This would apply to the case of hail-stones and droplets in clouds, since these cases, the particles tend to concentrate in zones of high stretching of the velocity field — this result of found by Ravichandran and Govindarajan [88]. The high stretching zones increase the effectiveness of mixing, [110], the added entrainment from the movement of the bodies would be expected to increase the effectiveness of the mixing in the cloud. Next, we look at the orbits that traced out by the triaxial ellipsoids.

Fig. 5.9 contains the recurrence plots of both case $E = 1$ and $E = 20$ for the marker orbits of the triaxial ellipsoids. It should be noted, that unlike in Fig. 5.6, the match with Fig. 4.15 in Chapter 4 is much better. For the case $E = 1$, as seen in Fig. 5.9a is periodic as expected and for Fig. 5.9b, we can see the start of chaotic dynamics. Chaos is characterised by the system exploring its phase-space completely as small distribution cause exponential departures as time passes, [11]. The beginning of chaotic dynamics is seen in Fig. 5.9b, with the signature of the broadening band representing that the system starting to explore its phase-space chaotically. This is further signalled by the presence of the complex blocky structure in the band. If the simulation were allowed to run for more time, we would expect to see a structure similar to that in Fig. 4.15, with the system initially being chaotic and then slowly being damped away by viscosity. In both the symmetric and the triaxial ellipsoids for a passive tracer, we have seen dynamics similar to those in Chapter 4. It should be noted that if would

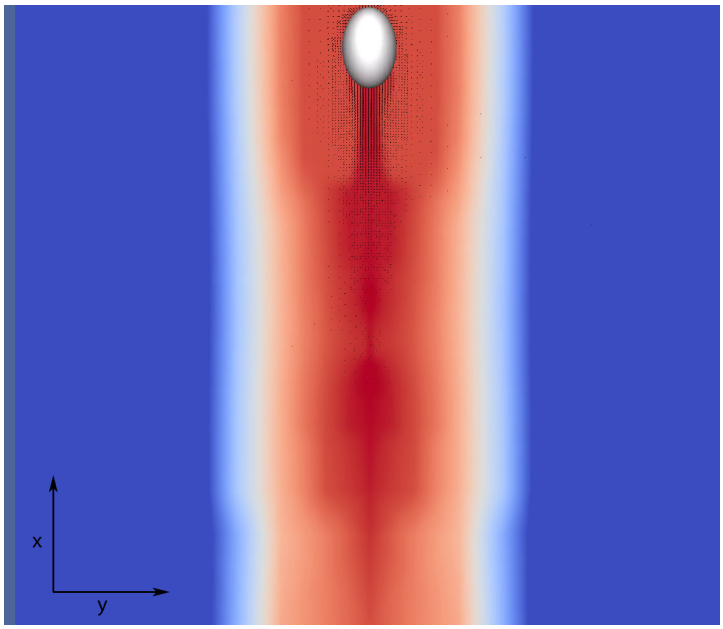

(a) Tracer Distribution at $E = 1$, xy plane at $z = 0$

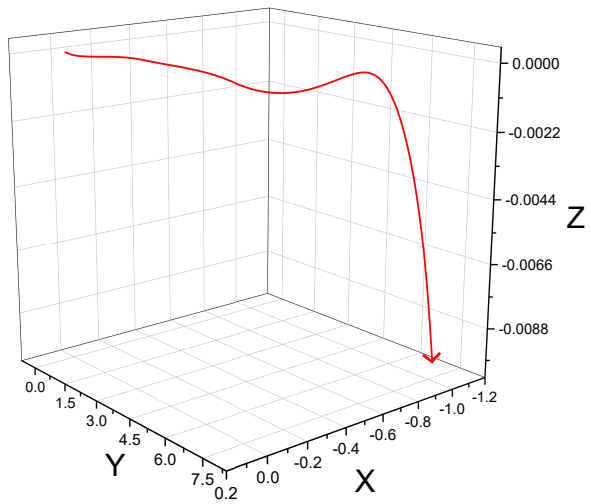

(b) Trajectory of the ellipsoid centriod at $E = 1$

Figure 5.7: Passive tracer mixed by an ellipsoid with dimensions $(a, b, c) = (1, 0.8, 0.6)$. Parameters used are $E = 1$, the density ratio $\rho = 1$ and the particle Reynolds number $Re_p = 10000$.

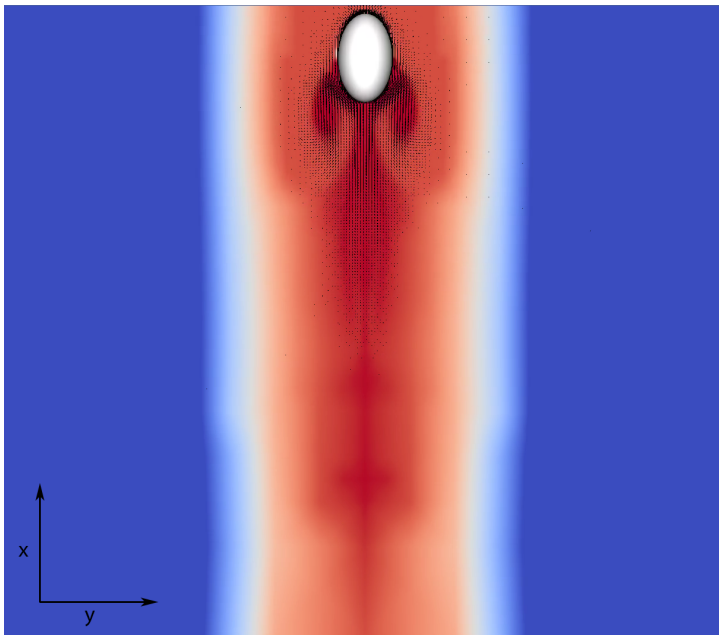

(a) Tracer Distribution at $E = 20$, xy plane at $z = 0$

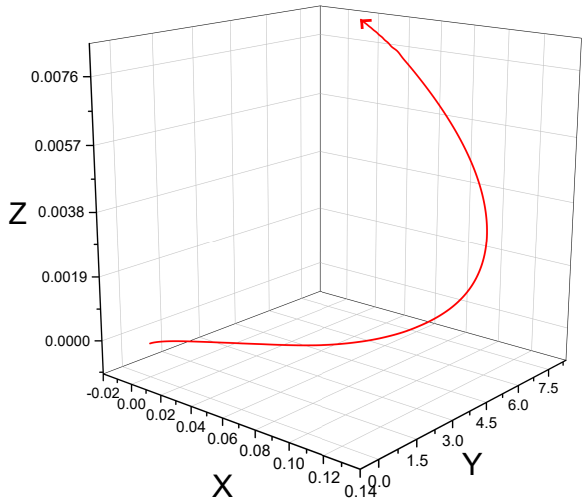

(b) Trajectory of the ellipsoid centriod at $E = 20$

Figure 5.8: Passive tracer mixed by an ellipsoid with dimensions $(a, b, c) = (1, 0.8, 0.6)$. Parameters used are $E = 20$, the density ratio $\rho = 1$ and the particle Reynolds number $Re_p = 10000$.

not be expected for the trajectories to be identical to those in Chapter 4, even for the exact same initial conditions. The addition of the scalar tracer changes how the dynamic mesh refinement occurs at any give time-step, meaning that meshes for the simulations would evolve differently.

For both the ellipsoid of revolution and the triaxial ellipsoid, it was noted that advection of the tracer appeared to be a function of the energy ratio. Further work is needed to flesh out the exact form of this dependence. However, literature is sparse when it comes to particle driven mixing of the fluid. Some work has been in this area by Boyland, Aref and Stremler [8] and along with Villermaux [110]. They both found that the stretching component to the fluid velocity field is that most important to mixing. However, for many systems assuming that the value of the tracer does not affect the fluid in any way is overly restrictive. In the following section, we present our results on viscosity coupled advected tracers.

5.3.2 *Advection of Viscosity Coupled Tracers*

The scalar tracer formalism is a mathematically convenient way to describe many physically different characteristics that can diffuse or advect through a fluid domain. These include but are not limited to parameters such as temperature and chemical concentration. These would all affect the flow in some manner and are not merely passive tracers. In this section, we couple the value of the scalar tracer directly to the viscosity by a simple rule $\mu = \alpha$, therefore the numerical value of the trace at given point in space is used a the value of the fluid at that point. This allows us to explore the additional complexity of supposing that the scalar is either temperature or concentration and then computing how that would affect the viscosity of the fluid. This allows that results to be more general, and we are not trapped by the specific physically characterises of a given material.

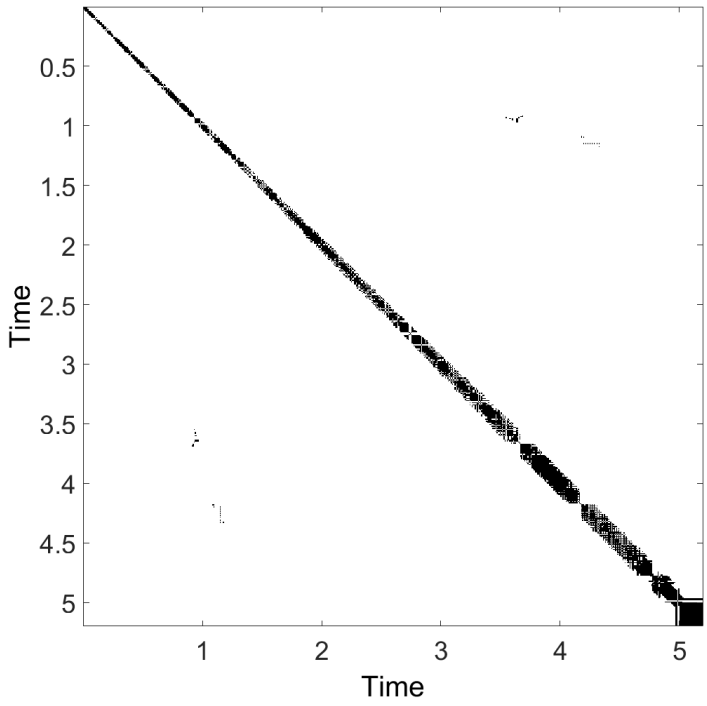

(a) $E = 1$

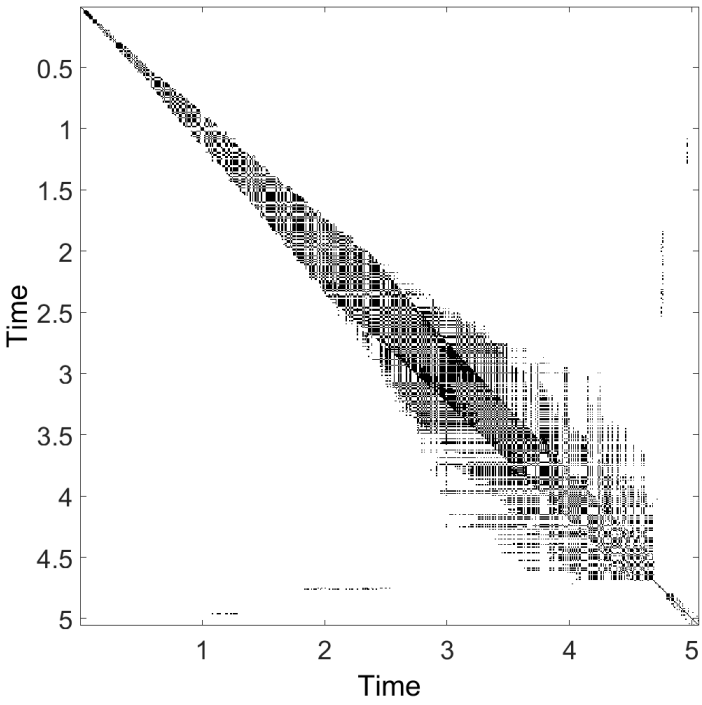

(b) $E = 20$

Figure 5.9: Recurrence plots for marker point orbit for an ellipsoid with dimensions $(a, b, c) = (1, 0.8, 0.6)$. With various energy ratios and the density ratio of $\rho = 1$ and the particle Reynolds number $Re_p = 10000$.

5.3.2.1 *Affects of Viscosity Maxima*

We considered a case similar to that used with that passive tracers, but now that viscosity is equal to the value of the tracer. Suppose that we have a viscosity field that has the following form:

$$\mu(\boldsymbol{x}) = \frac{1}{2}[(\mu_1 - \mu_0)\cos(\frac{2\pi \boldsymbol{x}_y}{L}) + \mu_1 + \mu_0]. \tag{5.11}$$

Where $\mu(\boldsymbol{x})$ is the viscosity as a function of position $\boldsymbol{x}$ and the size of the fluid domain is L. We set $\mu_0 = 1$ is the minimum viscosity and $\mu_1 = 10$ is the maximum viscosity corresponding to the initial periodic conditions of the scalar (corresponding to the hill and valley regimes mentioned in Table 5.2. This would mean that we have a maximum of viscosity along the centre-line of the fluid domain and that the initial impulse of the ellipsoid would be parallel to that line. In order to maintain the same invariants from Chapter 4 the initial condition for these simulation involving mixing were chosen so that: $\boldsymbol{L} \cdot \boldsymbol{P} = 0$. Since the initial linear momentum points along the line of maximum viscosity, the initial angular momentum must be at a right angle to it in Fig. 5.10 this would need the initial linear momentum vector is pointing to the top of the figures, and the initial angular momentum vector was chosen to lay in the plane of the figure and point to the left of the image. The evolution of these states is vastly different from that observed in the previous section.

Fig. 5.10 shows the distribution of the tracer for both the ellipsoid of revolution and the triaxial ellipsoid at the end of their respective simulations. They both started in the same symmetrical initial states. Then the triaxial ellipsoid as seen in Fig. 5.10b moved to the left of the fluid domain and ellipsoid of revolution, as seen in Fig. 5.10a stayed stationary. This is in stark contrast to what have seen in the case of a passive tracer.

Naively, it would have been expected that the ellipsoid should have behaved in the same manner as the passive case. However, with the ellipsoid in effect raiding along a hill crest of viscosity, it means that initial movement of the ellipsoid is through a regime of maximum viscous stress. Li, McKinley and Ardekani [66] found that for the spherical particles in steady channel flow, they migrate towards minima of the viscous stress. This does not explain the difference in the behaviour of the ellipsoid of

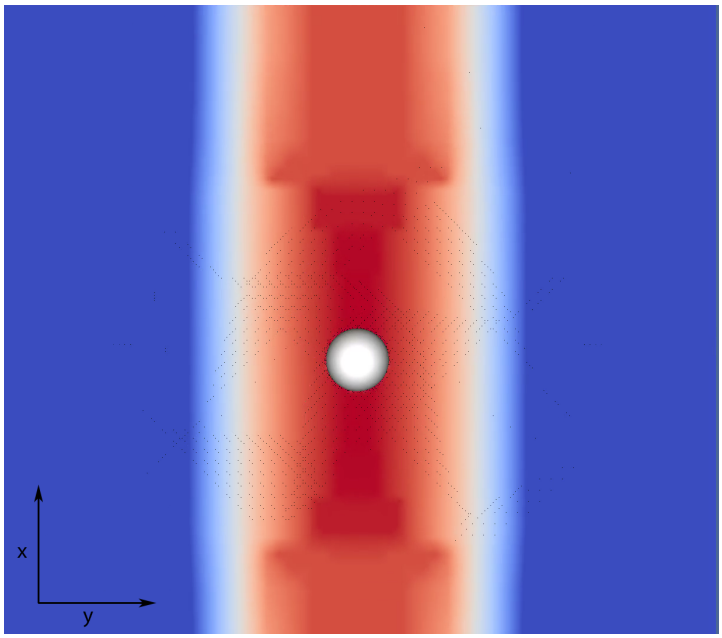

(a) Tracer distribution for ellipsoid of revolution at $E = 20$

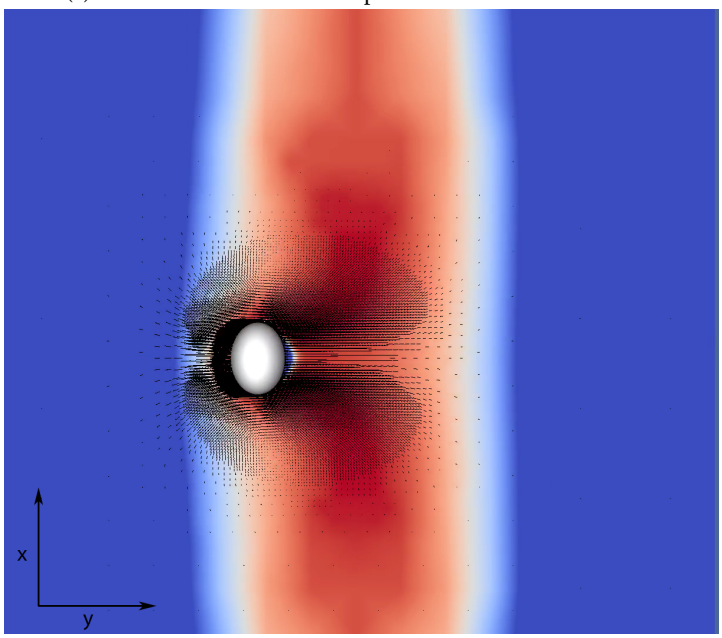

(b) Tracer distribution for triaxial ellipsoid at $E = 20$

Figure 5.10: Viscosity coupled tracer mixed by both an ellipsoid of revolution and a triaxial ellipsoid with dimensions $(a, b, c) = (1, 0.7, 0.7)$ and $(a, b, c) = (1, 0.8, 0.6)$ respectively. Parameters are $E = 20$, the density ratio $\rho = 1$ and the particle Reynolds number $Re_p = 10000$, xy plane at $z = 0$.

revolution and the triaxial ellipsoid. It should be noted that in the cases of $E = 1$ for both types of ellipsoids, the same kind of behaviour is seen (not shown).

Fig. 5.10 clearly demonstrates the differences in movement. The symmetric ellipsoid, as seen in Fig. 5.11, appears to be moving slowly along the centre-line (there is hardly any displacement in z). This slowness is the result of the being slowed by the much viscous fluid than the particle Reynolds number would suggest (since it was calculated concerning the minimum viscosity). There is no significant migration away from the centre-line. We propose that this is the result of the symmetry. If the simulation was allowed to run longer, the system might have been able to break its symmetry and move towards the stress minima. However for a triaxial ellipsoid as seen in Fig. 5.11b, the ellipsoid moves rapidly away from the centre-line and towards the lower viscosity regions along the sides. It also moves in the direction of the initial angular momentum vector was pointing. This suggests the triaxial ellipsoid experienced a net force as it rotated through the viscosity gradient. This is due to the hydrodynamic forces not being entirely cancelled, and then this effect rapidly grows as the ellipsoid moves towards the centre-line. This asymmetricity is critical in the body, moving away from the unstable equilibria that viscosity maxima represent. The effects of the viscosity gradient masked any effects that chaotic dynamics might have introduced into the mixing of the tracer. This was not the case for the viscosity minima.

5.3.2.2 *Effects of Viscosity Minima*

We also consider a case in which there was a minimum of viscosity along the centre-line of the fluid domain. This viscosity field had the following form:

$$\mu(\boldsymbol{x}) = \frac{1}{2}[(\mu_1 - \mu_0)\cos(\frac{2\pi \boldsymbol{x}_y}{L} + \pi) + \mu_1 + \mu_0]. \tag{5.12}$$

As before, $\mu_0 = 1$ is the minimum viscosity and $\mu_1 = 10$ is the maximum viscosity. The initial conditions were the same as in the previous case. Except, that in this case, the ellipsoids would be subject to a viscosity minima along the centre-line of the domain. Therefore, these ellipsoids are at a stable point, in terms of stress inducted particle migration.

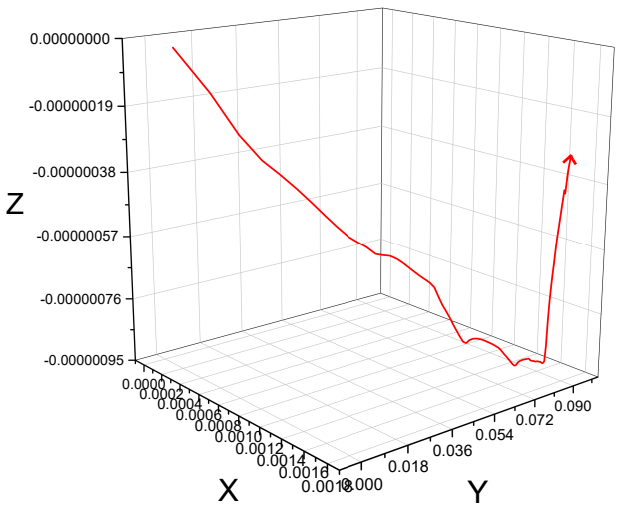

(a) Centriod trajectory for ellipsoid of revolution at $E = 20$

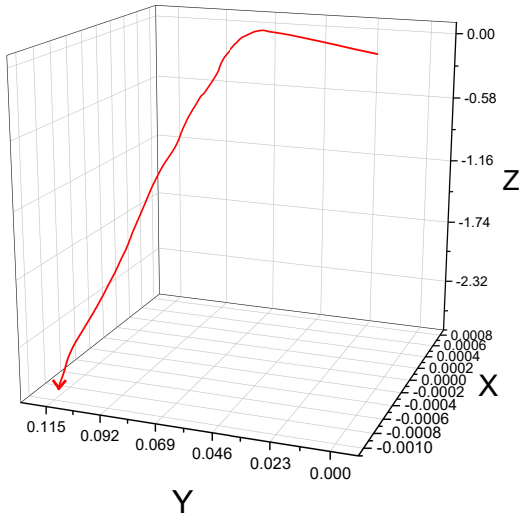

(b) Centriod trajectory for triaxial ellipsoid at $E = 20$

Figure 5.11: Trajectories of the centriod for an ellipsoid of revolution and a triaxial ellipsoid with dimensions $(a, b, c) = (1, 0.7, 0.7)$ and $(a, b, c) = (1, 0.8, 0.6)$ respectively. Parameters are $E = 20$, the density ratio $\rho = 1$ and the particle Reynolds number $Re_p = 10000$.

The coupled tracer simulations only ran for half of the simulated time when compared to passive tracer, due to increased computational demand. However, in this case the shape driven dynamics of the system is important.

The behaviour of the ellipsoid near the viscosity minima is similar to the passive case. Fig. 5.12, shows the recurrence plots for the marker orbits of the symmetric and asymmetric ellipsoids. When comparing this case to that of the passive tracer for the symmetric case, seen in Fig. 5.12a. We see that the symmetric ellipsoid in displaying periodic behaviour similar to that found in Fig. 5.6b. However there are stronger indication of chaotic dynamics, but they appear to decay away near to end of the simulation . While the asymmetric case shows the initial hallmarks of chaotic behaviour in Fig. 5.12a, given the more complex structure of the recurrence plot. Further work is required to better quantify the mixing experience in this case. Since for the timescales that we were able to simulate these systems, the mixing appears to confined to the low viscosity regions. It is not clear at this point how the higher viscosity fluid would be entrained at later times.

5.4 CONCLUSION

In this chapter, the DNS methodology described in Chapter 3 has been extended to include the Advection-Diffusion equation. This extend methodology was used to understand the dynamics of a single ellipsoid tumbling in a viscous environment with the presence of both passive and viscosity coupled tracers. In addition to the five non-dimensional parameters identified in Chapter 4, the distribution of the tracer and its coupling to the fluid viscosity dictate the dynamics of the system. For passive tracers, the dynamics are the same as seen in Chapter 4, except that effectiveness of the mixing of the tracer, is dependent of the energy ratio, E, of the system. In cases where the tracer is coupled to the flow in such a way that it creates viscosity gradients, these gradients can dominate the shape-based dynamics. The bodies move along from viscosity gradients towards minima of the viscous stress. These bodies might become trapped in unstable minima. In those cases, if the body is asymmetric, it will be able to escape sooner than a symmetric body. The dynamics of a body near stress minima

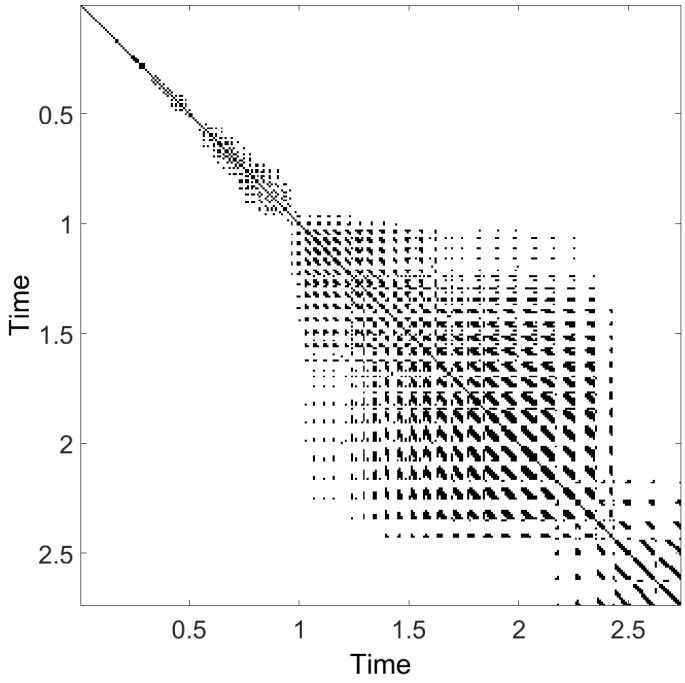

(a) Ellipsoid of Revolution at $E = 20$

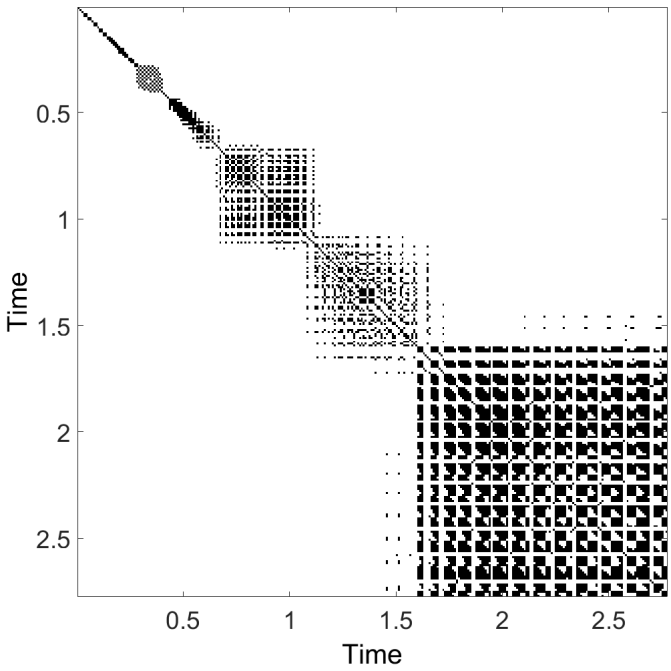

(b) Triaxial Ellipsoid at $E = 20$

Figure 5.12: Recurrence plots for marker point orbit for an ellipsoid of revolution and a triaxial ellipsoid with dimensions $(a, b, c) = (1, 0.7, 0.7)$ and $(a, b, c) = (1, 0.8, 0.6)$ respectively. Parameters are $E = 20$ and the density ratio $\rho = 1$ and the particle Reynolds number $Re_p = 10000$.

can be approximated by a body mixing a passive tracer. However, more work is needed to understand the long-term mixing of viscosity coupled tracers.

6

EFFECTS OF MULTIPLE BODIES AND CONTACT MODELS

So far, in this thesis, we have been studying the dynamics of a single immersed solid. It is possible to extend the approaches that have been used to systems of multiple bodies. Most industrial or natural systems have multiple bodies, influencing the fluid and interacting with each other. These include cyclonic solid separators, which up to only recently have only been studied using approximate methods such as Large-Eddy simulations Pisarev et al. [84]. In the field of geophysics, solid-laden flows are important for pyroclastic flows, density currents, and landslides. These flows have been extensively studied in the past by Huppert and Lister [45], Brian Dade and Huppert [9], and Neri et al. [79]. All this work has given us great insight into the behaviour of these flows, rheologically. This means that solid or immersed solid populations are treated as a second fluid phase with volume-averaged properties. While such depiction makes the resulting calculations much more feasible, but details of the behaviour of the immersed solids are lost. We will present an extension of the methodologies shown in Chapter 3 in the hope that it can be used in the future to understand these flows.

It may be recalled that GISS is composed of two sub-solvers, as described in Chapter 3. The fluid sub-solver is based on Gerris and is agnostic on the number of solid solids in the domain. This is because of the variant of the volume-of-fluid approach used to two-way couple the solid to fluid.

Fig. 6.1a shows how the presence of a single immersed solid in the fluid domain, causes the fluid mesh to be refined around it. Thereby approximating a body-fitted mesh. The fluid and solid domains are separated by a numerical interface, as shown in Fig. 6.1a. This interface is then used to calculate the volume fraction of the cell occupied by the solid and, as described in Chapter 3, allows us to implicitly enforce the two-way coupling between the dynamics of solid and the fluid. However, this exposes us to a limitation of the volume-of-fluid approach to interface tracking. Namely,

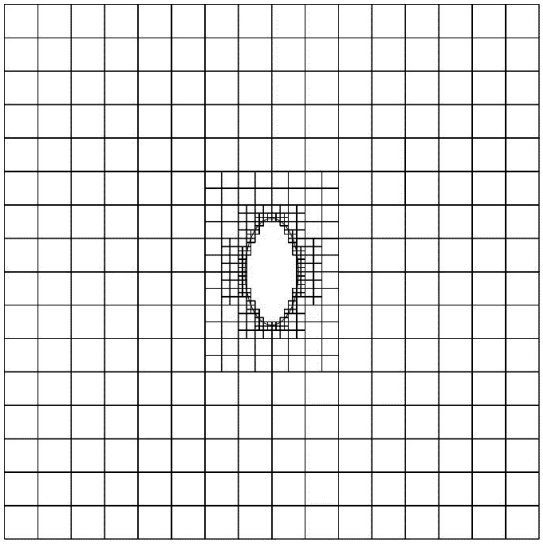

(a) Fluid Mesh Refinement

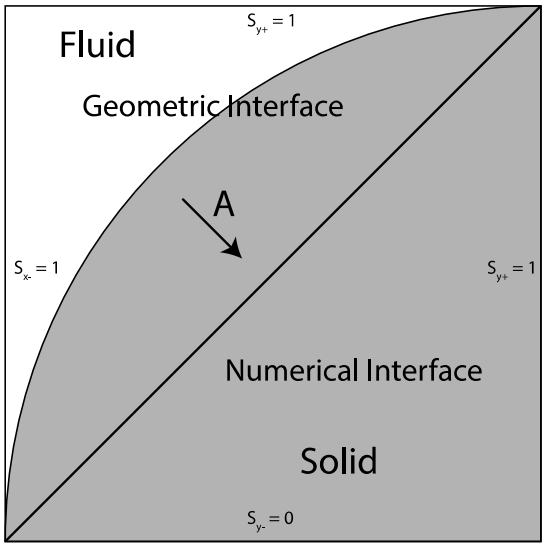

(b) Solid-Fluid Interface

Figure 6.1: Mesh refinement around an immersed body with volume-of-fluid based interface tracking

there cannot be more than one interface in a given fluid cell. Therefore, we need to ensure that when any pair of solids interact, there must be a separation of at least two-fluid mesh cells between them. A model to account for the intersolid interactions and to ensure a minimum separation between the solids is needed.

6.1 CONTACT MODELS FOR INTER-SOLID INTERACTIONS

Contact models have been studied extensively in the field of robotics, for example by Song et al. [100]. In the development of contact models, two paradigms are encountered, the penalty method and the constraint method. The penalty method models the interactions as a network of springs and dash-pots connecting the solids, and the constraint model uses a set of contact constraints to ensure no interpenetration of the solids occur. However, in solid-laden flows, inter-solid interactions such as collisions are expected to occur frequently. The contact model that is used to extend GISS is required to be both computationally inexpensive and guarantee the non-interpenetration requirements of the volume-of-fluid approach.

6.1.1 *Potential Based Contact Models*

Potential or penalty based contact models were first developed by the video games industry, as they can be very easily implemented in a preexisting six-degree-of-freedom solver, such as GISS. These models can be put on a rigorous mathematical footing, such as by Jalon et al. [48]. Contact between solids is modelled as a network of springs and dash-pots contacting them. This network then constrains the motion of the solids. The resulting motion of a solid, i that is contacted by multiple solids can be expressed as:

$$m_i \frac{d\boldsymbol{v}_i}{dt} = \boldsymbol{F}_{h,i} + m_i \boldsymbol{g}_i + \sum_j \boldsymbol{F}_{c,ij}, \tag{6.1}$$

$$\mathcal{I}_i \frac{d\boldsymbol{\Omega}_i}{dt} = \boldsymbol{T}_{h,i} + \sum_j \boldsymbol{T}_{c,ij}. \tag{6.2}$$

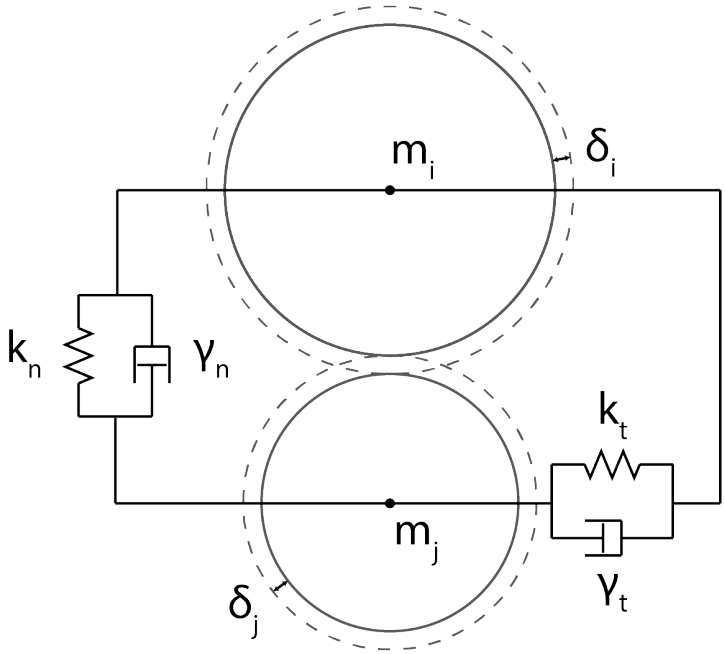

Figure 6.2: Potential model for intersolid contact, showing the tangential and normal contact forces being expressed as springs as dash-pots.

Where, m_i and $\mathcal{I}_i$ are the mass and moment of inertia of solid i, $\boldsymbol{v}_i$ and $\boldsymbol{\Omega}_i$ are the linear and angular velocities of solid i, $\boldsymbol{g}_i$ is the body force vector acting on the solid, $\boldsymbol{F}_{h,i}$ and $\boldsymbol{T}_{h,i}$ are the hydrodynamic force and torque acting on the solid, and lastly $\boldsymbol{F}_{c,ij}$ and $\boldsymbol{T}_{c,ij}$ are the force and torque exhorted on solid i by its contact with another solid j. The geometry of the contact to determine the forces and torques.

The potential contact model is shown in Fig. 6.2 is based on the Hertz-Mindlin contact model as described by Di Renzo and Di Maio [20]. The contact is decomposed into normal and tangential components. Here, k_n is the spring constant for the normal direction, γ_n is viscous damping constant for the normal direction, k_t is the spring constant for the tangential direction, γ_t is viscous damping constant for the tangential direction, and δ_i and δ_j are the thicknesses of the potential, interaction beyond this distance will produce zero force on the solid. However, the contact in GISS would not be between two perfect mathematical ellipsoids as would be implied by Fig. 6.2.

Solid objects in GISS are described using object tessellation, which decomposes the object's surface into a set of connected triangles. This method easily represents an arbitrary complex solid object in GISS. However, it comes at a price. As seen in Fig. 6.3, what would normally be

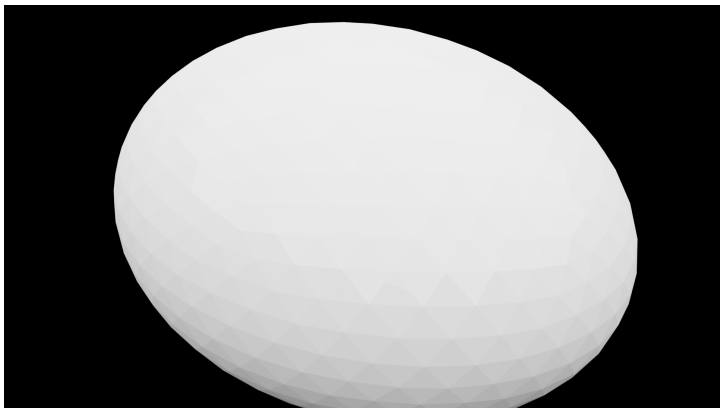

Figure 6.3: Ellipsoid as represented in GISS, the faceting of the ellipsoid is caused by solid models being described as a set of triangles comprising its surface.

expected as a smooth ellipsoid has become faceted. The fineness of the tessellation can be adjusted, and the coarseness has been exaggerated in 6.3 for visual effect. However, it means that the Hertz-Mindlin contact model needs to be adapted to this into account. This is done by considering two facets, i and j. Facet i is located on one of the contacting solids, and j is locating on the other solid. The relative velocities between the two facets can be in the following manner:

$$\boldsymbol{v}_{ij} = \boldsymbol{v}_j - \boldsymbol{v}_i + \boldsymbol{\Omega}_j \times \boldsymbol{r}_j - \boldsymbol{\Omega}_i \times \boldsymbol{r}_i, \tag{6.3}$$

$$\boldsymbol{v}_{n,ij} = (\boldsymbol{v}_{ij} \cdot \boldsymbol{n}_{ij})\boldsymbol{n}_{ij}, \tag{6.4}$$

$$\boldsymbol{v}_{t,ij} = \boldsymbol{v}_{ij} - \boldsymbol{v}_{n,ij}. \tag{6.5}$$

Where $\boldsymbol{v}_{ij}$ is the relative velocity between facets i and j, $\boldsymbol{v}_j$ and $\boldsymbol{\Omega}_j$ are the linear and angular velocity of the solid facet j is located on and $\boldsymbol{r}_j$ is the relative position of facet j on its solid. Likewise, $\boldsymbol{v}_i$ and $\boldsymbol{\Omega}_i$ are the linear and angular velocity of the solid facet i is located on and $\boldsymbol{r}_i$ is the relative position of facet i on its solid. This is based on the model presented by Navarro and Souza Braun [78]. Additional, we need to define the normal direction of the contact;

$$\boldsymbol{n}_{ij} = \frac{\boldsymbol{x}_j - \boldsymbol{x}_i}{\|\boldsymbol{x}_j - \boldsymbol{x}_i\|}, \tag{6.6}$$

$$\boldsymbol{\tau}_{ij} = \frac{\boldsymbol{v}_{t,ij}}{\|\boldsymbol{v}_{t,ij}\|}. \tag{6.7}$$

Where $\boldsymbol{n}_{ij}$ is the normal unit vector between facets i and j and while $\boldsymbol{\tau}_{ij}$ is a unit vector that is perpendicular to $\boldsymbol{n}_{ij}$ and point in the direction of the tangential motion of the two solids. The total contact force and torque applied to facet i is calculated by the sum of the interaction with all the facets on the other solid;

$$\boldsymbol{F}_c^{(i)}(t) = \sum_j (\boldsymbol{F}_{n,ij}(t) + \boldsymbol{F}_{t,ij}(t)), \tag{6.8}$$

$$\boldsymbol{T}_c^{(i)}(t) = \sum_j (\boldsymbol{r}_i \times \boldsymbol{F}_{t,ij}(t)). \tag{6.9}$$

Where is $\boldsymbol{F}_c^{(i)}(t)$ and $\boldsymbol{T}_c^{(i)}(t)$ are the contact force and torque applied to facet i as a function of time. As per the Hertz-Mindlin model the interaction is decomposed into the normal and tangential contact forces applied on facet i by facet j on a different solid given by $\boldsymbol{F}_{n,ij}$ and $\boldsymbol{F}_{t,ij}$, respectively. The normal interaction is defined in the following manner:

$$\boldsymbol{F}_{n,ij} = \begin{cases} -(k_n \sigma_n \boldsymbol{n}_{ij} + \gamma_n \boldsymbol{v}_{n,ij}) & \sigma_n \leq \delta_i + \delta_j \\ 0 & otherwise \end{cases}. \tag{6.10}$$

Here, σ_n is the distance which the potentials of the two solids overlap in the normal direction. The tangential interaction is defined similarly:

$$\boldsymbol{T}_{n,ij} = \begin{cases} -(k_t \sigma_t \boldsymbol{\tau}_{ij} + \gamma_t \boldsymbol{v}_{t,ij}) & \sigma_t \leq \delta_i + \delta_j \\ 0 & otherwise \end{cases}. \tag{6.11}$$

Here, σ_t is the distance which the potentials of the two solids overlap in the tangential direction. The overlap of the two solid potentials is defined as:

$$\sigma_n = [(\boldsymbol{x}_j - \boldsymbol{x}_i) - (\boldsymbol{r}_j + \delta_j \boldsymbol{n}_j + \boldsymbol{r}_j + \delta_i \boldsymbol{n}_i)] \cdot \boldsymbol{n}_{ij}, \tag{6.12}$$

$$\sigma_t = \int_{t_0}^{t} \boldsymbol{v}_{ij} \cdot \boldsymbol{\tau}_{ij} dt. \tag{6.13}$$

where, $\boldsymbol{n}_i$ and $\boldsymbol{n}_j$ are the normal unit vector of the facets and t_0 is the time of initial contact when the two potentials first came into contact. The total contact force and toque acting on a solid can then be calculated by the sum of the forces and torque acting on all of its facets.

This model has the advantages of being simple to implement with GISS as all the required information, such positions and velocities of the solids are already being calculated. Additionally, it is computationally efficient, since if any pair of facets are separated by a distance of $d > \delta_j + \delta_i$, the force between them is zero. This sparsity means for the vast majority of facet pairs being evaluated, no expensive calculations are required. This approach does have its shortcomings; firstly, it requires us to define five additional parameters per solid in the system viz. k_n, k_t, γ_n, γ_t, and δ_i. While empirical values for some materials are known, they are free parameters that need to tuned to ensure the system is stable. The most important disadvantage of this model is that it does not guarantee the solids will interpenetrate. If a pair of solids have enough momentum, they will interpenetrate before the potential has the opportunity to stop them. The probability of this occurring be reduced by increasing δ_i and k_n, but it would be a stop-gap measure. Therefore, in addition to the potential model, GISS uses a constraint-based contact model.

6.1.2 *Constraint Based Contact Models*

This section deals with the constraint-based approach, where the contact forces are determined such that unilateral constraints of the post-contact motion of the solids are satisfied. This method is based on the approach using in analytical mechanics, in which the forces that are applied to the

k	i_k	j_k	$\boldsymbol{n}_k$	$\boldsymbol{x}_k$
1	1	2	·	·
2	1	3	·	·
3	2	3	·	·
4	2	4	·	·
⋮	⋮	⋮	⋮	⋮

Table 6.1: The data structure used in GISS to contain the list of active contact points in the simulation, each row represents an active contact between two-solid, i and j. n_k is the normal unit vector directed from the contact point with the smaller index to the object with the larger index and the $\boldsymbol{x}_k$ is the position vector of the contact point in row k of the data structure.

systems arise from constraint placed on the system [37]. This stands in sharp contrast to the previous section, where an additional force field was added to the equations of motion to approximate contact dynamics. Baraff [5] and Mirtich [74] proposed algorithms to construct a system of simulations constraints which can be solved to find the exact contact forces and the impulses required to prevent interpenetration of solids. This approach can also be generalised to account for other types of constraints such as joints and hinges. Ruspini and Khatib [90] presented such a formulation and the work done by Sauer and Schömer [92] forms the basis of the constraint model used in GISS. In order to avoid additional complexity, friction will not be considered in this model.

As in the potential-base contact model, we suppose that there is a multiple solid system containing N solids, B_N. There are mutual contact at K contact points; an example of this can be seen in Fig. 6.4. Unlike the potential-based model, an additional data structure is required to hold the information of the K contact points. Table 6.1 is an example of the data structure used internally by GISS. For the k-th contact point stored in Table 6.1, the corresponding k-th row of the table stores the normal unit vector, $\boldsymbol{n}_k$, of contact point, the position vector, $\boldsymbol{x}_k$, of the contact, and two indices used to identify the two bodies involved in the contact, B_{i_k} and B_{j_k}. Here, f_k is the magnitude of the contact force acting in direction n_k. Lastly, $\boldsymbol{r}_{kl} = \boldsymbol{x}_k - \boldsymbol{x}_l$ is the direction vector connecting the centre of mass of solid, B_l, $(l = 1 \ldots N)$ to the k-th contact point.

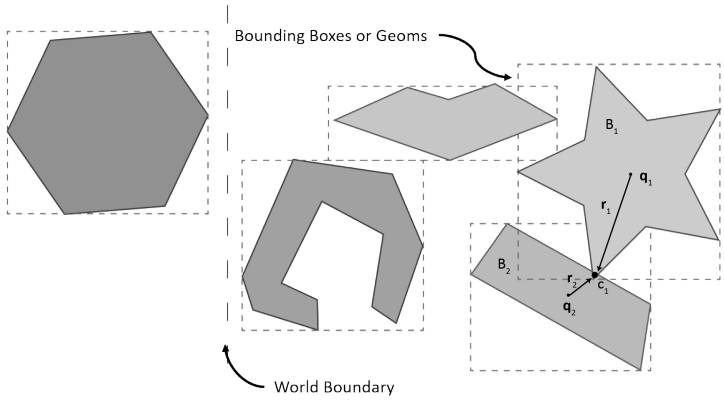

Figure 6.4: Two-dimensional schematic of constraint-based contact model. Every solid is surrounded by a bounding box or geom, and the simulation is subdivided into non-overlapping worlds into increase the algorithms efficiency

These constraints are defined globally across the system. Therefore, we need to uniquely address the configuration of all the solids, N in the system. Generalised coordinates provide us with this capability;

$$\boldsymbol{\sigma} = [\boldsymbol{x}_1, \boldsymbol{q}_1, \ldots, \boldsymbol{x}_N, \boldsymbol{q}_N] \tag{6.14}$$

$$\boldsymbol{v}_G = [\boldsymbol{v}_1, \boldsymbol{\Omega}_1, \ldots, \boldsymbol{v}_N, \boldsymbol{\Omega}_N]. \tag{6.15}$$

Here, $\boldsymbol{\sigma}$ is the generalised position and orientation vector for the system. It is the concatenation of the position vectors of the individual solids, $\boldsymbol{x}_i$ and their respective orientation quaternion, $\boldsymbol{q}$. Also, $\boldsymbol{v}_G$ is by extension the generalised velocity vector, likewise constructed from the linear, $\boldsymbol{v}_i$ and angular, $\boldsymbol{\Omega}_i$, velocities of each solid in the system. In order to more concisely describe the algorithm, it will be useful to define the following matrices and vectors; the vector of the magnitudes of the contact forces:

$$\boldsymbol{f} = [f_1, f_2, \ldots, f_K], \tag{6.16}$$

the vector of external forces, including both body forces and hydrodynamic forces:

$$\boldsymbol{f}_{ext} = [m_1\boldsymbol{g}_1 + \boldsymbol{f}_{\boldsymbol{s_1}}, -\boldsymbol{\Omega}_1 \times \mathcal{I}_1\boldsymbol{\Omega}_1, \ldots, m_N\boldsymbol{g}_N + \boldsymbol{f}_{\boldsymbol{s_N}}, -\boldsymbol{\Omega}_N \times \mathcal{I}_N\boldsymbol{\Omega}_N], \tag{6.17}$$

and the generalised orientation matrix

$$\mathcal{S} = \begin{bmatrix} \underline{\mathbf{1}} & & & & 0 \\ & \mathcal{Q}_1 & & & \\ & & \ddots & & \\ & & & \underline{\mathbf{1}} & \\ 0 & & & & \mathcal{Q}_N \end{bmatrix}. \tag{6.18}$$

Where $\underline{\mathbf{1}}$ is the identity matrix. Here, $(Q)_l$ is matrix representation of quaternion rotation,

$$\mathcal{Q}_l = \begin{bmatrix} -q_{l1} & -q_{l2} & -q_{l3} \\ q_{l0} & q_{l3} & -q_{l1} \\ -q_{l3} & q_{l0} & q_{l2} \\ q_{l2} & -q_{l1} & q_{l0} \end{bmatrix}, \tag{6.19}$$

The generalised mass matrix is given as,

$$\mathcal{M} = \begin{bmatrix} m_1\underline{\mathbf{1}} & & & & 0 \\ & \mathcal{I}_1 & & & \\ & & \ddots & & \\ & & & m_N\underline{\mathbf{1}} & \\ 0 & & & & \mathcal{I}_N \end{bmatrix}, \tag{6.20}$$

The matrix of the contact normal vectors is,

$$\mathcal{N} = \begin{bmatrix} \boldsymbol{n}_1 & & & 0 \\ & \boldsymbol{n}_2 & & \\ & & \ddots & \\ 0 & & & \boldsymbol{n}_K \end{bmatrix}. \tag{6.21}$$

We have the matrix containing the contact conditions given by,

$$\mathcal{J}_{lk} = \begin{cases} -\underline{\mathbf{1}} & \text{for } l = 2i_k - 1 \\ -\boldsymbol{r}^{\times}_{ki_k} & \text{for } l = 2i_k \\ \underline{\mathbf{1}} & \text{for } l = 2j_k - 1 \\ \boldsymbol{r}^{\times}_{kj_k} & \text{for } l = 2j_k \\ 0 & \text{otherwise} \end{cases}, \tag{6.22}$$

We also need the skew-symmetric operator,

$$\boldsymbol{r}^{\times} = \begin{bmatrix} 0 & -r_3 & r_2 \\ r_3 & 0 & -r_1 \\ -r_2 & r_1 & 0 \end{bmatrix}. \tag{6.23}$$

Taking a closer look at the structure of the contact conditions matrix, $\mathcal{J}$, we find that every column in the matrix corresponds to a contact point constraint and the rows to one solid. The columns contain two distance vectors, $\boldsymbol{r}$ for the solids in mutual contact. These matrices allow us to express the equations of motion for the system subject to its constraints in following manner:

$$\frac{d\boldsymbol{\sigma}}{dt} = \mathcal{S}\boldsymbol{v}_G \tag{6.24}$$

$$\frac{d\boldsymbol{v}_G}{ft} = \mathcal{M}^{-1}(\mathcal{J}\mathcal{N}\boldsymbol{f} + \boldsymbol{f}_{ext}). \tag{6.25}$$

When we apply the Euler discretisation scheme (used by the solid subsolver of GISS) to Eq. 6.24 and 6.25, we obtain the following equations.

$$\boldsymbol{\sigma}^{t+\Delta t} = \boldsymbol{\sigma}^{t} + \Delta t \mathcal{S} \boldsymbol{v}^{t+\Delta t} \tag{6.26}$$

$$\boldsymbol{v}^{t+\Delta t} = \boldsymbol{v}^{t} + \Delta t \mathcal{M}^{-1}(\mathcal{J}\mathcal{N}\boldsymbol{f} + \boldsymbol{f}_{ext}) \tag{6.27}$$

In order to solve for the contact forces, $\boldsymbol{f}$, we require a projection matrix so that we can extract contact configurations for two solids at their contact point from the conditions matrix, $\mathcal{J}$. The projection matrix needs to have the following form:

$$\mathcal{P}_k^T = [\underbrace{0 \dots 0}_{\text{k-1}} \quad \underline{\mathbf{1}} \quad 0 \dots 0]. \tag{6.28}$$

We can start by finding the conditions around the k-th contact point. The normal component of the relative velocities at the contact point is given by:

$$\boldsymbol{n}_k^T \mathcal{P}_k^T \mathcal{J}^T \boldsymbol{v} = \boldsymbol{n}_k^T (\boldsymbol{v}_{j_k} + \boldsymbol{\Omega}_{j_k} \times \boldsymbol{r}_{k_j}) - \boldsymbol{n}_k^T (\boldsymbol{v}_{i_k} + \boldsymbol{\Omega}_{i_k} \times \boldsymbol{r}_{k_i}). \tag{6.29}$$

If at time t the solids, B_{i_k} and B_{j_k} are already touching at the contact point located at $\boldsymbol{x}_k$, the generalised velocity will have to obey the complementarity inequality at next time step, $\boldsymbol{v}^{t+\Delta t}$. This inequality is defined as:

$$\boldsymbol{n}_k^T \mathcal{P}_k^T \mathcal{J}^T \boldsymbol{v}^{t+\Delta t} \geq 0 \quad \text{compl. to } f_k \geq 0. \tag{6.30}$$

If at time t the solids, B_{i_k} and B_{j_k} are not touching at the point located at $\boldsymbol{x}_k$, a linearised complementary condition will be used. This model the approach of the two solids ensuring no interpenetration occurs. The condition can be expressed in the following form:

$$\boldsymbol{n}_k^T \mathcal{P}_k^T \mathcal{J}^T \boldsymbol{v}^{t+\Delta t} \geq \frac{\nu_k}{\Delta t} \quad \text{compl. to } f_k \geq 0. \tag{6.31}$$

The linearisation process that is used to calculate the value of ν_k can be found in Sauer and Schömer [92], on which this model is based. The linearised complementary condition can be evaluated over all the contact points in the following form:

$$\boldsymbol{n}^T \mathcal{P}^T \mathcal{J}^T \boldsymbol{v}^{t+\Delta t} \geq \frac{\boldsymbol{\nu}}{\Delta t} \quad \text{compl. to } \boldsymbol{f} \geq 0, \tag{6.32}$$

Here, $\boldsymbol{\nu} = [\nu_1, \ldots, \nu_K]$. We can substitute Eq. 6.27 into Eq. 6.32 and obtain:

$$\mathcal{N}^T \mathcal{J}^T \mathcal{M}^{-1} \mathcal{J} \mathcal{N} \Delta t \boldsymbol{f} + \mathcal{N}^T \mathcal{J}^T (\boldsymbol{v}^t + \Delta t \mathcal{M}^{-1} \boldsymbol{f}_{ext}) - \frac{\boldsymbol{\nu}}{\Delta t} \geq 0. \tag{6.33}$$

This inequality relation can be transformed into the standard form of the linear complementarity problem (LCP):

$$\mathcal{A}\boldsymbol{z} + \boldsymbol{b} \geq 0 \tag{6.34}$$

$$\mathcal{A} \equiv \mathcal{N}^T \mathcal{J}^T \mathcal{M}^{-1} \mathcal{J} \mathcal{N} \tag{6.35}$$

$$\boldsymbol{z} \equiv \Delta t \boldsymbol{f} \tag{6.36}$$

$$\boldsymbol{b} \equiv \mathcal{N}^T \mathcal{J}^T (\boldsymbol{v}^t + \Delta t \mathcal{M}^{-1} \boldsymbol{f}_{ext}) - \frac{\boldsymbol{\nu}}{\Delta t}. \tag{6.37}$$

Here $\boldsymbol{z}$ is being solved for and is the impulse that needs to be applied to the solids in contact with each other. There are many algorithms available that can solve this classical form of LCP. GISS uses the standard Lemke-algorithm as described by Kostreva [56]. This takes the form of finding the minima the following quadratic form:

$$f(\boldsymbol{z}) = \boldsymbol{z} \cdot (\mathcal{A}\boldsymbol{z} + \boldsymbol{b}), \tag{6.38}$$

subject to the following constraints:

$$\mathcal{A}\boldsymbol{z} + \boldsymbol{b} \geq 0 \tag{6.39}$$

$$\boldsymbol{z} \geq 0. \tag{6.40}$$

Finding the minima of Eq. 6.39 provides us with the exact contact forces experienced at the time, t, in the vector $\boldsymbol{f}$. Additionally, the complementarity relations ensures that the correct impulse is applied to the solids so that no interpenetration occurs at the contact points. It stands to reason why if this approach provides us with the exact contact forces and does not require us to introduce additional free parameters, why would we use the potential based contact model?

The computational complexity of the algorithms is the answer. The potential-based model, even with its shortcomings, is more computationally efficient. A naive implementation of the contact model's computational cost would scale like, $\mathcal{O}(N^2)$ where N is the number of solids in the system. However, since only pairs of solids within a distance of $\delta_i + \delta_j$ are considered, the actual performance is even better. On the other hand, it was proven by Coxson [13] that optimisation problems such as the LCP-problems are in the NP complexity class. Therefore, no efficient algorithms are known to exist for solving these problems and the computational cost to solve the LCP constraints grows is the following manner: $\mathcal{O}(e^K)$, where K is the number of active contact points. Fig. 6.4, shows the methods used in GISS to try to work around this complexity. The simulation domain is divided into separate overlapping worlds, and the constraints are solved over each world separately, thereby reducing the complexity. This method is only valid if there if no solid spans a world divided. Therefore, the world separation planes are placed through the domain only if, they do not intersect with any of the bounding boxes of the solids in the system. While this does help with the cost, it ultimately would not solve the problem. So since we would like to use GISS in the future to simulate systems with hundreds or more solids, we need a composite contact model. An outer potential-based model which deals with the vast majority of the intersolid interactions and an inner constraint-based model that deals with the high momentum interactions. The constraint model provides the guarantee that no fluid mesh cell will contain more than one solid interface that Gerris requires. We performed validation of our composite model to ensure that the effects of the shortcomings of both approaches were minimized.

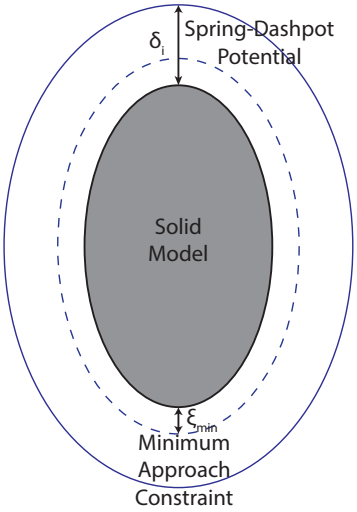

Figure 6.5: Schmatic of the composite contact model used in GISS. In outer shell the String-Dashpot potential applies and if solid crosses over into inner shell, the constraint based approach is invoked.

6.2 VALIDATION OF COMPOSITE MODEL

GISS uses a composite contact model, and this allows us to reap the advantages for both the potential and constraint paradigms while minimising the effects of either shortcoming. The model consists of two shells surrounding every solid solid in the simulation domain.

Fig. 6.5 contains a schematic overview of the models and the two shell. The outer shell's thickness, δ_i, determine the area over which the potential applies. It is a free parameter and requires tuning to minimize the number of solids that make contact with the inner shell. However, it must be larger than the minimum approach distance, ξ_{min}. This marks the beginning of the inner shell, and if a solid crosses over it, there is a risk that two mesh cells might contain two solid interfaces. This would cause numerical instability, and potentially, the solver might experience an unrecoverable error. Therefore, it is set to have the value of $\xi_{min} = 2L/2^N$, where N is the mesh refinement level, and L is the size of the domain. There should be two mesh cells contained inside the inner shell. If the potential in the outer shell does not slow the incoming solid's momentum enough and it crosses the inner shell the constraint model invoked by applying a contact constraint at the point of contact with the inner shell. This constraint stops any further penetration and minimises the number of constraints

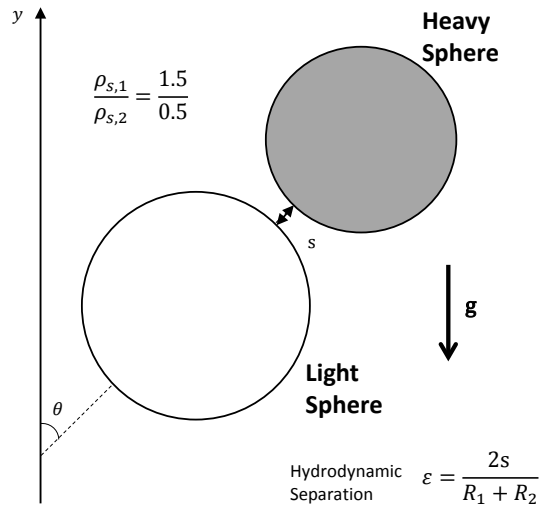

Figure 6.6: Schematic of the validation case for the contact model. The buoyant and sedimenting spheres come into contact and then move past each other.

that need to be evaluated, decreases the computational demands of the model.

We here validate the approach, in order to ensure that the composite model behaves as expected and does not increase non-physical dynamics into the simulations. There was a wide range of possible scenarios in the literature that we could have used to validate our contact model. However, we felt that it was essential to be able to compare our solver against both experimental and theoretical results. So we validate this against the problem of sedimenting spheres in viscous fluids.

Davis [16] and then later Zhao and Davis [114] investigated the motion of sedimenting spheres through viscous fluids in the Stokes regime. In this regime, Zhao and Davis [114] was able to analytically derive the equations of motion for buoyant and sedimenting spheres coming into contact with each other and moving past each other. They were later able to extend their work to include the effects of surface roughness on the contact dynamics and were able to confirm their analytical results against experiments [17]. Fig. 6.6 shows the setup for the validation case, we used to compare GISS to this body of work. Firstly, two spheres were introduced into the domain. The upper sphere will sediment but the lower sphere will rise due to buoyancy. The separation, s, between the surfaces of the two spheres along the vector connecting their centres of masses was

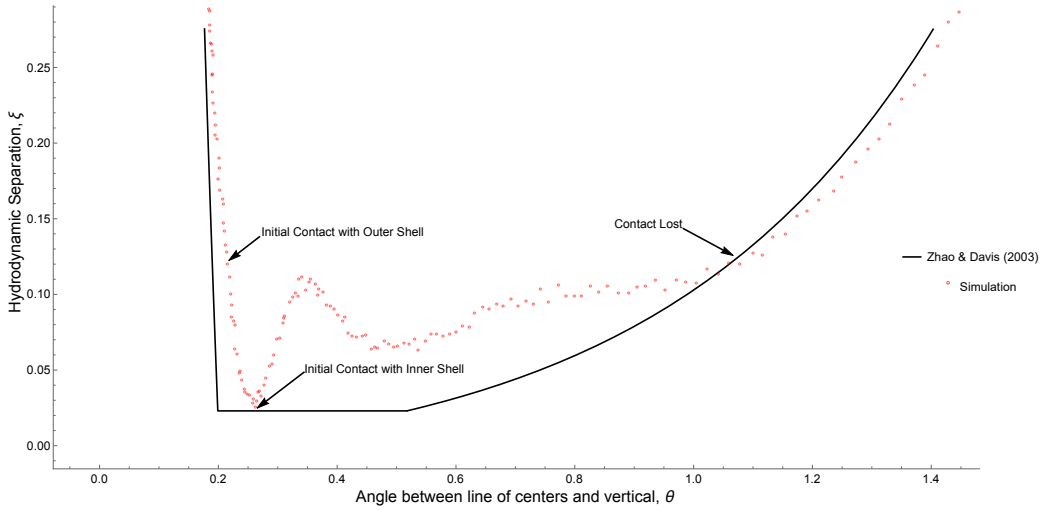

Figure 6.7: Validation results for the contact model. The motion predicted by GISS agrees well with the analytical results of Zhao and Davis [114]

recorded. The angle between the vertical axis and the vector connecting their centres of masses is also recorded.

Fig. 6.7, contains the results of our validation of GISS against the analytical equations of motions, proposed by Zhao and Davis [114]. We find that the initial approach and departure agree well with the analytical results. However, there is a deviation during the phase where the spheres are moving past one another. This error is caused by the potential causing the spheres to acts as if they were compliant. Hence the oscillatory motion as they pass each other in GISS, while in the analytical treatment they were assumed to be completely rigid. Additionally, GISS predicts that hydrodynamic separation, ξ, is always larger than theory. This caused by the requirement to ensure a maximum of one solid interface per mesh cell. This means that the radius of each sphere is effectively increased by ξ_{min}. However, these issues can be reduced by increasing the spring constant of the potential. This will reduce the oscillatory deviation by more closely approximating a hard-sphere. The over-prediction of the separation can be similarly reduced by increasing the mesh resolution and thereby reducing ξ_{min}, to a lower value.

This validation shows that the composite model allows GISS to simulate scenarios in which intersolid contact has a significant effect. However, care is needed in the tuning of the potential parameters to avoid numerical oscillations. In the future, the contact model should also be validated in

situations where there are high momentum interactions between solids, to better test hand-off between the outer and inner shells of the model.

In addition to GISS allowing used to study the effects of multiple solids on fluid flow, it is also possible to extend the Kirchhoff-Clebsch equations. This is presented in the following section.

6.3 EXTENDING THE KIRCHHOFF-CLEBSCH EQUATIONS TO MULTIPLE BODIES

In this section, we will extend the derivation of the Kirchhoff-Clebsch equations presented in Chapter. 3 to multiple solids in the ideal fluid. This is based on the premise set out by Lamb [63] and Milne-Thomson [73]. In Chapter 3, we mentioned that the Kirchhoff-Clebsch equations are valid when the fluid where the solids are immersed is infinite in extent and is an ideal fluid. Therefore, the scalar potential field, ϕ, can be defined such that the fluid velocity can be given by:

$$\boldsymbol{u} = \nabla\phi, \tag{6.41}$$

We will make use of generalised coordinates to describe the configuration of the solids in the system, much like in the previous section. If we additionally assume that the motion of the solids wholely causes movement of the fluid, this allows us to define the velocity potential in terms of these generalised coordinates:

$$\phi = \sum_{i=1}^{6N} \dot{\sigma}_i \phi_i \tag{6.42}$$

Where N is the number of solids in the system, $\boldsymbol{\sigma}$ are the generalised coordinates, and $\dot{\boldsymbol{\sigma}}$ are the generalised velocities of the system. The boundary conditions that are described in Chapter 3 need to be modified to account for the presence of multiple solids:

1. Impermeability condition for the solids, valid on the bounding surface of the fluid, S:

$$\left.\frac{\partial \phi}{\partial \boldsymbol{n}}\right|_S = \boldsymbol{n}_s \cdot \nabla \phi, \tag{6.43}$$

where $\left.\frac{\partial \phi}{\partial \boldsymbol{n}}\right|_S$ is a projection of the fluid velocity on the normal unit vector of the bounding surface of the fluid, S.

2. Stationary condition at infinity remains unchanged:

$$\lim_{\boldsymbol{x}\to\infty} \nabla \phi = 0. \tag{6.44}$$

As with the single solid Kirchhoff-Clebsch system, the potential field ϕ depends on time via the right-hand side of the boundary Eq. 6.43. Proceeding analogously to Chapter 3, it is possible to define ϕ_i from Eq. 6.41 as solutions to the Laplace equation subject to the boundary conditions, Eq. 6.43 and 6.44. Now that we have extended our method to calculate, ϕ, it is possible to calculate the kinetic energy of the fluid, K_f.

$$K_f = \frac{1}{2}\rho_F \iiint_V \|\nabla \phi\|^2 \, dV. \tag{6.45}$$

Using the Green's transformation, we can write the expression:

$$K_f = -\frac{1}{2}\rho_F \iint_S \phi \frac{\partial \phi}{\partial \boldsymbol{n}} dS, \tag{6.46}$$

Substituting Eq. 6.41 into Eq. 6.46, we obtain the following:

$$K_f = \frac{1}{2}\sum_{i=1}^{6N}\sum_{j=1}^{6N} \mathcal{A}_{ij}\dot{\sigma}_i\dot{\sigma}_j. \tag{6.47}$$

where $\mathcal{A}_{ij}$ are the generalised added masses:

$$\mathcal{A}_{ij} = -\rho \iint_S \phi_j \frac{\partial \phi_i}{\partial \boldsymbol{n}} dS = -\rho \iint_S \phi_i \frac{\partial \phi_j}{\partial \boldsymbol{n}} dS. \tag{6.48}$$

The generalised added-masses are also independent of the kinematics of the ensemble of solids. They only depend on the geometry of the individual solid. The total kinetic energy of the system, K_{tot} can be obtained by adding the kinetic energy of the solids to Eq. 6.47:

$$K_{tot} = \frac{1}{2} \sum_{i=1}^{6N} \sum_{j=1}^{6N} A_{ij} \dot{\sigma}_i \dot{\sigma}_j, \tag{6.49}$$

where $A_{i,j}$ has the value:

$$A = \mathcal{A} + \mathcal{M}. \tag{6.50}$$

Here (M) is the generalised mass tensor, that is defined in Eq. 6.20. In order to derive the equations of motion for the solids, an expression for the potential energy of the system is required. Fortunately, Lamb [63] showed that for the case where the solids are completely rigid, do not change shape and with vanishingly small potential energy, $\mathcal{V} = 0$. Therefore the Hamiltonian of the system is K_{tot} and the equations of motion can be derived by applying Hamilton's equations [37]:

$$\frac{d\dot{\boldsymbol{\sigma}}}{dt} = -\frac{K_{tot}}{d\boldsymbol{\sigma}}, \tag{6.51}$$

$$\frac{d\boldsymbol{\sigma}}{dt} = \frac{K_{tot}}{d\dot{\boldsymbol{\sigma}}}, \tag{6.52}$$

Subsistuting Eq. 6.49 into Eq. 6.51 and 6.52 we obtain a set of ODEs which are analogus to the Kirchhoff-Clebsch equations. These equations can been numerically solved to model the positions and velocities of the solids in the system. We will present preliminary results of solving these equations using a second-order Verlet algorithm [44].

6.3.1 *Validation*

The preliminary results of our investigation of the extended Kirchhoff-Clebsch equations will be presented below. There is the caveat that they are subject to change as additional work is performed. Eq. 6.51 and 6.52 will reduce down to the standard Kirchhoff-Clebsch equations for one

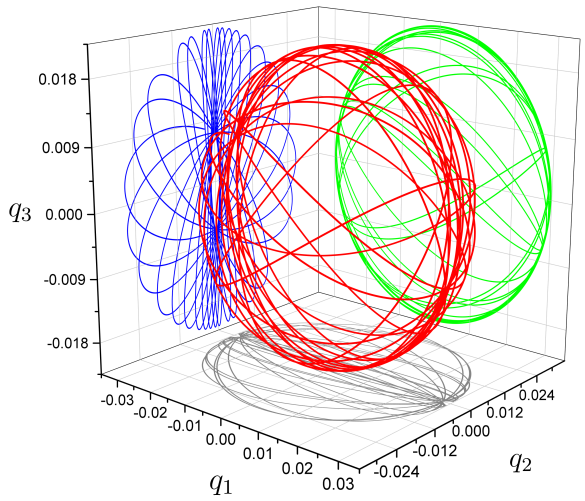

Figure 6.8: Chaotic orbits tracked by a marker point M on a triaxial ellipsoid $a : b : c = 1 : 0.8 : 0.6$ at $E = 20$ and $\rho = 1$, using Eq. 6.51 and 6.52

solid, $N = 1$. Therefore, we would expect to see identical results from Chapter 3 and the algorithm described in the previous section.

Fig. 6.8 show the orbit traced by a triaxial ellipsoid with dimensions $a : b : c = 1 : 0.8 : 0.6$ at an energy ratio of $E = 20$ and neutrally buoyant, $\rho = 1$. Its motion was modelled using the Kirchhoff-Clebsch equations from Chapter 3 and by the extended version seen in Eq. 6.51 and 6.52. The orbit predicted by both methods were very similar, the differences were caused by numerical errors. Simularity gives us confidence in the extension proposed in the previous section and its implementation in the numerical solver. Additionally, the new model was also able to capture the chaotic dynamics which is expected from an orbit with an energy ratio of $E = 20$. This gives us a foundation to build on for our investigation on the effect of multiple solids on the chaotic dynamics. However so far have only validated that the programming of the extended solver is correct with respect to the orignal code, additional validation will be required to confirm the physics of the model.

6.3.2 *Preliminary Results and Cross Recurrence Analysis*

The first case investigated with multiple solids is based on Fig. 6.8. Two identical triaxial ellipsoids were placed in the simulation domain, and their

initial linear and angular momentum vectors were parallel. A distance of $4a$ separated them. However, to analyse this system we can rely on reference plots since they are only defined for one time-series. In this case, we would have two orbits of marker points in their respective solids co-moving frame, $\boldsymbol{x}_M$ and $\boldsymbol{y}_M$. Fortunately, Marwan and Kurths [71] has proposed an extension to recurrence plots called cross recurrence plots.

Cross recurrence plots, CRP, are graphs which show all the times at which a state in one dynamical system coincides in another dynamical system. The cross recurrence plots reveal all the times when the phase-space trajectory of the first system visits roughly the same region in the phase-space as the trajectory of the second system. The cross recurrence plots is an extension of the recurrence plot definition:

$$CR_{i,j} = \begin{cases} 1 & \text{if } \| \boldsymbol{x}_M(i) - \boldsymbol{y}_M(j) \|_\infty \leq \epsilon \\ 0 & \text{otherwise,} \end{cases} \tag{6.53}$$

The cross recurrence plots can be used to quatify the correlations in the dynamics of two systems. This is analogous to the manner in which recurrence plots quatify the correlations within a single time-series.

Fig. 6.9, show the results from our first two solid simulation using the extended Kirchhoff-Clebsch equations. Fig. 6.9a is the plot of the relative orientation of the two marker points. Initially, the two points are aligned but as the systems evolves the alignment between the two solids is lost as is expected if both solids are chaotic. However, the cross recurrence plot, Fig. 6.9b reveals that the motion of the two solids remains correlated. The set of parallel lines that form regions at 90 degrees of each in the plot, indicates motion of two switches from being strongly correlated to each other. These lines are parallel to the line of identity. At other times the motion of the solids are strongly anti-correlated, when the lines are perpendicular to the line of identity. The system appears to regularly switch from regimes of correlation to anti-correlation as evidenced by the regular structure in the cross recurrence plot. Further work is required to uncover the importance of these cross-correlations in the otherwise chaotic time-series of the case two-solid system.

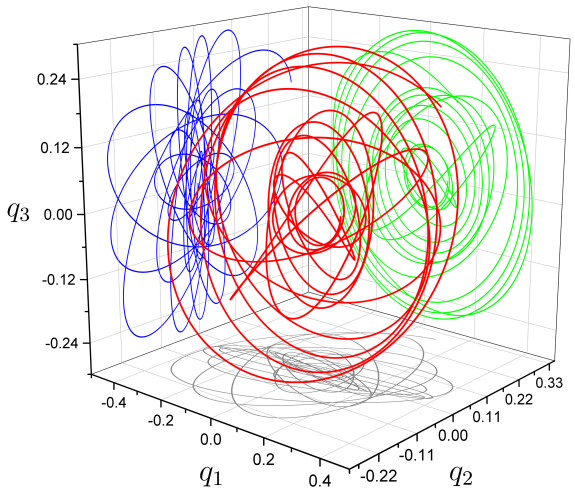

(a) Relative Orientation of Marker Points

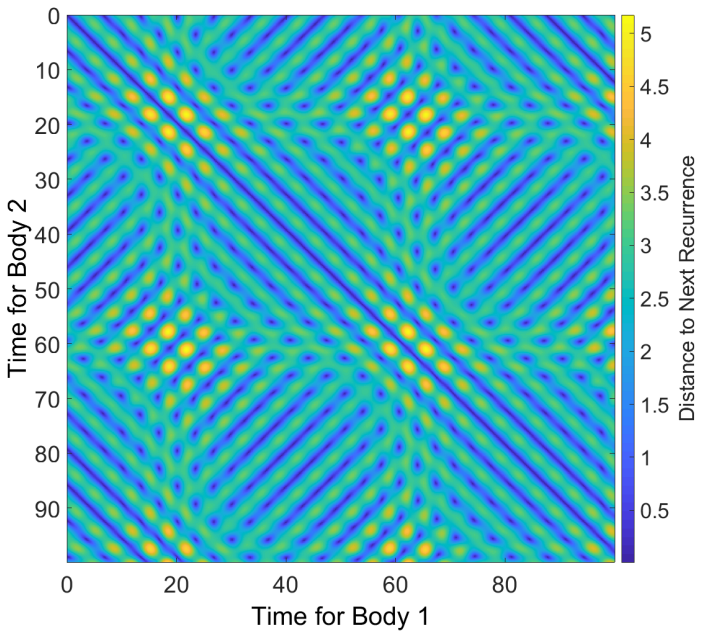

(b) Cross Recurrence Plot

Figure 6.9: Chaotic orbits tracked by the marker points M on two triaxial ellipsoid $a : b : c = 1 : 0.8 : 0.6$ at $E = 20$ and $\rho = 1$, separated by $4a$.

6.4 CONCLUSION

In this chapter, the composite contact model used in our in-house 6DoF GISS solver are presented in detail. Along with the design decisions behind the choice of a more complex composite model, it must be noted that while the GISS Solver can be used to simulate an arbitrary number of interacting solids using this contact model, the time required would be prohibitive. The validation of the contact models was also presented, and it was noted the contact model parameters need to be carefully chosen to avoid introducing additional dynamics into the problems, such as the effects of compliant bodies. This chapter further expands the theoretical framework of the Kirchhoff-Clebsch equations to account for the presence of multiple bodies. This extension was done by using Hamiltonian mechanics to extend the derivation proposed by Lamb [63]. In this chapter, we also present our preliminary result of simulating two solids systems using the extended Kirchhoff-Clebsch equations. The relative orientations of the two solids were found to regularly switch from being correlated to anti-correlated in an otherwise chaotic system. Further work is required to understand the mechanism behind this behaviour.

7

CONCLUSIONS AND FUTURE WORK

7.1 CONCLUSIONS

We have developed a solid-fluid solver, GISS, using the immersed boundary methodology and the open-source DNS fluid solver, Gerris. The solver can simulate the 6DOF motion of solid bodies in both inviscid and viscous fluids and calculate the hydrodynamic force applied on the solid accurately. In this paper, we conduct extensive validations on this solver in both the viscous and inviscid limits and show that it passes hard tests. Given that problems of bodies freely moving in fluids have been simulated far less than the flow past fixed bodies, we hope that this solver will enable future research in this direction.

We have studied conditions under which an ellipsoid displays chaotic motion in inviscid and viscous environments. We identify five nondimensional numbers which affect the dynamics: the ratios b/a and c/a of the ellipsoid axes, the fluid/solid density ratio ρ, the ratio E of initial kinetic energy in translational to rotational motion, and the particle Reynolds number. In the inviscid case, we were aided by the Kozlov-Onishchenko theorem, using which conditions for integrability can be shown to be satisfied by an ellipsoid of rotation.

We solve the Kirchhoff-Clebsch equations over a huge parameter range of ρ and E and show that the propensity of chaos depends strongly on this ratio. In particular, we show that the system supports an additional integral of motion in the form of $\boldsymbol{\Omega} \cdot \boldsymbol{L}$ in the limit of zero density ratio, by which the dynamics reduces to the classical problem of an ellipsoid in vacuum [64]. Thus it is clarified how added mass is the cause of chaos. We show how the added mass tensor for a general ellipsoid provides a vehicle for the exchange of energy between fluid and solid and between rotation and translation. The motion is also shown to be periodic in the limit of zero initial translation. We show that high fluid densities and intermediate values of the initial kinetic energy ratio increase chaos in the system. We

thus identify ranges in parameter space where the system is non-integrable, but chaos is rarely attainable.

Using GISS, we have simulated the chaotic motion of an ellipsoid in a large domain with the inviscid flow or viscous flow. Using RQA, Poincare sections and orbit maps, we have distinguished chaotic behaviour from periodic and quasi-periodic. With GISS, we can demonstrate how added mass and viscosity affect the dynamics of an ellipsoid. From the limited cases we considered, for a triaxial ellipsoid the added mass dominates the behaviour at early times, with the high Reynolds number and inviscid cases behaving similarly. At later times, viscous damping simplifies chaotic dynamics to periodic before halting it entirely. We show that asymmetric vortex shedding can cause chaotic dynamics in a spheroid, where the Kozlov-Onishchenko theorem bans chaos in inviscid flow.

We extended GISS methodology described in Chapter 3 to include the Advection-Diffusion equation. This extend methodology was used to understand the dynamics of a single ellipsoid tumbling in a viscous environment with the presence of both passive and viscosity coupled tracers. The tracer is advected, but diffusion effects are neglected. In addition to the five non-dimensional parameters identified in Chapter 4, the distribution of the tracer and its coupling to the fluid viscosity dictate the dynamics of the system. For passive tracers, the dynamics are the same as seen in Chapter 4, except that effectiveness of the mixing of the tracer, is dependent of the energy ratio, E, of the system. In cases where the tracer is coupled to the flow in such a way that it creates viscosity gradients, these gradients can dominate the shape-based dynamics. The bodies move along from viscosity gradients towards minima of the viscous stress. These bodies might become trapped in unstable minima. In those cases, if the body is asymmetric it will be able to escape sooner than symmetric bodies. The dynamics of a body near stress minima can be approximated by the behaviour seen in Chapter 4. However, more work is needed to understand the long-term mixing of viscosity coupled tracers. In addition to the effects of advection, GISS was also extended to include solid-solid interactions.

We extended GISS to account for inter-solid interactions by implementing a composite contact model. This composite model combines the benefits of the dominant paradigms in contact dynamics. Our model has the computational efficiency of a potential-based model, while also guaranteeing that no interpenetrations of the solids in the systems will occur.

The validation of the contact models was also presented, and it was noted the contact model parameters need to be carefully chosen to avoid introducing additional dynamics into the problems, such as the effects of compliant bodies. This chapter further expands the theoretical framework of the Kirchhoff-Clebsch equations to account for the presence of multiple bodies. This extension was done by using Hamiltion mechanics to extend the derivation proposed by Lamb [63]. In this chapter, we also present our preliminary result of simulating two solids systems using the extended Kirchhoff-Clebsch equations. The relative orientations of the two solids were found to regularly switch from being correlated to anti-correlated in an otherwise chaotic system. Further work is required to understand the mechanism behind this behaviour.

7.2 FUTURE WORK

We envision that this work has created several avenues for future work. In particular, we feel that the effects of viscosity gradients and mixing are of particular interest, as these gradients may have importance in the nucleation and growth of raindrops in clouds. As noted in Chapter, 5, our study focused on the effects of advection and neglected diffusion. However, the combined effects of both processes warrant exploration. The configuration space of the problem is vast, and interesting dynamics might be found as the effects of chaotic motion of the body, advection and diffusion interplay. Additional, the detailed mechanisms of the viscosity gradient driven migration is not well known and as far as we know, has mostly been concentrated on the migration of particles in steady flows. The presence of multiple bodies also bears further investigation.

In Chapter 6, we presented our extension to our solver, GISS, to handle contact interactions. We presented our preliminary finds of the effects of multiple bodies on the dynamics of the system. However, they consisted of two bodies with the same geometry, and that were well separated. Shui et al. [94], showed that for *Jeffery's orbits* long scale hydrodynamic attraction and repulsion exists between the bodies. Whether these interactions exist for the high Reynold's numbers $Re_p > 10000$ required to chaotic dynamics to appear, would be an interesting avenue of investigation to pursue. Additionally, in how the relative geometry and sizes of the two

bodies affect their shared dynamics also bears investigation. In the limit, where one body in much larger than the other we much expect its effects on the system's dynamics to dominate. However, it is possible in systems where there are many smaller particles, and their collective influence might become dominate. These studies, would be greatly augmented by the extended Kirchhoff-Clebsch formulation presented in Chapter 6, allow the inviscid limit to be investigated. However, the dynamics of these multiple body simulations require our DNS solver performance to be improved.

At present, GISS, our DNS solver is single-threaded and therefore limited in the number of particles it can simulate at once. In order to facilitate the study of larger and more complex systems in the future, finding a method to parallelize GISS is crucial. Besides investigating CUDA and other graphics, processor-based approaches would give us access to the most powerful computation device available at present. Generally, improving GISS will lay the foundation to investigate more complex phenomena in the future and will pay dividends.

REFERENCES

[1] J. R. Aarnes, N. E.L. Haugen and H. I. Andersson. 'High-order overset grid method for detecting particle impaction on a cylinder in a cross flow'. In: *International Journal of Computational Fluid Dynamics* 33.1-2 (Feb. 2019), pp. 43–58 (cit. on pp. 15, 16).

[2] M. J. Andrews and P. J. O'Rourke. 'The multiphase particle-in-cell (MP-PIC) method for dense particulate flows'. In: *International Journal of Multiphase Flow* 22.2 (Apr. 1996), pp. 379–402 (cit. on p. 12).

[3] H. Aref and S. W. Jones. 'Chaotic motion of a solid through ideal fluid'. In: *Physics of Fluids A: Fluid Dynamics* 5.12 (Oct. 1993), pp. 3026–3028 (cit. on pp. ix, 21, 22, 37, 40, 46, 47).

[4] F. Auguste, J. Magnaudet and D. Fabre. 'Falling styles of disks'. In: *Journal of Fluid Mechanics* 719 (2013), pp. 388–405 (cit. on p. 45).

[5] D. Baraff. *Analytical Methods for Dynamic Simulation of Non-penetrating Rigid Bodies*. Tech. rep. 3. 1989 (cit. on p. 112).

[6] O. Behrend. 'Solid-fluid boundaries in particle suspension simulations via the lattice Boltzmann method'. In: *Physical Review E* 52.1 (July 1995), pp. 1164–1175 (cit. on p. 13).

[7] M. Boivin, O. Simonin and K. D. Squires. 'Direct numerical simulation of turbulence modulation by particles in isotropic turbulence'. In: *Journal of Fluid Mechanics* 375 (Nov. 1998), pp. 235–263 (cit. on p. 11).

[8] P. L. Boyland, H. Aref and M. A. Stremler. 'Topological fluid mechanics of stirring'. In: *Journal of Fluid Mechanics* 403 (Jan. 2000), pp. 277–304 (cit. on p. 95).

[9] W. Brian Dade and H. E. Huppert. 'Long-runout rockfalls'. In: *Geology* 26.9 (1998), p. 803 (cit. on p. 105).

[10] D. L. Brown, R. Cortez and M. L. Minion. 'Accurate Projection Methods for the Incompressible Navier–Stokes Equations'.

In: *Journal of Computational Physics* 168.2 (Apr. 2001), pp. 464–499 (cit. on p. 25).

[11] M. Cencini, F. Cecconi and A. Vulpiani. *Chaos : from simple models to complex systems*. 1st. World Scientific, 2010, p. 460 (cit. on pp. 67, 92).

[12] R. Clift, J. R. Grace and M. E. Weber. *Bubbles, drops, and particles*. 1st. Academic Press, 1978, p. 380 (cit. on p. 32).

[13] Gregory E. Coxson. 'The P-matrix problem is co-NP-complete'. In: *Mathematical Programming* 64.1-3 (Mar. 1994), pp. 173–178 (cit. on p. 118).

[14] M. Crapper, G. Duursma, C. Robertson and S. Wong. 'EDEM-FLUENT investigation of bubble-tube interactions in gas-fluidized beds'. In: *7th International Conference on Multiphase Flow*. 2007 (cit. on p. 9).

[15] *Cumulonimbus Cloud over Africa*. Mar. 2008 (cit. on p. 2).

[16] R. H. Davis. 'Effects of surface roughness on a sphere sedimenting through a dilute suspension of neutrally buoyant spheres'. In: *Physics of Fluids A* 4.12 (1992), pp. 2607–2619 (cit. on p. 120).

[17] R. H. Davis, Y. Zhao, K. P. Galvin and H. J. Wilson. 'Solid-solid contacts due to surface roughness and their effects on suspension behaviour'. In: *Philosophical Transactions of the Royal Society A: Mathematical, Physical and Engineering Sciences* 361.1806 (May 2003), pp. 871–894 (cit. on p. 120).

[18] D. DeZeeuw and K. G. Powell. 'An Adaptively Refined Cartesian Mesh Solver for the Euler Equations'. In: *Journal of Computational Physics* 104.1 (Jan. 1993), pp. 56–68 (cit. on p. 29).

[19] R. Di Felice. 'The voidage function for fluid-particle interaction systems'. In: *International Journal of Multiphase Flow* 20.1 (1994), pp. 153–159 (cit. on p. 11).

[20] A. Di Renzo and F. P. Di Maio. 'Comparison of contact-force models for the simulation of collisions in DEM-based granular flow codes'. In: *Chemical Engineering Science* 59.3 (2004), pp. 525–541 (cit. on p. 108).

[21] E. J. Ding and C. K. Aidun. 'The dynamics and scaling law for particles suspended in shear flow with inertia'. In: *Journal of Fluid Mechanics* 423 (Nov. 2000), pp. 317–344 (cit. on p. 13).

[22] V. Dragović and B. Gajić. 'On the cases of Kirchhoff and Chaplygin of the Kirchhoff equations'. In: *Regular and Chaotic Dynamics* 17.5 (Sept. 2012), pp. 431–438 (cit. on p. 40).

[23] T. G. Drake and J. Calantoni. 'Discrete particle model for sheet flow sediment transport in the nearshore'. In: *Journal of Geophysical Research: Oceans* 106.C9 (Sept. 2001), pp. 19859–19868 (cit. on pp. ix, 3, 9).

[24] D. A. Drew and S. L. Passman. *Theory of Multicomponent Fluids*. Vol. 135. Applied Mathematical Sciences. New York, NY: Springer New York, 1999 (cit. on pp. 10, 85).

[25] Fabián Duarte, Raúl Gormaz and Srinivasan Natesan. 'Arbitrary Lagrangian–Eulerian method for Navier–Stokes equations with moving boundaries'. In: *Computer Methods in Applied Mechanics and Engineering* 193.45-47 (Nov. 2004), pp. 4819–4836 (cit. on pp. 15, 17).

[26] *Dust Plumes off Namibia*. June 2004 (cit. on p. 2).

[27] D. K. Dysthe, F. Renard, F. Porcheron and B. Rousseau. 'Fluid in mineral interfaces—molecular simulations of structure and diffusion'. In: *Geophysical Research Letters* 29.7 (Apr. 2002), p. 1109 (cit. on p. 9).

[28] J. P. Eckmann, S. Oliffson Kamphorst and D. Ruelle. 'Recurrence Plots of Dynamical Systems'. In: *Europhysics Letters* 4.91 (1987), pp. 973–977 (cit. on pp. 22, 49, 53).

[29] E. A. Fadlun, R. Verzicco, P. Orlandi and J. Mohd-Yusof. 'Combined Immersed-Boundary Finite-Difference Methods for Three-Dimensional Complex Flow Simulations'. In: *Journal of Computational Physics* 161.1 (June 2000), pp. 35–60 (cit. on p. 19).

[30] L. S. Fan and C. Zhu. *Principles of Gas–Solid Flows*. Cambridge: Cambridge University Press, 1998 (cit. on p. 10).

[31] John R. Fanchi. *Principles of Applied Reservoir Simulation*. Elsevier Inc., 2006 (cit. on p. 82).

[32] J. Feng, H. H. Hu and D. D. Joseph. 'Direct simulation of initial value problems for the motion of solid bodies in a Newtonian fluid Part 1. Sedimentation'. In: *Journal of Fluid Mechanics* 261.-1 (Feb. 1994), p. 95 (cit. on p. 15).

[33] J. Feng, H. H. Hu and D. D. Joseph. 'Direct simulation of initial value problems for the motion of solid bodies in a Newtonian fluid. Part 2. Couette and Poiseuille flows'. In: *Journal of Fluid Mechanics* 277.-1 (1994), p. 271 (cit. on p. 15).

[34] J. H. Ferziger and M. Perić. *Computational Methods for Fluid Dynamics*. Berlin, Heidelberg: Springer Berlin Heidelberg, 2002 (cit. on p. 18).

[35] D. Gidaspow. *Multiphase flow and fluidization : continuum and kinetic theory descriptions*. Academic Press, 1994, p. 467 (cit. on p. 11).

[36] R. Glowinski, T. W. Pan and J. Périaux. 'Distributed Lagrange multiplier methods for incompressible viscous flow around moving rigid bodies'. In: *Computer Methods in Applied Mechanics and Engineering* 151.1-2 (Jan. 1998), pp. 181–194 (cit. on p. 18).

[37] H. Goldstein, J. Safko and C. Poole. *Classical mechanics*. 3rd. Pearson Higher Ed, 2014, p. 664 (cit. on pp. 41, 112, 124).

[38] Marcel Gurris and Stefan Turek. 'Finite element simulation of compressible particle-laden gas flows'. In: *Journal of Computational and Applied Mathematics* 233.12 (Apr. 2010), pp. 3121–3129 (cit. on p. 14).

[39] P. Holmes, J. Jenkins and N. E. Leonard. 'Dynamics of the Kirchhoff equations I: Coincident centers of gravity and buoyancy'. In: *Physica D: Nonlinear Phenomena* 118.3-4 (July 1998), pp. 311–342 (cit. on p. 40).

[40] M. Horner, G. Metcalfe, S. Wiggins and J. M. Ottino. 'Transport enhancement mechanisms in open cavities'. In: *Journal of Fluid Mechanics* 452 (Feb. 2002), pp. 199–229 (cit. on pp. 82, 83).

[41] Louis H. Howell and John B. Bell. 'An Adaptive Mesh Projection Method for Viscous Incompressible Flow'. In: *SIAM Journal on Scientific Computing* 18.4 (July 1997), pp. 996–1013 (cit. on p. 29).

[42] P. Y. Huang, J. Feng, H. H. Hu and D. D. Joseph. 'Direct simulation of the motion of solid particles in Couette and Poiseuille flows of viscoelastic fluids'. In: *Journal of Fluid Mechanics* 343 (July 1997), pp. 73–94 (cit. on p. 15).

[43] P. Y. Huang, H. H. Hu and D. D. Joseph. 'Direct simulation of the sedimentation of elliptic particles in Oldroyd-B fluids'. In: *Journal of Fluid Mechanics* 362 (May 1998), S0022112098008672 (cit. on p. 15).

[44] W. Huang and B. Leimkuhler. 'The adaptive Verlet method'. In: *SIAM Journal of Scientific Computing* 18.1 (1997), pp. 239–256 (cit. on p. 124).

[45] H. E. Huppert and J. R. Lister. 'Particle-driven gravity currents'. In: *Journal of Fluid Mechanics* 250 (1993), pp. 339–369 (cit. on p. 105).

[46] M. A. Hyman. 'Non-iterative numerical solution of boundary-value problems'. In: *Applied Scientific Research, Section B* 2.1 (Dec. 1952), pp. 325–351 (cit. on p. 18).

[47] D. M. Ingram, D. M. Causon and C. G. Mingham. 'Developments in Cartesian cut cell methods'. In: *Mathematics and Computers in Simulation* 61.3-6 (Jan. 2003), pp. 561–572 (cit. on p. 30).

[48] J. G. Jalon, J. Cuadrado, A. Avello and J. M. Jimenez. 'Kinematic and Dynamic Simulation of Rigid and Flexible Systems with Fully Cartesian Coordinates'. In: *Computer-Aided Analysis of Rigid and Flexible Mechanical Systems*. Springer Netherlands, 1994, pp. 285–323 (cit. on p. 107).

[49] A. T. Jarullah, N. A. Awad and I. M. Mujtaba. 'Optimal design and operation of an industrial fluidized catalytic cracking reactor'. In: *Fuel* 206 (2017), pp. 657–674 (cit. on p. 4).

[50] G. B. Jeffery. 'The Motion of Ellipsoidal Particles Immersed in a Viscous Fluid'. In: *Proceedings of the Royal Society A: Mathematical, Physical and Engineering Sciences* 102.715 (Nov. 1922), pp. 161–179 (cit. on pp. 21, 32, 34, 35).

[51] A. A. Johnson and T. E. Tezduyar. '3D Simulation of fluid-particle interactions with the number of particles reaching 100'. In: *Computer Methods in Applied Mechanics and Engineering* 145.3-4 (June 1997), pp. 301–321 (cit. on p. 14).

[52] H. J. Keh and C. H. Huang. 'Slow motion of axisymmetric slip particles along their axes of revolution'. In: *International Journal of Engineering Science* 42.15-16 (Sept. 2004), pp. 1621–1644 (cit. on p. 15).

[53] A. M. Khokhlov. 'Fully Threaded Tree Algorithms for Adaptive Refinement Fluid Dynamics Simulations'. In: *Journal of Computational Physics* 143.2 (July 1998), pp. 519–543 (cit. on p. 20).

[54] G. Kirchhoff. *Vorlesungen über mathematische Physik*. Leipzig: B.G. Teubner, 1876, ix, [1], 466 p. (Cit. on p. 21).

[55] A. I. Korotkin. *Added masses of ship structures*. 1st. Vol. 88. Amsterdam: Springer Netherlands, 2009, pp. 1–391 (cit. on pp. 36, 40).

[56] Michael M. Kostreva. 'Lemke Method'. In: *Encyclopedia of Optimization*. Springer US, Aug. 2008, pp. 1868–1870 (cit. on p. 117).

[57] V. V. Kozlov and D. A. Onishchenko. 'Nonintegrability of Kirchhoff's equations'. In: *Sov. Math. Dokl* 26.2 (1982), pp. 495–498 (cit. on pp. ix, 21, 23, 40, 43, 67, 69).

[58] T. Krüger, M. Gross, D. Raabe and F. Varnik. 'Crossover from tumbling to tank-treading-like motion in dense simulated suspensions of red blood cells'. In: *Soft Matter* 9.37 (July 2013), pp. 9008–9015 (cit. on p. 13).

[59] T. Krüger, D. Holmes and P. V. Coveney. 'Deformability-based red blood cell separation in deterministic lateral displacement devices-A simulation study'. In: *Biomicrofluidics* 8.5 (Oct. 2014) (cit. on p. 1).

[60] T. Krüger, H. Kusumaatmaja, A. Kuzmin, O. Shardt, G. Silva and E. M. Viggen. *The Lattice Boltzmann Method: Principles and Practice*. 1st ed. Springer International Publishing, 2017, p. 694 (cit. on pp. 12, 13).

[61] J. B. Kuipers. *Quaternions and rotation sequences : a primer with applications to orbits, aerospace, and virtual reality*. Princeton University Press, 1999, p. 371 (cit. on p. 28).

[62] A. J. C. Ladd. 'Numerical simulations of particulate suspensions via a discretized Boltzmann equation. Part 2. Numerical results'.

In: *Journal of Fluid Mechanics* 271 (July 1994), p. 311 (cit. on p. 13).

[63] H. Lamb. *Hydrodynamics*. Dover publications, 1945, p. 738 (cit. on pp. ix, 1, 21, 36, 39, 122, 124, 128, 131).

[64] L. D. Landau and E. M. Lifshitz. *Mechanics, Second Edition*. Pergamon Press Ltd, 1969 (cit. on pp. 60, 129).

[65] L. Lee and R. J. Leveque. 'An immersed interface method for incompressible Navier-Stokes equations'. In: *SIAM Journal on Scientific Computing* 25.3 (Nov. 2003), pp. 832–856 (cit. on p. 19).

[66] G. Li, G. H. McKinley and A. M. Ardekani. 'Dynamics of particle migration in channel flow of viscoelastic fluids'. In: *Journal of Fluid Mechanics* 785 (Nov. 2015), pp. 486–505 (cit. on p. 97).

[67] E. Limacher, C. Morton and D. Wood. 'Generalized derivation of the added-mass and circulatory forces for viscous flows'. In: *Physical Review Fluids* 3.1 (Jan. 2018) (cit. on p. 37).

[68] D. F. Martin and P. Colella. 'A Cell-Centered Adaptive Projection Method for the Incompressible Euler Equations'. In: *Journal of Computational Physics* 163.2 (Sept. 2000), pp. 271–312 (cit. on p. 29).

[69] N. Marwan. 'A historical review of recurrence plots'. In: *The European Physical Journal Special Topics* 164.1 (Oct. 2008), pp. 3–12 (cit. on pp. 52, 53).

[70] N. Marwan, M. Carmen Romano, M. Thiel and J. Kurths. 'Recurrence plots for the analysis of complex systems'. In: *Physics Reports* 438.5-6 (Oct. 2007), pp. 237–329 (cit. on pp. 53, 54).

[71] N. Marwan and J. Kurths. 'Nonlinear analysis of bivariate data with cross recurrence plots'. In: *Physics Letters A* 302.5-6 (Sept. 2002), pp. 299–307 (cit. on p. 126).

[72] J. M. Masella, Q. H. Tran, D. Ferre and C. Pauchon. 'Transient simulation of two-phase flows in pipes'. In: *International Journal of Multiphase Flow* 24.5 (Aug. 1998), pp. 739–755 (cit. on p. 9).

[73] L. M. Milne-Thomson. *Theoretical hydrodynamics*. 5th. London: Macmillan, 1968 (cit. on pp. 21, 37, 40, 122).

[74] B. V. Mirtich. 'Impulse-based Dynamic Simulation of Rigid Body Systems'. PhD thesis. University of California, Berkeley, 1989, pp. 1–239 (cit. on p. 112).

[75] R. Mittal and G. Iaccarino. 'Immersed Boundary Methods'. In: *Annual Review of Fluid Mechanics* 37.1 (2005), pp. 239–261 (cit. on p. 19).

[76] N. Mordant and J. F. Pinton. 'Velocity measurement of a settling sphere'. In: *The European Physical Journal B* 18.2 (Nov. 2000), pp. 343–352 (cit. on pp. 32, 33).

[77] F. Nanayama, K. Satake, R. Furukawa, K. Shimokawa, B. F. Atwater, K. Shigeno and S. Yamaki. 'Unusually large earthquakes inferred from tsunami deposits along the Kuril trench'. In: *Nature* 424.6949 (Aug. 2003), pp. 660–663 (cit. on p. 9).

[78] H. A. Navarro and Meire P. de Souza Braun. 'Determination of the normal spring stiffness coefficient in the linear spring-dashpot contact model of discrete element method'. In: *Powder Technology* 246 (Sept. 2013), pp. 707–722 (cit. on p. 109).

[79] A. Neri, T. Esposti Ongaro, G. Macedonio and D. Gidaspow. 'Multiparticle simulation of collapsing volcanic columns and pyroclastic flow'. In: *Journal of Geophysical Research: Solid Earth* 108.B4 (Apr. 2003) (cit. on pp. 1, 105).

[80] G. S. Okin, N. Mahowald, O. A. Chadwick and P. Artaxo. 'Impact of desert dust on the biogeochemistry of phosphorus in terrestrial ecosystems'. In: *Global Biogeochemical Cycles* 18.2 (June 2004) (cit. on p. 3).

[81] N. A. Patankar. 'Numerical simulation of particulate two-phase flow'. In: (1997) (cit. on p. 15).

[82] C. S. Peskin. 'Flow patterns around heart valves: A numerical method'. In: *Journal of Computational Physics* 10.2 (Oct. 1972), pp. 252–271 (cit. on p. 18).

[83] Charles S Peskin. 'Numerical analysis of blood flow in the heart'. In: *Journal of Computational Physics* 25.3 (1977), pp. 220–252 (cit. on pp. 1, 19).

[84] G. I. Pisarev, A. C. Hoffmann, W. Peng and H. A. Dijkstra. 'Large Eddy Simulation of the vortex end in reverse-flow centrifugal sep-

arators'. In: *Applied Mathematics and Computation*. Vol. 217. 11. Feb. 2011, pp. 5016–5022 (cit. on p. 105).

[85] R. H. Pletcher, J. C. Tannehill and D. A. Anderson. *Computational fluid mechanics and heat transfer*. Boca Raton: Taylor & Francis Group, 2013, p. 763 (cit. on p. 9).

[86] S. Popinet. 'Gerris: a tree-based adaptive solver for the incompressible Euler equations in complex geometries'. In: *Journal of Computational Physics* 190.2 (Oct. 2003), pp. 572–600 (cit. on pp. 20, 25, 30, 78, 80, 82).

[87] D. Qi. 'Lattice-Boltzmann simulations of particles in non-zero-Reynolds-number flows'. In: *Journal of Fluid Mechanics* 385 (Oct. 1999), pp. 41–62 (cit. on p. 13).

[88] S. Ravichandran and R. Govindarajan. 'Vortex-dipole collapse induced by droplet inertia and phase change'. In: *Journal of Fluid Mechanics* 832 (Dec. 2017), pp. 745–776 (cit. on pp. ix, 3, 9, 12, 92).

[89] T. Rosén. 'Chaotic rotation of a spheroidal particle in simple shear flow'. In: *Chaos: An Interdisciplinary Journal of Nonlinear Science* 27.6 (June 2017), p. 63112 (cit. on p. 22).

[90] D.C. Ruspini and O. Khatib. *Collision/Contact Models for the Dynamic Simulation of Complex Environments*. Tech. rep. (cit. on p. 112).

[91] Hanan. Samet and Hanan. *Applications of spatial data structures : computer graphics, image processing, and GIS*. New York, NY: Addison-Wesley, 1990, p. 507 (cit. on p. 30).

[92] J. Sauer and E. Schömer. 'A constraint-based approach to rigid body dynamics for virtual reality applications'. In: *Proceedings of the ACM Symposium on Virtual Reality Software and Technology, VRST*. Association for Computing Machinery, 1998, pp. 153–162 (cit. on pp. 112, 117).

[93] A. N. Semenov and O. P. Polyansky. 'Numerical modeling of the mechanisms of magma mingling and mixing: A case study of the formation of complex intrusions'. In: *Russian Geology and Geophysics* 58.11 (Nov. 2017), pp. 1317–1332 (cit. on p. 82).

[94] P. Shui, P. Valluri, S. Popinet and R. Govindarajan. 'Direct Numerical Simulation Study of Hydrodynamic Interactions between Immersed Solids and Wall during Flow'. In: *Procedia IUTAM*. Vol. 15. Elsevier B.V., 2015, pp. 150–157 (cit. on pp. 20, 32–35, 131).

[95] P. Singh, T. I. Hesla and D. D. Joseph. 'Distributed Lagrange multiplier method for particulate flows with collisions'. In: *International Journal of Multiphase Flow* 29.3 (Mar. 2003), pp. 495–509 (cit. on p. 15).

[96] P. Singh, D. D. Joseph, T. I. Hesla, R. Glowinski and T. W. Pan. 'A distributed Lagrange multiplier/fictitious domain method for viscoelastic particulate flows'. In: *Journal of Non-Newtonian Fluid Mechanics* 91.2-3 (Oct. 2000), pp. 165–188 (cit. on p. 18).

[97] B. F. Smith. 'Domain Decomposition Methods for Partial Differential Equations'. In: Springer, Dordrecht, 1997, pp. 225–243 (cit. on p. 19).

[98] R. Smith. *Open dynamics engine*. 2005 (cit. on p. 28).

[99] D. M. Snider, P. J. O'Rourke and M. J. Andrews. 'Sediment flow in inclined vessels calculated using a multiphase particle-in-cell model for dense particle flows'. In: *International Journal of Multiphase Flow* 24.8 (Oct. 1998), pp. 1359–1382 (cit. on p. 12).

[100] P. Song, P. Kraus, V. Kumar and P. Dupont. 'Analysis of rigid-body dynamic models for simulation of systems with frictional contacts'. In: *Journal of Applied Mechanics, Transactions ASME* 68.1 (2001), pp. 118–128 (cit. on p. 107).

[101] J. G. Speight. 'Chapter 6 - Catalytic Cracking'. In: *The Refinery of the Future*. William Andrew Publishing, 2011, pp. 181–208 (cit. on p. 5).

[102] V. N. Starkov and N. A. Stepenko. 'Simulation of particle motion in the given speed fields'. In: *2015 International Conference on "Stability and Control Processes" in Memory of V.I. Zubov, SCP 2015 - Proceedings*. Institute of Electrical and Electronics Engineers Inc., Nov. 2015, pp. 75–77 (cit. on p. 3).

[103] *Subsea Engineering Associates*. 2019 (cit. on p. 4).

[104] M Syamlal. *MFIX documentation numerical technique*. English. Tech. rep. United States: U.S. Department of Energy, 1998 (cit. on p. 11).

[105] B.T. Tan, P. Morris, M.C. Thompson and K. Hourigan. 'Chaotic mixing simulations'. In: *Applied Mathematical Modelling* 22.12 (Dec. 1998), pp. 1047–1057 (cit. on pp. 77, 87).

[106] G. I. Taylor. 'Experiments on the Motion of Solid Bodies in Rotating Fluids'. In: *Proceedings of the Royal Society A: Mathematical, Physical and Engineering Sciences* 104.725 (Oct. 1923), pp. 213–218 (cit. on p. 21).

[107] T. E. Tezduyar. 'Finite element methods for flow problems with moving boundaries and interfaces'. In: *Archives of Computational Methods in Engineering* 8.2 (2001), pp. 83–130 (cit. on p. 18).

[108] T. E. Tezduyar, J. Liou and D. K. Ganjoo. 'Incompressible flow computations based on the vorticity-stream function and velocity-pressure formulations'. In: *Computers & Structures* 35.4 (Oct. 1990), pp. 445–472 (cit. on p. 15).

[109] H. S. Udaykumar, W. Shyy and M. M. Rao. 'ELAFINT: a mixed eulerian-lagrangian method for fluid flows with complex and moving boundaries'. In: *International Journal for Numerical Methods in Fluids* 22.8 (1996), pp. 691–712 (cit. on p. 29).

[110] E. Villermaux. 'Mixing Versus Stirring'. In: *Annual Review of Fluid Mechanics* 51.1 (Jan. 2019), pp. 245–273 (cit. on pp. 89, 92, 95).

[111] Y. Yali Tang, E. A.J.F. Frank Peters, J. A. M. Hans Kuipers, S. H. L. Sebastian Kriebitzsch and M. A. Martin van der Hoef. 'A new drag correlation from fully resolved simulations of flow past monodisperse static arrays of spheres'. In: *AIChE Journal* 61.2 (Feb. 2015), pp. 688–698 (cit. on p. 11).

[112] A. L. Yarin, O. Gottlieb and I. V. Roisman. 'Chaotic rotation of triaxial ellipsoids in simple shear flow'. In: *Journal of Fluid Mechanics* 340 (June 1997), pp. 83–100 (cit. on p. 21).

[113] D. Z. Zhang and A. Prosperetti. 'Averaged equations for inviscid disperse two-phase flow'. In: *Journal of Fluid Mechanics* 267.-1 (Oct. 1994), p. 185 (cit. on p. 10).

[114] Y. Zhao and R. H. Davis. 'Interaction of two touching spheres in a viscous fluid'. In: *Chemical Engineering Science* 57.11 (June 2002), pp. 1997–2006 (cit. on pp. 120, 121).

COLOPHON

This document was typeset using the typographical look-and-feel `classicthesis` developed by André Miede and Ivo Pletikosić. The style was inspired by Robert Bringhurst's seminal book on typography "*The Elements of Typographic Style*". `classicthesis` is available for both LaTeX and LyX:

https://bitbucket.org/amiede/classicthesis/

Happy users of `classicthesis` usually send a real postcard to the author, a collection of postcards received so far is featured here:

http://postcards.miede.de/

Thank you very much for your feedback and contribution.

Final Version as of 12th May 2020 (0.0.1).